Unraveling Femtosecond Spin and Charge Dynamics with EUV T-MOKE Spectroscopy

Dissertation

for the award of the degree
DOCTOR RERUM NATURALIUM
of the Georg-August-Universität Göttingen

within the doctoral program *Physics*
of the *Georg-August University School of Science (GAUSS)*

submitted by

Henrike Probst
from Braunschweig

Göttingen, 2023

Thesis Committee

Prof. Dr. Stefan Mathias
I. Physikalisches Institut, Georg-August-Universität Göttingen

Prof. Dr. Vasily Moshnyaga
I. Physikalisches Institut, Georg-August-Universität Göttingen

Prof. Dr. Peter Blöchl
Institut für Theoretische Physik, Technische Universität Clausthal

Members of the Examination Board

Reviewer:
Prof. Dr. Stefan Mathias
I. Physikalisches Institut, Georg-August-Universität Göttingen

Second Reviewer:
Prof. Dr. Martin Wenderoth
IV. Physikalisches Institut, Georg-August-Universität Göttingen

Further members of the Examination Board

Prof. Dr. Vasily Moshnyaga
I. Physikalisches Institut, Georg-August-Universität Göttingen

Prof. Cynthia A. Volkert, PhD
Institut für Materialphysik, Georg-August-Universität Göttingen

Prof. Dr. Peter Blöchl
Institut für Theoretische Physik, Technische Universität Clausthal

Dr. Tobias Meyer
Institut für Materialphysik, Georg-August-Universität Göttingen

Date of the oral examination: 21$^{\text{st}}$ August 2023

«Chaque fois que la science avance d'un pas, c'est qu'un imbécile la pousse, sans le faire exprès.»
- Émile Zola, French novelist and journalist (1840 - 1902)

To my family!

Publications

During my doctoral research, I contributed to three articles, which are all relevant to this thesis. The first has been published in a peer-reviewed journal. The last two were recently submitted and are available online as preprints.

Ultrafast element-resolved magneto-optics using a fiber-laser-driven extreme ultraviolet light source

   Christina Möller, **Henrike Probst**, Johannes Otto, Karen Stroh, Carsten Mahn, Sabine Steil, Vasily Moshnyaga, GS Jansen, Daniel Steil, and Stefan Mathias. *Review of Scientific Instruments* 92.6 (2021). DOI: `https://doi.org/10.1063/5.0050883`

Unraveling Femtosecond Spin and Charge Dynamics with EUV T-MOKE Spectroscopy

   Henrike Probst, Christina Möller, Maren Schumacher, Thomas Brede, John Kay Dewhurst, Marcel Reutzel, Daniel Steil, Sangeeta Sharma, GS Jansen, and Stefan Mathias. *arXiv preprint arXiv:2306.02783 [cond-mat.mtrl-sci]* (2023)

Verification of ultrafast spin transfer effects in FeNi alloy

   Christina Möller, **Henrike Probst**, GS Jansen, Maren Schumacher, Mariana Brede, John Kay Dewhurst, Marcel Reutzel, Daniel Steil, Sangeeta Sharma, and Stefan Mathias. *arXiv preprint arXiv:2306.02793 [cond-mat.mtrl-sci]* (2023)

List of Abbreviations

3d FM	3d ferromagnets
3TM	Three temperature model
ARPES	Angle-resolved photoemission spectroscopy
DOS	Density of states
DFT	Density functional theory
EUV	Extreme ultraviolet
FM	Ferromagnet
GIP	Grazing incidence plate
HXAS	Helicity-dependent soft X-ray absorption spectroscopy
HHG	high-harmonic generation
M3TM	Microscopic three temperature model
MAT	Magnetization-asymmetry test ratio
MCD	Magnetic circular dichroism
MOKE	Magneto-optical Kerr effect
NIR	Near-infrared
OISTR	Optically induced intersite spin transfer
T-MOKE	Transverse magneto-optical Kerr effect
TDDFT	Time-dependent density functional theory
TM	Transition metal
XMCD	X-ray magnetic circular dichroism
XRD	X-ray diffraction

Contents

Introduction

"I happen to have discovered a direct relation between magnetism and light, also electricity and light, and the field it opens is so large and I think rich, that I naturally wish to look at it first."

- MICHAEL FARADAY in a letter to CHRISTIAN FRIEDRICH SCHÖNBEIN (Nov. 1845)

With these words, MICHAEL FARADAY described his observation that linearly polarized light undergoes a rotation of the polarization when propagating through a magnetized medium [1]. At the time of his discovery, FARADAY was already aware of the potential of this phenomenon, and history shows that he was proven right. Together with the demonstration of the same effect in reflection about 30 years later [2], FARADAY and KERR laid the foundations for the vast research field of magneto-optics as we know it today.

In the 19th century, magneto-optical effects were a driving force for the development of electrodynamics, as they helped to establish MAXWELL's theory of electromagnetism [3]. At the turn of the 20th century, magneto-optical phenomena played a crucial role in unveiling the fundamentals of quantum mechanics and contributed, for example, to the development of the theory of dispersion by LORENTZ and DRUDE [4, 5]. However, a wide-spread use of magneto-optical techniques remained relatively limited until the 1960s due to the lack of suitable light sources [6]. With the emergence of laser technology, a veritable boom in experimental research on magneto-optics was finally unleashed in the second half of the last century and this initiated first applications in data-storage technology [7–10].

Three decades ago, the combination of magneto-optics with femtosecond laser pulses added another dimension to magneto-optical experiments, as this advancement enabled to explore the manipulation of the magnetic state in the femtosecond-time domain using

pump-probe techniques [11]. With the ability to affect spins with previously unimagined speed, the research field of ultrafast magnetism was born. This led to the revelation of numerous ultrafast magnetic phenomena reaching from ultrafast magnetization quenching on a few tens of femtoseconds [12] to all-optical magnetization switching [13, 14] and laser-induced magnetization generation [15] to coherent spin precession at THz frequencies [16]. Interest in the field of ultrafast demagnetization is continuously growing, as a profound understanding of the underlying microscopic processes could provide new tools for technologies, such as spintronics, magnetic recording, and magnonics.
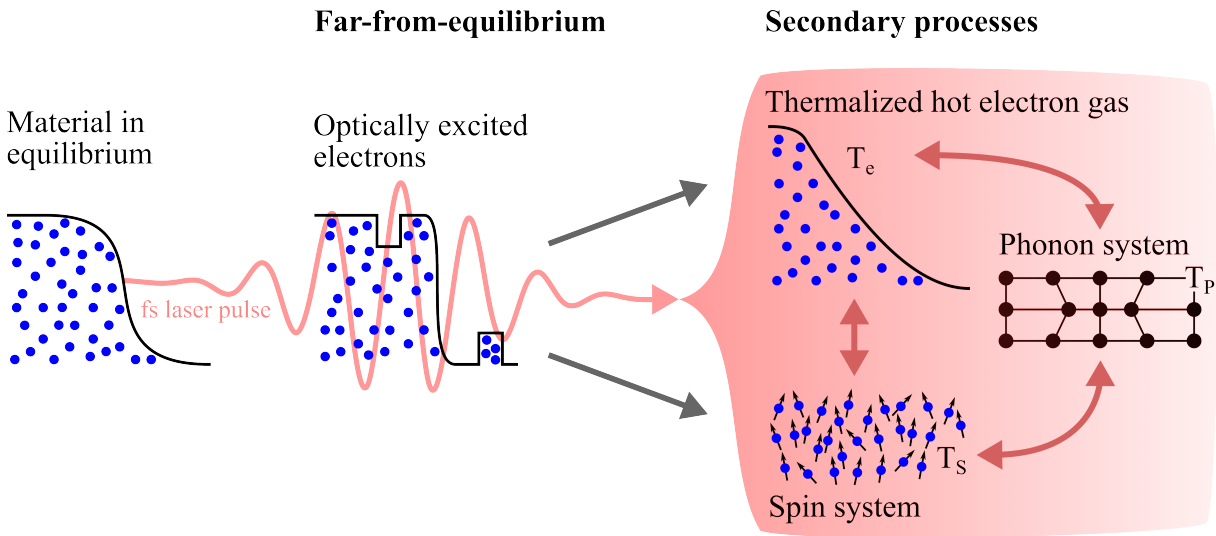

Figure 1.1. – Interaction of a femtosecond laser pulse with a ferromagnetic material in equilibrium. During the optical excitation (red pulse), the electron system (including spins) is excited into a far-from-equilibrium distribution, which cannot be described by a Fermi-Dirac distribution anymore (middle panel). Thereupon, the electron system decays into a hot electron distribution and a cascade of secondary processes (spin transport, spin-flip scattering) lead to the macroscopic demagnetization of the system (right panels).

To date, most work on optically excited magnetic materials has focused on secondary processes including spin transport and spin-flip scattering, which ultimately lead to the demagnetization of the material [17, 18]. However, the fastest way to manipulate the magnetic state lies in the direct manipulation of the spin system with the light field itself, which provides the potential for a direct, coherent control of the spin redistribution [19]. The underlying microscopic mechanisms of such phenomena, which are only limited by the duration of the laser pulse itself, are highly challenging to elucidate by experimental and theoretical means. Upon optical excitation, a far-from-equilibrium state occurs, where the electron and spin systems are significantly perturbed (see Figure 1.1). The need to understand this highly complex state of matter has grown, especially following

the experimental observations of the optically induced intersite spin transfer (OISTR) process [12, 20–26], which represents one of the fastest mechanisms to manipulate magnetization with light.

In this context, magneto-optical techniques that allow for a spectral analysis of the excited material have proved to be particularly promising, as they allow for a more complete view on charge and spin dynamics as a function of probing energy. This can be achieved by using high photon energies in the extreme ultraviolet (EUV) and soft X-ray spectral regions, which allow operating at the M- and L-edges of the $3d$ ferromagnets ($3d$ FM) [27].

While the functionalities of magnetic materials are often realized in multi-component systems, the interplay of different elements adds further challenges to the already complex interplay of spin, charge, and phonon dynamics after femtosecond laser excitation. As a result, for the study of the far-from-equilibrium state, the $3d$ FM Ni, Co, and Fe have recently received significantly more attention [28–30]. In particular, considerable effort has been devoted to the study of femtosecond charge and spin dynamics. However, a truly quantitative picture of the complex interplay of these subsystems upon laser excitation has remained elusive so far.

At this point, we aim to follow up on previous studies by investigating the spectrally-resolved magneto-optical properties of the $3d$ FM by means of the transverse magneto-optical Kerr effect (T-MOKE) in the EUV spectral range. The overall goal is to gain a deeper understanding of the underlying microscopic processes in the far-from-equilibrium state during and shortly after the optical excitation, and to clarify the respective roles of charges and spins. In doing so, we address the question of optical contributions to the magneto-optical signal, which has been the subject of a long-lasting debate in the magneto-optical community [31–39]. In addition, in response to recently reported non-linearities between the T-MOKE measurement signal and the magnetization by Jana et al. [28], we attempt to clarify the connection between the T-MOKE observable and other magnetic properties.

The thesis is structured as follows: In Chapter 2 I give a brief introduction to the theoretical background, starting with the basic concepts of ferromagnetism and an overview on ultrafast magnetism. Further, I provide a review of recently reported spectrally-resolved magneto-optics of the $3d$ FM in the far-from-equilibrium state, from which I develop a

series of research questions for this thesis. This is followed by an introduction to the fundamental physics of the interaction of light with magnetic matter in Chapter 3, where I focus on the T-MOKE and provide a profound overview on the spectral response of the 3d FM in the EUV spectral range. In Chapter 4 I give a detailed description of the EUV T-MOKE setup that was constructed and built up in a joint effort with my coworkers Christina Möller and Johannes Otto. The chapter concludes with a benchmarking of the spectral analysis by presenting time- and energy-resolved T-MOKE and s-polarized reflectivity measurements of a Ni thin film. In Chapter 5 I present an intriguing effect in the EUV T-MOKE experiment, where under almost identical experimental conditions seemingly contradictory dynamics of the transient magnetic asymmetry of Ni are found. I provide a direct solution to this initially disturbing observation by introducing a new sophisticated analysis of the T-MOKE measurement data. This analysis allows to unambiguously identify magnetic and non-magnetic contributions to our magneto-optical signal and provides a direct comparison to time-dependent density functions theory (TDDFT) calculations through the same quantity, i.e., the transient dielectric tensor. This method, which was developed in a joint effort with Christina Möller, allows us to trace the optically-induced spin and charge dynamics in exceptional detail. Chapter 6 discusses the far-from-equilibrium spin dynamics of all 3d FM Ni, Co, and Fe with a focus on differences and similarities in the observed dynamics. I then extend the discussion to longer timescales and consider different types of magnetic excitations to the ultrafast demagnetization in these systems. The thesis concludes by summarizing our achievements and answering the research questions developed in Chapter 2. Finally, I provide an outlook on future research prospects based on the results presented in the framework of this thesis.

Ferromagnetism and ultrafast demagnetization

This chapter serves as an introduction to the fundamental topics treated in this thesis, starting with the basic concepts of ferromagnetism and a brief discussion of theoretical models to understand the ferromagnetic behavior of the materials of interest: the $3d$ ferromagnets ($3d$ FM) Nickel, Cobalt, and Iron. Thereafter, follows a short introduction to ultrafast magnetization dynamics, providing an overview on some theoretical microscopic models that have been established to describe magnetization dynamics at ultrafast timescales. The chapter concludes with a review of the recently reported spectrally-resolved spin dynamics of $3d$ FM. In the last part, the focus will be on the ultra-short timescale, where the role of charge and spin dynamics will be discussed in particular.

2.1. Ferromagnetism

This thesis focuses on the ultrafast spin dynamics of ferromagnetic $3d$ transition metals (TM) Nickel, Cobalt, and Iron. Therefore, it is essential to understand the origin of the ferromagnetism in these elements, which will be shortly discussed in the following. For a more detailed overview on collective magnetism in general, the interested reader is referred to the textbooks of STÖHR and COEY [40, 41].

The characteristic feature of a ferromagnet (FM) is the spontaneous alignment of the magnetic moment in the absence of an external magnetic field, resulting in parallel long-range order of magnetic moments (spins) on each atomic lattice site. This spontaneous magnetization is present below a critical temperature, the CURIE temperature T_C, where the transition from a spontaneously magnetized material to a material with randomized spin orientation occurs. The origin of long-range magnetic order in solids can be found in

the "exchange interaction" between neighboring atoms, which was introduced by HEISEN-
BERG in 1928 [42].

2.1.1. Heisenberg model

The HEISENBERG model of ferromagnetism is based on the exchange interaction between
two neighbouring electrons, which results from the COULOMB interaction between the
electrons and the PAULI exclusion principle. The latter forbids electrons to have the same
state with the same spin alignment, meaning that the total electronic wave function of
the electrons has to be antisymmetric. The classical HEISENBERG model accounts for
fully localized electrons, where the exchange interaction between electronic spins $S_{i,j}$ on
neighbouring lattice sites (i,j) is described by the effective Hamiltonian $\mathcal{H}_{eff}$

$$\mathcal{H}_{eff} = -2 \sum_{i \neq j} J_{ij} S_i \cdot S_j \tag{2.1}$$

with the exchange coupling constant J_{ij}. The interatomic exchange coupling described
by this Hamiltonian can lead to electrons favouring parallel ($J_{ij} > 0$) or antiparallel
($J_{ij} < 0$) spin alignment, resulting in a ferromagnetic or antiferromagnetic ground state
[40].

The $3d$ FM Ni, Co, and Fe are ferromagnetic at room temperature and their magnetic
order is known to be caused by partially delocalized electrons. The HEISENBERG model
of ferromagnetism therefore fails to describe the magnetic ordering sufficiently in these
systems. Thus, a band theory was introduced by MOTT, SLATER and STONER to explain
the itinerant ferromagnetism of these elements, or rather of metals in general [43–47].

2.1.2. Itinerant magnetism of 3d ferromagnets

$3d$ FM with more than half-filled d-shells exhibit strong ferromagnetic coupling at room
temperature ($T_C = 600 - 1400\,\mathrm{K}$). Their atomic moments ($m_{exp} \approx 2.2\mu_B$ for Fe, $1.7\mu_B$ for
Co and $0.6\mu_B$ for Ni) are given by non-integer values of the BOHR magnetron, indicating
that the $3d$ electrons in these elements are not strictly localized [40]. This partial delocal-
ization of valence electrons results in a strong overlap and interaction with $3d$ orbitals of
the neighbouring atoms. In order to describe metallic ferromagnetism in these systems,
the band theory of FM was developed. The simplest of these models is the STONER model
[44], where strong hybridization of the $3d$ electrons causes the formation of bands with
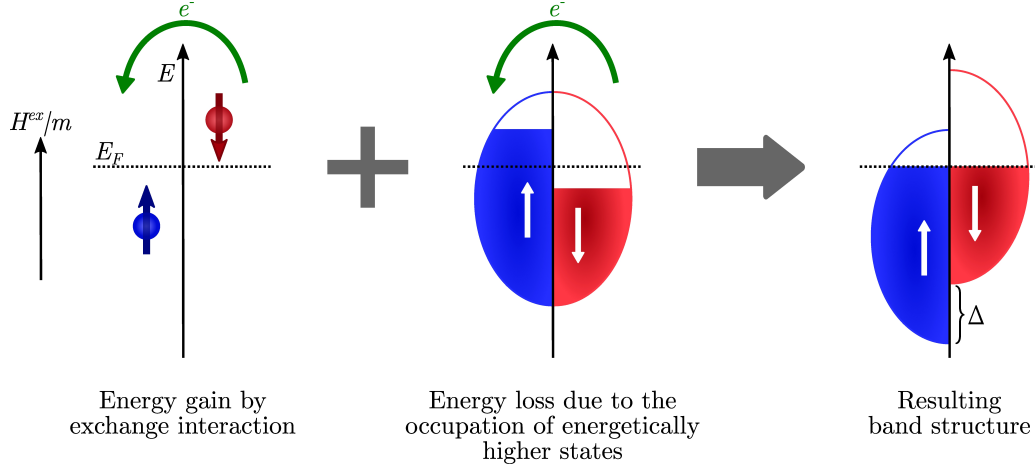
Figure 2.1. – Energy contributions to the ferromagnetic equilibrium. The left graph illustrates the lowering of the energy of an electron, due to exchange interaction, which results from a parallel spin alignment to the majority of the electrons with "spin-up" character. This results in a gain of potential energy since the electrons have a larger average distance to each other. In the middle graph, the reversal of the spin direction leads to a loss in energy, as the electrons can only access unoccupied states in the density of states (DOS), which have an originally higher energy. Contributions from both scenarios can lead to an equilibrium situation, where the bands with "majority" (spin-up) and "minority" (spin-down) character are shifted with respect to each other by the exchange splitting Δ shown in the right panel. The shaded areas in the schematic density of states represents occupied states, while uncolored areas represent unoccupied states. Adapted from [48].

"spin up" (majority) and "spin down" (minority) character. The majority and minority bands are shifted relative to each other by the exchange splitting Δ generated by the exchange field, H^{ex}, as shown in Figure 2.1. As a consequence, the exchange splitting Δ determines an imbalance in the occupation of the spin up and spin down states and the magnetic moment m of the system is determined by the difference in the number of electrons in the majority $N_e^\uparrow$ and minority $N_e^\downarrow$ bands

$$|m| = \mu_B \left(N_e^\uparrow - N_e^\downarrow \right) \qquad \text{and} \qquad \Delta = 2m \cdot H^{ex}. \tag{2.2}$$

This allows for values of the magnetic moment m which are non-integer multiples of μ_B. The number of electrons is given by the integration of the spin dependent density of states $D^\uparrow(E)$ and $D^\downarrow(E)$

$$N_e^{\uparrow/\downarrow} = \int_{-\infty}^{E_F} D^{\uparrow/\downarrow}(E)dE. \tag{2.3}$$

A criterion for ferromagnetism can be expressed by the STONER criterion [44] at zero temperature $(T = 0\,\mathrm{K})$ defined by

$$D(E_F)^{\uparrow/\downarrow} \cdot I > 1, \tag{2.4}$$

where I represents the STONER parameter and E_F the Fermi level. This criterion takes into account the competition between two forms of energy, as illustrated in Figure 2.1. The parallel alignment of spins in a ferromagnet results in a gain of potential energy, since the electrons have a larger average distance to each other (left graph). Counteracting to this process is the loss of energy for electrons that change their spin state and transition to initially higher lying unoccupied states (middle graph). The condition of the STONER criterion is fulfilled when either the density of states (DOS) around the Fermi level $D(E_F)$ or the STONER exchange parameter I, which is a measure of the exchange splitting Δ, is large.

2.1.3. Band theory results for 3d ferromagnets

The $3d$ FM exhibit a high density of states around E_F due to narrow d-bands and thereby meet the criterion in Equation 2.4. Their exchange splitting Δ is on the order of $1\,\mathrm{eV}$ [40]. While the STONER model is based on a simple semi-circle-like band structure, a more realistic representation of the spin-split DOS for Ni, Co, and Fe as calculated by *ab initio* calculations, is shown Figure 2.2.

The structure of the DOS is given by the overlap interactions of the d-states with neighboring atoms located on lattice points of well-defined symmetry. The closed packed systems Co (hcp) and Ni (fcc) display a more compact DOS compared to Fe (bcc) where the DOS shows pronounced maxima and minima. The $3d$ DOS around E_F overlaps with the dispersive sp-bands, also shown in Figure 2.2. The DOS of Ni, Co, and Fe mainly differs in the position of the Fermi energy E_F, which separates the occupied from the unoccupied states. For Ni and Co, the majority d-bands are completely pushed below E_F, while the majority states of Fe are only partially filled. This difference results in the classification of the $3d$ FM into strong (Ni and Co) and weak FM (Fe). The band splitting of the $3d$ bands leaves the shape of the majority and minority band almost unchanged. This behavior is known as "rigid band behavior" and occurs in pure metals or alloys of metals and metalloids. For alloys consisting of more than one magnetic element, such as FeNi, the electronic structure changes due to interaction between the atoms of the different elements.

Figure 2.2. – Spin-split density of states of the 3d FM Ni, Co, and Fe for d- and sp-states as calculated by *ab initio* calculations. In the strong FM Ni and Co, the majority d-states are fully occupied, while the weak FM Fe also exhibits empty majority states above E_F. The data are provided by SANGEETA SHARMA.
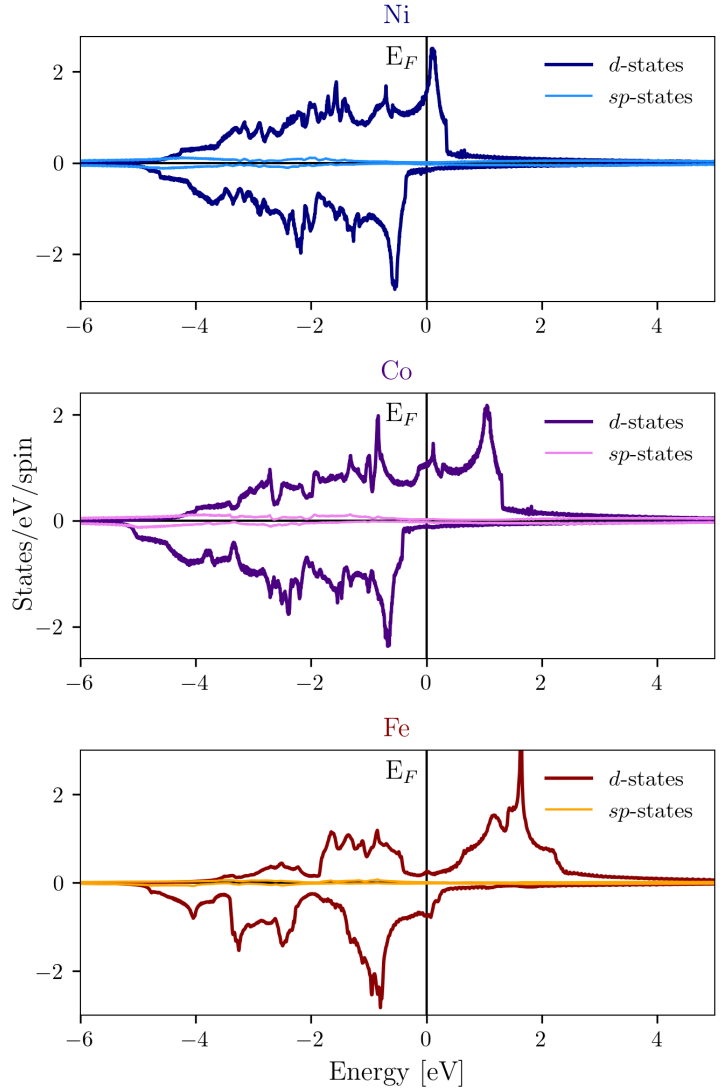
It should be noted, that the classification of 3d FM into weak and strong FM is misleading in the sense that the magnetization of Fe is larger compared to Co and Ni. The magnetic moments of the 3d FM are nearly entirely determined by d electrons and dominated by the spin moment m_s^d. The orbital moment m_o^d only accounts for less than 10% as can be seen from the calculations of ERIKSSON et al. in Table 2.1 [40, 49, 50].

Table 2.1. – $3d$ valence shell properties of Ni, Co, and Fe calculated by local density functional theory (DFT) by Eriksson [40, 49, 50]. Summarized are the number of d electrons N_e^d, the spin magnetic moment m_s^d and the orbital magnetic moment m_o^d.

	$3d$ valence shell properties		
	N_e^d	m_s^d $[\mu_B]$	m_o^d $[\mu_B]$
Ni (fcc)	8.22	0.65	0.07
Co (hcp)	7.20	1.67	0.14
Fe (bcc)	6.07	2.23	0.09

2.2. Ultrafast laser-induced demagnetization

The foundations of ultrafast magnetization dynamics were laid by BEAUREPAIRE and coworkers in their famous work on the demagnetization of ferromagnetic nickel after femtosecond laser excitation [11]. While laser-induced demagnetization was long thought to occur on the order of tens of picoseconds due to a sudden increase in lattice temperature followed by spin-lattice relaxation, BEAUREPAIRE's study showed that a ferromagnet can demagnetize on a sub-picosecond timescale. Since then, the study of ultrafast demagnetization after femtosecond laser excitation has been a very active field of research, aiming to disentangle the microscopic processes that drive the sudden reduction of magnetic moment.
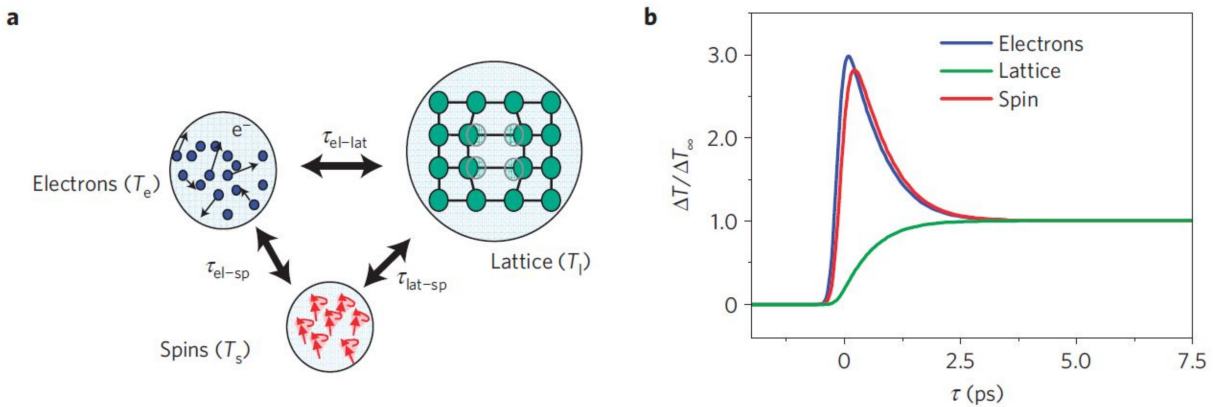

Figure 2.3. – (a) Schematic illustration of the three temperature model (3TM) and (b) simulations of the temperature change of the three subsystems (electrons, spins, and lattice) for metallic nickel. Reprinted from [51]. Reproduced with permission from Springer Nature.

BEAUREPAIRE et al. introduced a phenomenological three temperature model (3TM) to explain their discovery of ultrafast demagnetization [11]. The model is based on the division of the solid into three different reservoirs: the electron, the spin, and the lattice system with their assigned respective temperatures T_e, T_s and T_p, depicted in Figure 2.3 (a). In the framework of the 3TM, the laser excitation leads to a femtosecond-scale increase of the electronic temperature T_e, followed by thermalization and equilibration with the other subsystems. These processes are described by a set of rate equations (see Figure 2.3). This phenomenological description allows for an intuitive picture of the ultrafast demagnetization and the subsequent relaxation [11]. However, it does not provide insight into the microscopic mechanisms involved, which are of particular interest to fully understand how a magnet can demagnetize on the experimentally observed timescale.

In the following, a brief overview will be given on the proposed processes, which allow the laser pulse to influence the magnetization on a sub-picosecond timescale. In general, a distinction can be made between two types of processes: **spin-flip scattering** processes and **spin transport** processes. The former affect the angular momentum of the spin system, which is transferred directly to the lattice, while the latter assumes that excited spins leave the sample volume under investigation. As this section only provides a brief introduction to the basic concepts of ultrafast demagnetization, the reader is referred to Refs. [17, 18, 52] for a more general introduction to the theoretical descriptions of ultrafast magnetization dynamics.

2.2.1. Spin-flip processes

Spin scattering events can be understood as local effects, where the angular momentum is eventually transferred to the lattice, leading to ultrafast demagnetization. The local change of angular momentum is caused by the scattering of excited electrons with other quasiparticles in so called *Elliott-Yafet* type electron-electron, electron-phonon but also electron-magnon scattering events [53, 54]. In these events, the probability of a spin-flip is based on the idea that in the presence of spin-orbit-coupling, the eigenstate of the electron is not described by a pure "spin up" $|\uparrow\rangle$ or "spin down" $|\downarrow\rangle$ eigenstate anymore but rather by a mixture of both states:

$$|\Psi_{\uparrow\downarrow}\rangle = \alpha |\uparrow\rangle + \beta |\downarrow\rangle. \tag{2.5}$$

In consequence, the excited electron can be in a final state with mainly spin down (spin up) character, even if the initial state has mainly spin up (spin down) character [55]. This allows the electron to effectively flip its spin after a scattering event.

Electron-phonon scattering

Electron-phonon scattering events form the basis of the microscopic three temperature model (M3TM), where the spin-flip is caused by an electron-phonon scattering event. The M3TM proposed by KOOPMANS et al. extends the original 3TM by adding spin relaxation via *Elliott-Yafet*-type spin-flips, which occur with a certain probability during an electron-phonon scattering event [56]. By this means, the angular momentum is directly transferred to the lattice. It was shown that the M3TM allows for demagnetization times which are much faster than the electron-phonon thermalization. Since its development, the model has been used to successfully describe many different experimental results. Criticism of its accuracy was mainly raised due to two reasons. First, the three subsystems, electrons, spins and phonons, are assumed to be in full internal equilibrium; thus the model neglects thermalization time [36, 56]. Secondly, the model was challenged by a number of publications, where the scattering rates for the $3d$ FM Ni, Co and Fe, determined by *ab initio* calculations, were found to be too small to account for the experimentally observed demagnetization [57–59]. Thus, although electron-phonon spin-flips were found to contribute significantly to demagnetization, further processes must be involved to fully explain the experimentally determined dynamics.

Electron-electron scattering

In electron-electron scattering events, the spin-flip is mediated by a COULOMB scattering event between electrons with different spin-orientation. This model was first proposed by KRAUSS et al. and includes the material-specific band structure and a simplified model of the optical excitation [60]. In the presence of spin-orbit coupling, the scattering events lead to an inter-band redistribution of electrons from majority to minority bands and thus to a reduction of the magnetization. Electron-electron scattering simulations have been shown to be in good agreement with the demagnetization observed for ferromagnetic Co and Ni. In a later extension of the proposed model of KRAUSS et al., it was shown that an interplay of electron-electron and electron-phonon scattering processes should be considered to fully describe the demagnetization of ferromagnetic Ni [61].

Magnons

Another effect that has been discussed to drive ultrafast demagnetization is based on the HEISENBERG model of localized spins and consists of the generation of collective spin excitations, so called *magnons.* A magnon is a quantized, delocalized eigenstate of a spin wave and can be understood as a distribution of a local spin-flip over several spins with a fixed phase relation, resulting in a collective excitation. The excitation of one quantum of a magnon equals one spin-flip, but distributed over the whole electron ensemble. In terms of the DOS, magnon generation can be understood as a "mirroring" of the band structure, where the formerly majority spin band (analogous for the minority spin band) is projected onto the opposite spin direction. The role of magnon generation [62–69] to ultrafast demagnetization has for example been studied in more detail by EICH et al. [70] and TURGUT et al. [71] in Co thin films, which revealed a relevant contribution of magnon generation to the demagnetization.

2.2.2. Spin transport processes

In contrast to spin scattering processes, spin transport processes do not affect the total magnetization of the sample. The demagnetization is rather based on the idea that excited electrons are transported out of the probed region. In the context of spin transport processes, the conservation of angular momentum is not required, as the moment is transported out of the excited volume. Spin transport events are also referred to as non-local processes, as the local spin remains unchanged.

Superdiffusive spin transport

The model of superdiffusive spin currents was developed by BATTIATO et al. and allowed to successfully describe the ultrafast demagnetization of a thin Ni film by transport of excited charge into the underlying metallic substrate [72]. Since then, spin transport processes have been experimentally observed in a number of multilayer systems, reaching from Co/Pt over Au/Fe to Ni/Fe [73–79].
The demagnetization by superdiffusive spin currents is based on the excitation of electrons that propagate through the sample in a superdiffusive transport regime, whereas the transported spin remains unchanged. As majority carriers display longer lifetimes in $3d$ FM and therefore have higher mean free paths compared to minority carriers [80–82], the demagnetization is supposed to be driven mostly by transport of majority electrons out of the probed region, resulting in a reduction of the net magnetic moment. While

superdiffusive spin transport certainly contributes to ultrafast demagnetization, it cannot be the only responsible process. For example, studies of Ni on an insulating substrate showed that local dissipation processes are still relevant for the demagnetization, as spin currents into the substrate were suppressed [83]. The interplay between spin-flip scattering and spin currents to ultrafast demagnetization was further investigated, for example by TURGUT et al., for multilayers of Fe and Ni with different insulating and conducting spacer materials [78]. It was shown that the contribution of both processes depends critically on the composition of the system under investigation. The study also impressively illustrates the advantage of an element-specific technique, such as the EUV T-MOKE experiment, to reveal such dynamics in multi-elemental sample systems.

2.2.3. Optical intersite spin transfer

This thesis focuses on the study of distinct spin dynamics in elemental Ni, Co, and Fe on very early timescales after the optical excitation, where the electron system is in a far-from equilibrium state. For this reason, the recently discovered optical intersite spin transfer (OISTR), which allows the manipulation of the spin system on the timescale of the laser excitation itself, is of particular interest for the following discussion. The OISTR process represents a spin-selective charge flow between different sublattices of multi-component magnetic systems and was first introduced by ELLIOTT and coworkers by time-dependent density functional theory (TDDFT) calculations for different HEUSLER compounds [84]. It was later verified experimentally in a variety of magnetic materials, ranging from alloys and HEUSLER compounds to multilayer systems [12, 20–25].

As this will be of particular importance for the later discussion in Chapter 5, the OISTR process is explained using the example of $Fe_{50}Ni_{50}$ alloy first reported by HOFHERR et al. using EUV T-MOKE [21]. The study reveals a direct net spin transfer from the sublattice of Ni to the Fe sublattice on the timescale of the pump excitation. This transfer is schematically shown in the spin projected DOS of $Fe_{50}Ni_{50}$ in Figure 2.4 (a), which highlights that the process is highly dependent on the band structure of the different magnetic subsystems, the photon energy and the transition probability of the optical excitation. In the exemplary sample system of $Fe_{50}Ni_{50}$, the sublattice of Ni displays a large number of occupied minority states below E_F, while many empty states are available in the subsystem of Fe above E_F. Thus, the optical excitation can directly transfer minority electrons from the occupied Ni minority states to the unoccupied minority channel of Fe, leading to an ultrafast increase of the magnetic moment in Ni and
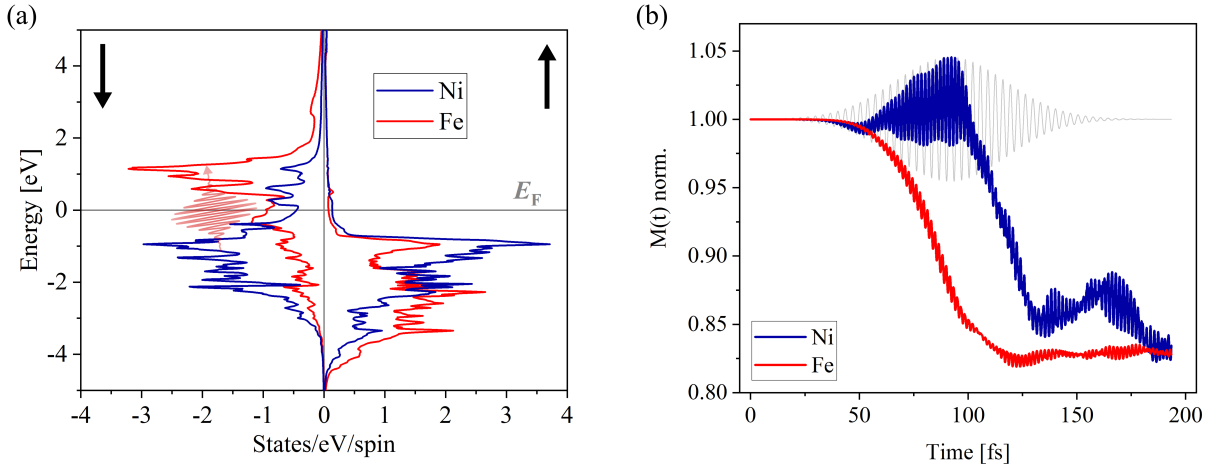
Figure 2.4. – OISTR in $Fe_{50}Ni_{50}$. (a) Spin- and element-projected projected DOS of $Fe_{50}Ni_{50}$ for Ni in blue and Fe in red. The favorable density of states around E_F allows a direct spin transfer from occupied Ni minority states to unoccupied minority states of Fe. Data adapted and reprinted from [21] in accordance with *Creative Commons Attribution NonCommercial License 4.0* (**CC BY-NC 4.0**). (b) TDDFT calculation of the change in local magnetic moment of Ni and Fe in $Fe_{50}Ni_{50}$ after excitation with a 1.2 eV pump pulse (47 fs FWHM). The magnetic moment of Ni shows a rapid increase, while the magnetic moment of Fe simultaneously decreases. The shown data was provided by Sangeeta Sharma.

a decrease in the magnetic moment of Fe (see Figure 2.4 (b)). Being a coherent spin-conserving process, which is only active during the presence of the pump pulse, OISTR represents one of the fastest mechanisms to manipulate magnetization with light and even precedes the usual demagnetization process. For a more detailed study of OISTR in FeNi alloys, I refer to the thesis of Christina Möller, who intensively investigated the spectrally-resolved spin dynamics in FeNi compounds with EUV T-MOKE experiments [85].

To sum up this section on ultrafast laser-induced demagnetization, after nearly 30 years of research in this field, different processes have been identified to contribute to ultrafast demagnetization and the associated angular momentum dissipation. However, disentangling these different types of contributions to the demagnetization process remains challenging. In this context, techniques making use of high photon energies in the EUV and soft X-ray range of the electromagnetic spectrum, which allow for an element-specific and thus spectrally-resolved analysis, have proven to be of key importance. As the OISTR example shows, the use of such techniques also makes it possible to study dynamics that occur on even faster timescales than the usual demagnetization process. While OISTR-like processes have not yet been experimentally verified in the 3d FM, such signatures can be expected to also appear in single elements, since the ultrafast excitation also drives

occupation changes in these materials. First investigations of spectrally-resolved spin dynamics in elemental FM on early timescales after the optical excitation have recently gained a lot of attention [28–30]. The next section will provide an overview of recent developments in this field, with a particular focus on studies in the EUV spectral region (M-edge magneto-optical techniques).

2.3. Spectrally-resolved magneto-optics in the far-from-equilibrium state

The previous Chapter 2.2 on ultrafast laser-induced demagnetization illustrates the immense progress that has been made in the field. The intensive study of magnetization dynamics induced by optical excitation has led to numerous promising discoveries, reaching from ultrafast spin currents [73–77] to all-optical switching of magnetic materials [13, 17]. Most existing studies focus on spin and lattice dynamics that occur on timescales where the excited system has already undergone partial thermal equilibration. Only in recent years, the study of the strong non-equilibrium state that occurs during and shortly after the optical excitation has become a new and exciting playground to investigate the competing role of electron and spin dynamics [21, 35, 86, 87].

In this regard, magneto-optical techniques that make use of light in the EUV and soft X-ray regions of the electromagnetic spectrum offer significant advantages by reaching absorption edges (M- and L-edges) that provide element sensitivity and higher magnetic contrast. Moreover, the use of EUV-light and soft X-rays also enables to investigate spin dynamics with different probing energies around the elemental absorption edges, e.g., allowing for a spectrally-resolved analysis of the given material. The latter is especially promising for the characterization of the strong non-equilibrium state after the optical excitation, i.e., for the investigation of magnetic and electronic contributions to dynamics on the sub-picosecond timescale.

2.3.1. Establishment of spectral analysis

The foundation for the spectral analysis of metallic thin films on the femtosecond timescale after optical excitation was first laid with investigations in the soft X-ray region, i.e., at the L-edges of the $3d$ FM. For instance, STAMM and KACHEL et al. measured a reshaping and an ultrafast shift of $\approx 0.15\,\text{eV}$ of the absorption spectrum at the Ni L_3-edge by soft X-ray

spectroscopy [86, 87]. Hereupon, a theoretical study by CARVA et al. explained the observed phenomenon as a result of electron redistribution around E_F caused by the optical charge excitation [35]. Their calculations further predicted that the far-from-equilibrium state should also influence the magnetic circular dichroism (MCD) spectrum of the material. While further studies of $3d$ transition metals were still limited to investigations at the L-edges [88], in 1975 ERSKINE et al. already provided theoretical predictions that transient changes of the MCD spectrum at the M-resonances could provide information about the microscopic origin of different types of spin excitations [89]. However, only recently, investigations of the spectral response at the M-edges have received more attention [22, 28, 29]. One of the first studies that made use of such spectral analysis in the EUV was conducted by HOFHERR et al. in a T-MOKE study of $Fe_{50}Ni_{50}$ [21]. They revealed the previously introduced OISTR from Ni to Fe on the timescale of the laser excitation (Chapter 2.2.3). While dynamics occurring on these few-fs-timescales are highly challenging to interpret, the $3d$ FM Ni, Co, and Fe were found to serve as ideal candidates to study the spectral response on the earliest timescales. In the following, a short review will be given on recently reported spectrally-resolved magnetization (and charge) dynamics of $3d$ FM in the EUV spectral region.

2.3.2. Time- and energy-dependent T-MOKE

The first detailed T-MOKE study investigating Ni and Fe thin films with spectral resolution was conducted by JANA et al. in 2020 using photon energies in the range of $40 - 72\,\mathrm{eV}$ [28]. In particular, the study focuses on the analysis of the relationship between the T-MOKE asymmetry and the magnetic moment, i.e., the proportionality relation between both quantities. For this purpose, Ni and Fe thin films were excited with a $800\,\mathrm{nm}$ ($1.5\,\mathrm{eV}$) fundamental pump beam and investigated with EUV light generated by high-harmonic generation. While the study does not focus specifically on the few-fs-timescales, it nevertheless provides insights into the ultrafast spin dynamics of the $3d$ FM under investigation.

In Figure 2.5 (a) and (b) the T-MOKE asymmetry time-traces for Fe and Ni from [28] are shown for energies around the corresponding M-edges. For Fe, the authors find a strong energy dependence of magnetic asymmetry time-traces, which reflects in different onsets and quenchings of the magnetization. For the harmonic energy above the M-edge ($57\,\mathrm{eV}$, marked in blue), the authors even observe an early increase of the asymmetry. In contrast to this, the magnetic asymmetry of Ni for different photon energies around

the resonance ($\approx 66\,\text{eV}$) shows a rather homogeneous behavior, as indicated in (b) by the expected demagnetization curves. The (non-)linear connection between the magnetic asymmetry and the magnetization is further investigated by the magnetization-asymmetry test ratio (MAT), for which the magnetic asymmetry at a given photon energy is divided by the magnetic asymmetry close to the M-edge of the material. For a linear relation between magnetic asymmetry and magnetization, this ratio should be independent of the magnetization and, thus, should result in a time-independent ratio. Evidently, from the asymmetry time traces, the MAT for Ni in Figure 2.5 (d) is found to be more constant than for Fe (shown in (c)). The authors infer that the magnetic asymmetry for Ni correctly describes the magnetic state of the system, while for Fe, the proportionality between the asymmetry and the magnetic moment is questioned.
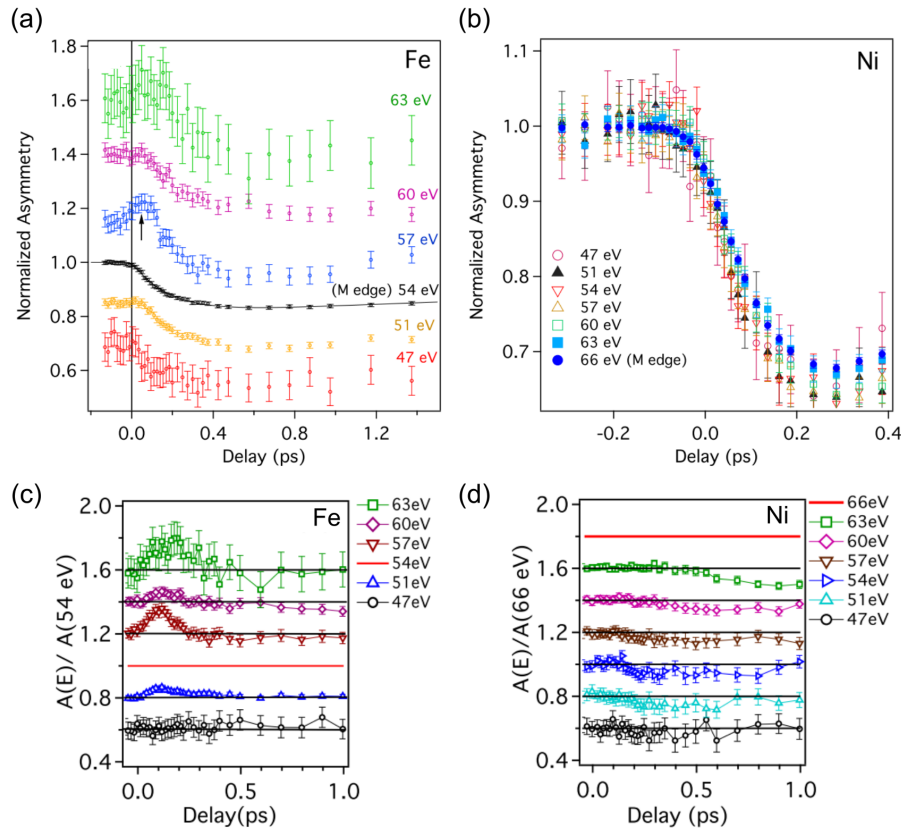

Figure 2.5. – Asymmetry time traces for various probing energies for a bcc Fe (a) and a fcc Ni sample (b) pumped with a NIR $\approx 1.5\,\text{eV}$ laser pulse with a length of $\approx 35\,\text{fs}$. The Fe asymmetry curves were shifted vertically for better visibility and exhibit strong irregularities in the energy-resolved asymmetry time-traces. In contrast, no irregularities are found for Ni, where the asymmetry time-traces homogeneously decrease. In (c) and (d) the (non-)linearity of the magnetic asymmetry is investigated with the help of the magnetization-asymmetry test ratio (see text for details), which is more constant for Ni (d) in comparison to Fe (c). For better visualization, the data was shifted along the vertical axis. Adapted and reprinted from Ref. [28] in accordance with *Creative Commons Attribution 4.0* (**CC BY 4.0**) license.

In order to investigate the relation between the T-MOKE asymmetry and the magnetic moment in further detail, *ab initio* DFT calculations of the magneto-optical response were performed for different types of magnetic excitations: long wavelength magnons, short wavelength magnons, and STONER excitations. From these calculations, a strong dependence of the transient magnetic asymmetry on the specific type of magnetic excitation was found in Fe. In contrast, the magnetic asymmetry for Ni was found to be less sensitive on the specific excitation-type. Within their paper, the authors do not provide an answer on the origin of energy-dependent dynamics in the T-MOKE signal. However, with their study, JANA et al. highlighted the important question on how the energy-resolved magnetic asymmetry should be understood and if the energy-resolved magnetic asymmetry can be directly related to the magnetization of the sample.

A direct consequence of the results of JANA et al. is the awareness that the interpretation of T-MOKE data requires careful analysis [90]. Their work highlights the need for a more fundamental investigation of spectral analysis in the T-MOKE experiment, which will be provided in the course of this thesis.

2.3.3. Time- and energy-dependent absorption and MCD

A study more focused on the spectrally-resolved dynamics of $3d$ FM and some of their alloys on the ultrashort timescale was carried out by YAO et al. utilizing helicity-dependent transient absorption and XMCD measurements [29]. The samples were probed by narrow bandwidth EUV radiation tuned to specific energies around the $M_{2,3}$-resonances (55 eV for Fe, 60.1 eV for Co, and 66.6 eV for Ni) and pumped with laser pulses with a central wavelength of 800 nm (1.5 eV). The authors report a delayed onset of the magnetization dynamics determined by the MCD response compared to the onset of charge dynamics determined by transient absorption. The delayed onset of the MCD signal amounts to several tens of femtoseconds for the $3d$ FM ((25 ± 11) fs for Ni). A higher delay compared to the single-elements was found in $Fe_{50}Ni_{50}$ alloy with $(111 \pm 50$ fs) at the Ni resonance, which can be understood as a further indication of OISTR from Ni to Fe.

As a general explanation for the delayed MCD signal, the authors propose the creation of a non-equilibrium electron distribution induced by the laser pulse, leading to a redistribution of charge around E_F. As a result of the electron redistribution, the MCD spectrum and the absorption spectrum undergo a redshift in the order of ≈ 0.15 eV. This finding is

qualitatively supported by state-of-the-art *ab initio* calculations of the absorptive part of the magneto-optical functions $\Delta\beta(E)$[2.1]. The results are also in good agreement with the aforementioned redshift of the X-ray absorption spectrum of Ni at the L_3-edge by STAMM et al. [86]. A difference between the onset of charge and spin dynamics at the M-edges was also confirmed shortly afterward by RÖSNER et al. using a two-color EUV streaking experiment to study a Fe/Cu/Ni trilayer system [90].

YAO and coworkers conclude with assigning the delay in the MCD spectrum as a result of the interplay of two competing processes:

- a shift of the MCD spectrum as a consequence of electron redistribution around E_{F}

- and a decrease of the MCD response due to the onset of the demagnetization processes.

Building on the results of YAO et al., a more detailed study of the spectrally-resolved electron and magnetization dynamics around the $M_{2,3}$-edge of elemental Ni was provided by HENNES et al. by probing with five different photon energies spanning from 64 eV to 68 eV [30]. Their work reveals a strong dependence of the transient absorption and MCD signal on the probing energy after optical excitation with 800 nm (1.5 eV, $\tau = 60$ fs) pump pulses. The time- and energy-dependent absorption and MCD traces are illustrated in Figure 2.6 and display different charge and spin dynamics for the investigated energies. By calculating the absorption for different redshifts ΔE of the static spectrum, the authors identify a maximum shift of the absorption spectrum of $\Delta E_{\mathrm{max}} = 0.15$ eV towards lower energies, consistent with previously reported results at the M- and L-edges. In the same way, a shift of the MCD spectrum on very short timescales of $< 100 - 200$ fs was determined. In agreement with the work of YAO et al., the redshift of the spectra is explained by the modification of the electronic population around E_{F} induced by the pump excitation. The largest impact of the redshift on the charge and spin dynamics is found for the energy of 65.7 eV. For this specific energy, in addition to the largest change in the absorption, also an increase in the MCD time-trace is found (see Figure 2.6).

From the different dynamics in the MCD signals, HENNES et al. emphasize that the electronic population dynamics around E_{F} are spin-dependent and that the magnetization dynamics are closely connected to the changes in the occupation of the density of states.

[2.1]Given the direct proportionality between the absorptive part of the magneto-optical function and the MCD signal: $\Delta\beta(t) \propto \mathrm{MCD}(t)$
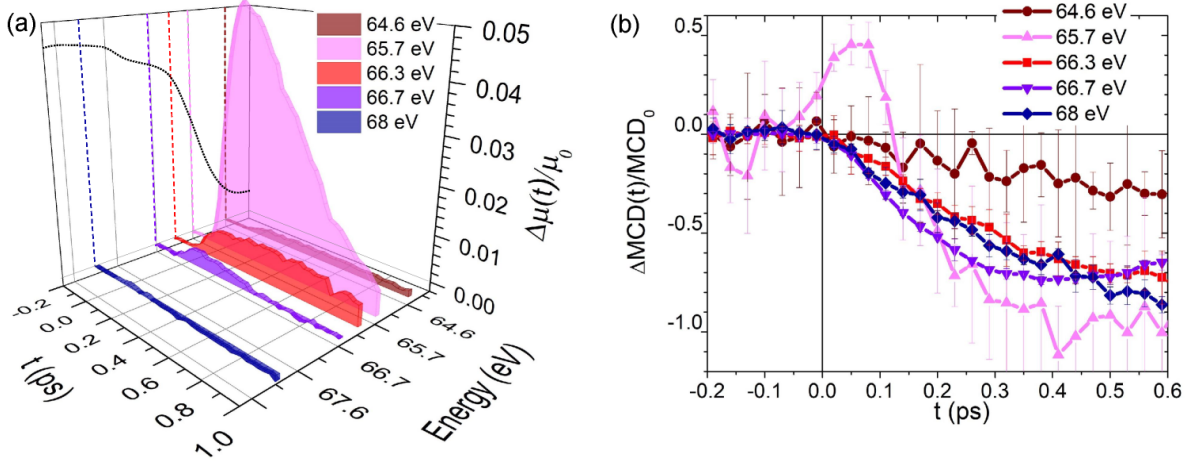
Figure 2.6. – Time- and energy-dependent absorption and MCD, reported in Ref. [30]. The transient absorption (a) and the transient MCD signal (b) strongly depend on the probing energy. For 65.7 eV, a significant increase is found for both the absorption and the MCD signal marked in pink. The MCD signal at 64.6 eV and 66.3 eV reveal a slight delay with respect to t_0. Adapted and reprinted from Ref. [30] in accordance with *Creative Commons Attribution 4.0* (**CC BY 4.0**) license.

The authors also determine a delayed onset of the MCD signal with respect to the electronic changes for energies spanning from 64.6 eV to 66.3 eV, which is in agreement with Ref. [29, 90]. At higher energies, no delay between charge and spin dynamics was found, which is explained by the fact that charge excitation and ultrafast demagnetization do not appear to compete.

In summary, the results of all the above-mentioned studies reveal the complexity of the interplay between charge and spin dynamics on the earliest timescales. While there is general agreement that different dynamics on the ultrashort timescale are induced by charge redistribution around E_{F}, leading for example to shifts in the absorption spectrum, there are indications for more complex scenarios that require further detailed experimental and in-depth theoretical analysis. All studies highlight that the far-from-equilibrium is a state that is highly challenging to interpret. While the usual demagnetization processes occur on timescales that are much longer than the optical excitation itself, the aforementioned studies demonstrate that the spin system of the $3d$ FM is also affected on these short timescales. This is not surprising, given that electrons with a certain spin are excited from occupied states below to unoccupied states above E_{F}, leading to a redistribution of spins. As shown by a photoemission study on Fe by GORT et al., these excitations are initially spin-preserving and the spin polarization is only lost after a few tens of femtoseconds [67]. Demonstrated by the experimental observation of OISTR in

a range of multi-elemental systems, these spin-conserving processes can lead to distinct fingerprints in the spin dynamics. However, so far, a clear experimental signature of such spin-conserving processes in typical ferromagnetic materials by magneto-optical spectroscopy has been elusive.

Concerning the T-MOKE experiment, the relationship between the energy-resolved magnetic asymmetry and the magnetic moment has been questioned by Ref. [28]. The arguments in Ref. [28] are part of a long-lasting debate about the presence of non-magnetic artifacts in magneto-optical signals [31–39]. Especially, the role of optical artifacts due to the hot-electron distribution generated by the pump excitation has been controversially discussed in the past. It is therefore necessary to crosscheck the validity of spectrally-resolved T-MOKE data and, in this context, also to review the relationship between different magneto-optical quantities in order to understand and correctly interpret spectrally-resolved data.

Overall, the following questions can be raised for this thesis on the basis of the review of recently published spectrally-resolved studies of $3d$ FM in the EUV spectral range:

- What is the relationship between the T-MOKE asymmetry and other magneto-optical quantities, such as the magnetization? Can we relate the T-MOKE asymmetry at a given energy directly to the energy-resolved magnetic moment?

- What is the role of charge and spin dynamics on the ultrashort timescale? Is it possible to identify OISTR-like processes within a single element?

- Can we exclude optical artifacts in the T-MOKE asymmetry?

- Is it possible to pinpoint differences and similarities in the spectral dynamics of the $3d$ FM?

Transverse magneto-optical
Kerr effect in the EUV

The aim of this chapter is to give an overview of the fundamental physics of the interaction of light with magnetic matter. The basic concepts of the magneto-optical Kerr effect in transversal geometry (T-MOKE) will be introduced, followed by a discussion of the element-sensitivity and spectral resolution in the EUV spectral range.

It should be noted that only an outline of the complex field of magneto-optics is given here. For a detailed introduction into the subject, the interested reader is referred to more in-depth literature [91–95].

3.1. Interaction of polarized light with magnetic matter

The investigation of magnetic matter with polarized light is a powerful and well-established tool to study magnetization dynamics on the sub-picosecond timescale. The foundations of the magneto-optical effects, as we know them today, were laid as early as 1845 by MICHAEL FARADAY, who observed a rotation of polarization when linearly polarized light passes through magnetic matter [1]. A few years later, JOHN KERR made an analogous observation in reflection, nowadays known as the magneto-optical Kerr effect (MOKE) [2]. Since then, the research field of magneto-optics has evolved considerably and numerous techniques were developed to study magnetization dynamics with high temporal resolution by use of different detection schemes, measurement geometries and light polarizations. The feasibility of light sources in the soft X-ray and extreme ultraviolet spectral range further enriched the research field by providing an element-sensitive probe. An overview of the wide range of magneto-optical techniques, as we know them today, is given in Table 3.1.

Table 3.1. – Magneto-optical techniques classified by the following criteria: the detection scheme, the sensitivity to the magnetization, the light polarization and the measurement geometry. $\langle M \rangle$ is the average of the magnetization of all the atoms that are measured. Adapted from [93].

Detection	Magnetic Sensitivity	Light Polarization	Geometry Transmission	Reflection
Intensity Measurement	$\langle M \rangle$	circular	XMCD	XMRS
		linear		T-MOKE
	$\langle M^2 \rangle$	linear	XMLD	XMLD type Reflectometry
Polarization analysis	$\langle M \rangle$	linear	Faraday	L- & P-MOKE
	$\langle M^2 \rangle$	linear	Voigt	QMOKE

3.1.1. Macroscopic description of the Kerr effect

While there are numerous effects that allow the investigation of light-induced changes of the magnetic properties of the material, the fundamental physics behind all of them is the same and governed by the material-specific dielectric tensor $\hat{\epsilon}$ (permittivity tensor), which relates the dielectric flux $\vec{D}$ to the applied electric field by $\vec{D} = \hat{\epsilon}\vec{E}$ [96]. For an isotropic medium, the dielectric tensor is a constant related to the refractive index by $n_0 = \sqrt{\epsilon}$. Once the material is magnetized with a magnetization $\vec{M}$, the dielectric tensor $\hat{\epsilon}$ is expressed by

$$\hat{\epsilon} = \begin{pmatrix} \epsilon_{xx} & \epsilon_{xy} & \epsilon_{xz} \\ \epsilon_{yx} & \epsilon_{yy} & \epsilon_{yz} \\ \epsilon_{zx} & \epsilon_{zy} & \epsilon_{zz} \end{pmatrix} = \epsilon_{xx} \begin{pmatrix} 1 & -iQm_z & iQm_y \\ iQm_z & 1 & -iQm_x \\ -iQm_y & iQm_x & 1 \end{pmatrix}, \quad (3.1)$$

where the projection of the magnetization on the coordinate system of the material is given by m_x, m_y and m_z. Q describes the magneto-optical constant, which is proportional to the magnetization and defined as $Q = i\epsilon_{xy}/\epsilon_{xx}$, where ϵ_{xy} are the off-diagonal tensor elements of the dielectric tensor [96]. The sign convention of the off-diagonal tensor elements is determined by Onsager relations, $\epsilon_{ij}(M) = -\epsilon_{ji}(M) = \epsilon_{ji}(-M)$ [97].

Since this thesis deals with the magneto-optical Kerr effect in transversal geometry, the following description is reduced to the reflection of polarized light from magnetized media. The Maxwell and Fresnel equations can be solved by the dielectric tensor $\hat{\epsilon}$, resulting in the reflection matrix in the Jones formalism [98]

$$R = \begin{pmatrix} r_{\mathrm{pp}} & r_{\mathrm{ps}} \\ r_{\mathrm{sp}} & r_{\mathrm{ss}} \end{pmatrix},$$ (3.2)

where the reflection coefficients (Fresnel coefficients) [98] are as follows

$$
\begin{aligned}
r_{\mathrm{pp}} &= \frac{n_1 \cos\theta_0 - n_0 \cos\theta_1}{n_1 \cos\theta_0 + n_0 \cos\theta_1} - i \cdot \frac{2 n_0 n_1 \cos\theta_0 \sin\theta_1}{n_1 \cos\theta_0 + n_0 \cos\theta_1} \cdot m_x Q \\
r_{\mathrm{ss}} &= \frac{n_0 \cos\theta_0 - n_1 \cos\theta_1}{n_0 \cos\theta_0 + n_1 \cos\theta_1} \\
r_{\mathrm{sp}} &= i \cdot \frac{n_0 n_1 \cos\theta_0 \left(m_z \cos\theta_1 + m_y \sin\theta_1\right)}{\left(n_1 \cos\theta_0 + n_0 \cos\theta_1\right)\left(n_0 \cos\theta_0 + n_1 \cos\theta_1\right)\cos\theta_1} \cdot Q \quad \text{and} \\
r_{\mathrm{ps}} &= i \cdot \frac{n_0 n_1 \cos\theta_0 \left(m_z \cos\theta_1 - m_y \sin\theta_1\right)}{\left(n_1 \cos\theta_0 + n_0 \cos\theta_1\right)\left(n_0 \cos\theta_0 + n_1 \cos\theta_1\right)\cos\theta_1} \cdot Q.
\end{aligned}
$$ (3.3)

In these expressions, θ_0 and θ_1 are the angle of incidence and the angle of refraction. n_0 is the refractive index of a non-magnetic medium and n_1 the refractive index of the magnetic medium.

The Fresnel coefficients r_{ps} and r_{sp} describe a rotation of the polarization and are proportional to m_y and m_z, whereas r_{pp} and r_{ss} give access to intensity changes of the reflected signal. From Equations 3.3, we only find r_{pp} to be proportional to the magnetization for $\vec{M}$ pointing along the x-axis. The signal is maximized, when $|m_x| = 1$, which is the case in the geometry of the **transverse** magneto-optical Kerr effect. As r_{ss} only contains optical contributions, the T-MOKE geometry only allows measuring changes in magnetization using p-polarized light. The T-MOKE measurement geometry is shown in Figure 3.1 together with the geometries for the polar and linear MOKE.

In usual experimental conditions, the non-magnetic medium is given by vacuum, i.e., $n_0 = 1$. The accessible quantity is the intensity upon reflection from the magnetic medium,
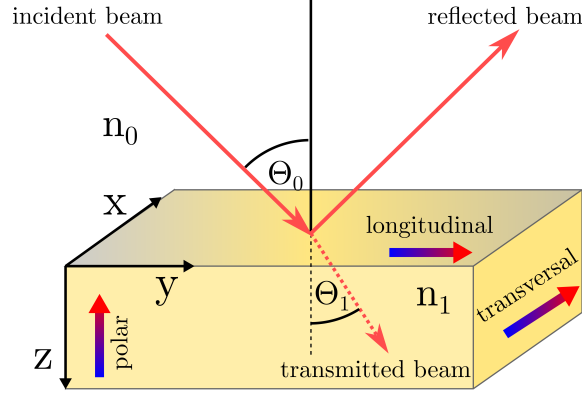
Figure 3.1. – Sketch for the derivation of the magneto-optical Kerr effect. The magnetic field directions for the different MOKE geometries are indicated by red–blue arrows. For the geometry of interest, the transversal MOKE, the magnetization is perpendicular to the plane of incidence and parallel to the surface of the sample. Adapted from [98].

which for p- and s-polarized light can be expressed by

$$I_{\text{p-pol}}^{\pm} = I_0 \cdot \left| \frac{n \cos \theta_0 - \cos \theta_1}{n \cos \theta_0 + \cos \theta_1} \pm \frac{2 \sin \theta_0 \cos \theta_0}{n^2 (n \cos \theta_0 + \cos \theta_1)^2} \epsilon_{xy} \right|^2 \tag{3.4}$$

$$= I_0 \cdot |R_{0,\text{p-pol}} \pm R_M \cdot \epsilon_{xy}|^2$$

and

$$I_{\text{s,pol}} = I_0 \cdot \left| \frac{\cos \theta_0 - n \cos \theta_1}{\cos \theta_0 + n \cos \theta_1} \right|^2 \tag{3.5}$$

$$= I_0 \cdot |R_{0,\text{s-pol}}|^2,$$

where n denotes the refractive index of the magnetic material, I_0 the incoming light intensity and $\theta_1 = \sin^{-1}(\sin \theta_0 / n)$ [37]. For the T-MOKE experiment with p-polarized light, the $\pm$ sign in Equation 3.4 refers to opposite directions of the magnetic field. Note, that the term $R_{0,\text{p-pol}}$ represents precisely the Fresnel coefficient for reflected polarized light on a non-magnetic material and contains the purely optical contributions to the signal. Usually, $R_{0,\text{p-pol}}$ dominates over $R_M \cdot \epsilon_{xy}$, except near the absorption edges of the magnetic material, where ϵ_{xy} is significantly enhanced. The off-diagonal tensor element ϵ_{xy} of the permittivity tensor of Ni is shown in Figure 3.2.

Figure 3.2. – *Ab initio* calculations of the off-diagonal tensor element ϵ_{xy} of the permittivity tensor of Ni around the M-edge. The M_3-edge around 66 eV is indicated by the dashed line. The data was provided by SANGEETA SHARMA.
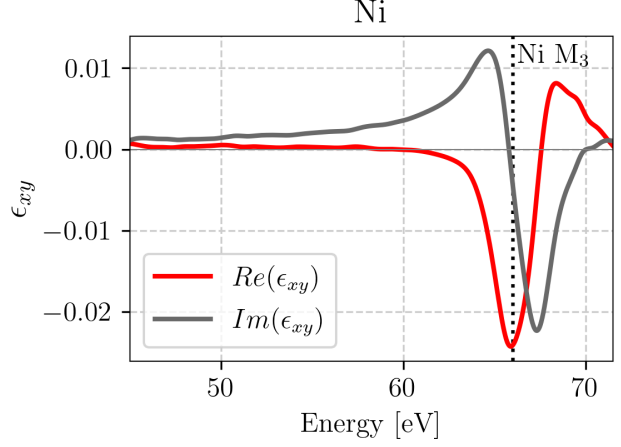
3.1.2. Magnetic asymmetry

The measurement quantity in the T-MOKE experiment is the magnetic **asymmetry** parameter, which is defined by the normalized difference of the reflected intensities for opposite directions of the magnetic field. By taking the difference of the reflected intensities I^+ and I^-, the optical contribution $|R_{0,\text{p-pol}}|^2$ (expression now shortened to $|R_0|^2$) is removed from the signal. The normalization to the sum removes potential fluctuations of the incoming intensity I_0. Taking the expressions of Equation 3.4 for the reflected intensities $I^\pm$, the magnetic asymmetry can be written as [28, 37, 99, 100]

$$
\begin{aligned}
A_{\text{TMOKE}} &= \frac{I_+ - I_-}{I_+ + I_-} \\
&= \frac{2 \cdot \text{Re}\left(R_0^\star \cdot R_{\text{M}}\epsilon_{xy}\right)}{|R_0|^2 + |R_{\text{M}}\epsilon_{xy}|^2} \qquad (3.6) \\
&\approx \frac{2 \cdot \text{Re}\left(R_0^\star \cdot R_{\text{M}}\epsilon_{xy}\right)}{|R_0|^2} \qquad (3.7) \\
&= 2\text{Re}\left[\frac{\sin(2\theta_0)\epsilon_{xy}}{n^4 \cos^2\theta_0 - n^2 + \sin^2\theta_0}\right]. \qquad (3.8)
\end{aligned}
$$

In line 3.7 the asymmetry parameter is simplified by assuming that $|R_0|^2$ is significantly larger than $|R_M\epsilon_{xy}|^2$.

The asymmetry maximizes when the denominator approaches zero, which is exactly the case near the Brewster angle $\theta_B \approx 45°$. The asymmetry shape and even the sign of the asymmetry are thereby strongly dependent on the angle of incidence θ_0, which has

27

already been demonstrated in a number of previous works [71, 101, 102]. In Chapter 5 we will introduce a different approach to express the magnetic asymmetry, which allows us to understand how the asymmetry can change its sign at a given energy within a relatively small angle range.

It should also be noted that in the past, the asymmetry was often treated as linear in ϵ_{xy} and therefore linear with respect to the magnetization. However, we emphasize that the asymmetry in Equation 3.8 is certainly connected to ϵ_{xy} but not directly linear to it. The relationship between the T-MOKE asymmetry and the magnetization therefore needs to be reconsidered with care. In Chapter 5, we will provide an overview on the connection between the asymmetry parameter and other magneto-optical quantities such as the magnetization or more specifically the energy-resolved magnetic moment.

3.2. Spectral response of 3d ferromagnets in the extreme ultraviolet light range

In the following, the spectral response using light in the extreme ultraviolet range (30 eV to 250 eV [27]) will be discussed for the materials of interest, e.g., the $3d$ FM Ni, Co, and Fe. The probing of these elements with frequencies in the visible light range (400 nm to 800 nm) leads to a broad spectral response and as a result in a smeared-out magneto-optical signal. The reason for this is the large number of electronic states around the Fermi level as shown in the density of states in Figure 2.2, which allows for numerous initial and final states. As a consequence, the extraction of spectral or element-specific (in a multi-component system) information is prevented. To obtain spectral information, the use of light in the EUV and soft X-ray spectral range is advantageous and is used by a number of magneto-optical techniques, e.g., XMCD, T-MOKE and Faraday Effect.

Table 3.2. – Absorption edges of $3d$ FM Ni, Co, and Fe in the EUV spectral range. Data taken from [103].

Element	M_2 $(3p_{1/2})$ [eV]	M_3 $(3p_{3/2})$ [eV]
Fe	52.7	
Co	58.9	
Ni	68	66.2

The use of higher photon energies allows access to the absorption edges of the $3d$ FM, e.g., the M- or L-edges depending on the photon energy. Here, we focus on the M-
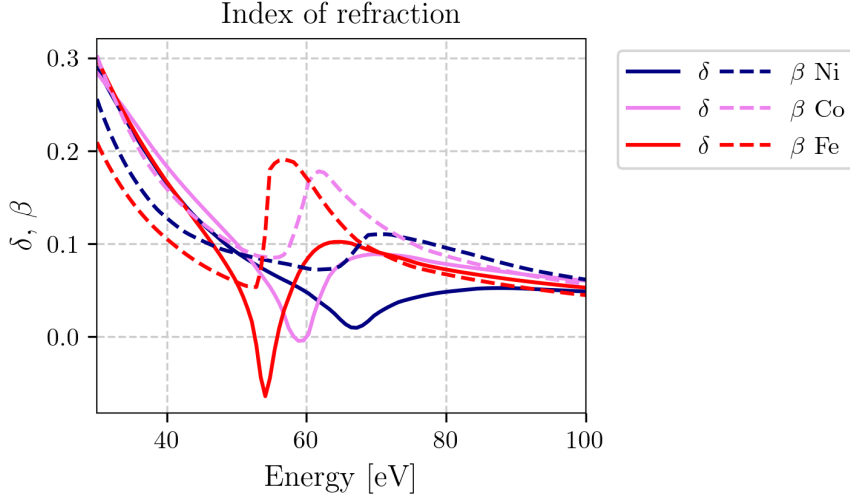
Figure 3.3. – Complex refractive index of the $3d$ FM Ni, Co, and Fe in the EUV range of $30 - 100\,\text{eV}$. Data taken from [103].

edges, which are in the EUV spectral range of our experiment between 40 and $72\,\text{eV}$. The resonant nature of the absorption edges can be illustrated by the evolution of the complex refractive index, which is defined as

$$n = 1 - \delta + i\beta, \tag{3.9}$$

where δ and β describe the dispersive and absorptive part of the light matter interaction. The refractive index in the EUV spectral range is close to unity and its resonant nature is displayed in Figure 3.3. The absorption edges lie in the energetic region where the dispersive part δ approaches zero and the absorptive part β displays a sudden increase. It is evident that the M-absorption edges of the $3d$ FM are separated by several eV, which enables to disentangle element-specific information in multi-component sample systems. A drawback in comparison to the L-edges is the smaller spin-orbit splitting on the order of $\Delta_{sp} = 1\,\text{eV}$, which prevents a clear separation of the individual edges [104–107]. Further, the well spin-orbit split L-edges allow the application of the sum rules [40, 108, 109], and thus the determination of the relative contributions of spin and orbital momenta to the angular momentum [86, 110].

3.2.1. Probing window in M-edge magneto-optical spectroscopy

The possibility to probe the magneto-optical signals of the $3d$ FM simultaneously in the EUV spectral range was demonstrated by the complex refractive index in Figure 3.3. However, a detailed analysis and interpretation of spectrally-resolved data requires a thorough understanding of the probing window in the EUV. This window is mainly determined by the initial $3p$ states. This section aims to clarify which width of the probing window can be expected in M-edge spectroscopy by using the example of Ni.
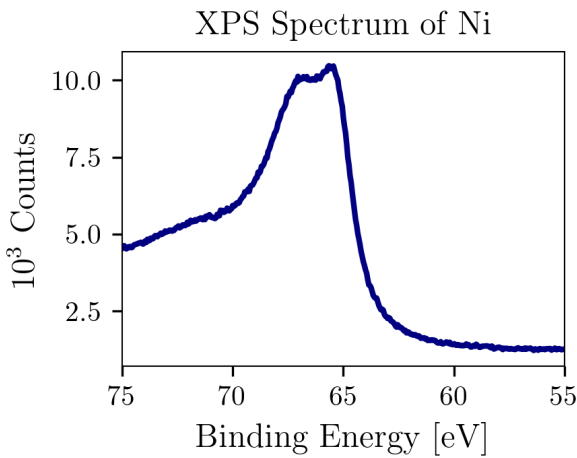
Figure 3.4. – XPS spectrum of a 20 nm Ni film on Si-substrate around the $M_{2,3}$-resonances. The exact position of the M-edges is difficult to determine due to the small spin-orbit splitting and the lifetime broadening of the $3p$ states. Fitting with a combination of Gaussian and Lorentzian distribution yields two core level states at binding energies of $E = 65.6$ eV ($3p_{3/2}$) and $E = 67$ eV ($3p_{1/2}$). The measurement was taken together with FLORIAN SCHÖNEWALD at the Institute of Material Physics, Göttingen.

The effect of spectral broadening of the $3p$ states was first discussed by ERSKINE et al. in 1975, who emphasized that the shape of the MCD spectrum in the EUV is determined by both, the shape of the final $3d$ states and the initial $3p$ states [89]. Although Ni has a relatively large spin-orbit splitting of $\Delta_{sp} \approx 1.8$ eV [103], it is still challenging to determine the exact position of each $3p_{1/2}$ (M_2-edge) and $3p_{3/2}$ (M_3-edge) state, as can be easily seen from the exemplary X-ray photoelectron spectroscopy (XPS) spectrum of

Table 3.3. – Life-time broadening of $3p$ core levels determined by photoemission spectroscopy by NYHOLM et al. [111].

Element	Broadening of	
	$3p_{1/2}$ [eV]	$3p_{3/2}$ [eV]
Fe	1.22	0.44
Co	1.26	0.71
Ni	1.19	1.19

a 20 nm Ni thin film in Figure 3.4. In fact, the individual peaks of both states can hardly be separated and fitting them accurately is a challenging task. Hence, different values for the M-edges of the $3d$ FM can be found in the literature. The reason for the strong overlap of the $3p$ doublet is found in the large lifetime broadening of these states. For Ni, the lifetime broadening was determined to a value of 1.19 eV for both edges by means of photoemission experiments (see Table 3.3 for all $3d$ FM) [111].

This relatively large lifetime broadening has a direct consequence on the probing window in EUV spectroscopy, which consequently cannot be assumed to be narrow-bandwidth. Rather, the EUV probe results in a broadband measurement of the unoccupied states around E_{F}. In other words, the same photon energy can probe different transitions to the $3d$ states of the given material, as shown in Figure 3.5 by two identical purple arrows.
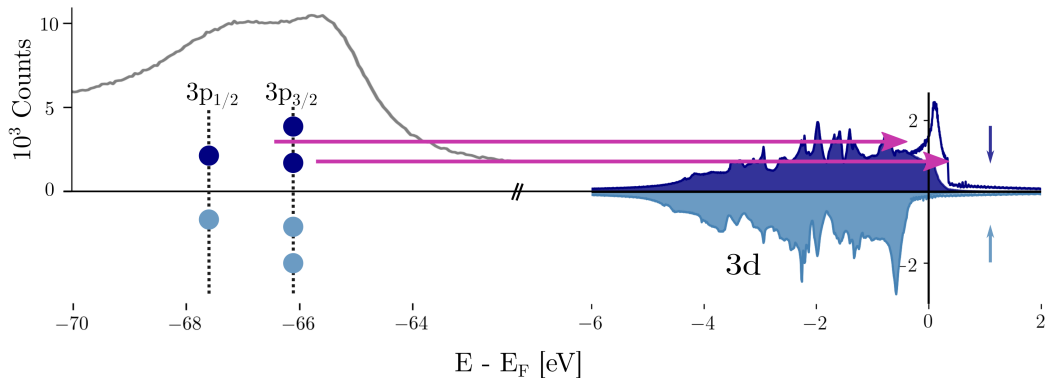
Figure 3.5. – Representation of the broad-band probing window induced by the shape and width of the initial $3p$ states of Ni. The same photon energy, depicted by purple arrows, can probe different final states around E_{F}. Here, the broadening of initial states is visualized using an XPS spectrum from a 20 nm Ni thin film. The broad probing window results in a large combination of initial and final states, and thereby smears the spectrally-resolved signal in the EUV spectral range. Shaded areas in the DOS of Ni indicate occupied states, and unshaded areas indicate unoccupied states above E_{F}.

3.2.2. Static magneto-optical signal

The static magneto-optical signal results from photo-excited electrons of the $3p$ core states to the unoccupied and spin-split $3d$ states, which serve as a kind of „detector". Thus, as stated by ERSKINE et al., the static magneto-optical response is determined by both the shape of the initial and final states [89]. The origin of the magneto-optical signal can be understood by the two-step model introduced by STÖHR and WU for circularly polarized light [112]. In a first step, electrons are excited from the $3p$ states. Due to spin-orbit coupling, the photon spin can partly be transferred to the excited electrons, which results in spin-polarized photoelectrons with opposite polarization at the individual edges (by convention from the literature at the L-edges, the sign is positive for the $3p_{3/2}$ (M_2-edge) and negative for the $3p_{1/2}$ (M_3-edge) state) [24, 40, 113]. The transition probability then depends on the DOS of the given material, i.e., the unoccupied d-states around E_F and the optical transition matrix elements [89, 114]. In a ferromagnet and thereby in the presence of exchange splitting, these final states are dominated by empty minority states, as the majority states are almost fully occupied (see Figure 3.5). This imbalance in the number of available final states results in a different absorption for both edges with opposite signs. For the M-edges of the $3d$ FM, the spin-orbit coupling is small and thus the absorption signals of both edges overlap, which leads to a reduced amplitude of the overall signal and possible sign changes depending on the shape of the initial states [24, 113].

A visualization of the contribution of both M-edges to the magneto-optical signal is given in Figure 3.6, where WILLEMS et al. theoretically calculated the absorption for left and
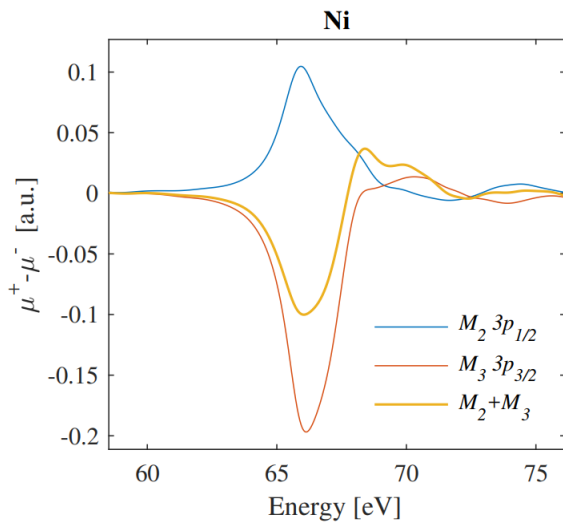

Figure 3.6. – Difference in the absorption of circularly polarized light with different helicities for the example of Ni. The absorptions from the M_2- and M_3-edges are different in amplitude and in sign. The contributions from both edges energetically overlap, and the sum MCD signal is therefore reduced in amplitude and exhibits a sign change towards higher energies. Reprinted figure with permission from [24]. Copyright (2019) by the American Physical Society.

right circularly polarized light for the M_2- and M_3-edges of Ni individually [24, 40]. The MCD signal for each edge can be understood as the difference in the absorption for both helicities. As shown, the M_3-edge has a larger contribution to the magneto-optical signal compared to the M_2-edge. The total MCD is the sum signal of both core levels. It is therefore reduced in amplitude and exhibits a sign change towards higher energies.

Although the two-step model and the presented absorptions for both M-edges in Figure 3.6 apply to the measurement principle of MCD, some general statements can be applied to the EUV T-MOKE signal with linearly polarized light (which is a combination of right and left circular polarized light):

- The static T-MOKE asymmetry is determined by the shape of the initial $3p$ states and the final unoccupied $3d$ states.

- Due to the small spin orbit coupling and the lifetime broadening of the M-edges, the static magneto-optical signal should be understood as a mixed signal with contributions from both edges. This is clearly visualized by Figure 3.6.

- The static T-MOKE signal in the $3d$ FM is always dominated by transitions of minority electrons, since the number of empty majority states above E_F is small, as shown in Figure 3.5.

We can now understand that only the unoccupied final states are relevant for the magneto-optical signal, i.e., T-MOKE probes the imbalance of unoccupied majority and minority spin states around E_F, which in the $3d$ FM displays large differences due to the exchange splitting. In the case of the strong FM Ni, free states are almost only to be found in the minority channel, and they are confined to an energy range of $< 1\,\mathrm{eV}$ around the Fermi level, as shown by the unshaded region in the density of states in Figure 3.5. However, the magneto-optical signal is also influenced by the shape of the initial $3p$ states and spreads over a much larger energy range of several eV, as visualized by the static T-MOKE asymmetries of the $3d$ FM in Figure 3.7. Therefore, the measured magneto-optical signal at a given energy cannot be directly assigned to the spin polarization of a particular energy in the DOS. This fact is of particular relevance to the later discussion of spectrally-resolved T-MOKE data.

The static T-MOKE asymmetries for the $3d$ FM were measured at an angle of incidence of $\theta_0 \approx 45°$ with our experimental setup, which will be introduced in Chapter 4. As expected, the T-MOKE signal is most pronounced around the M-absorption edges indicated by
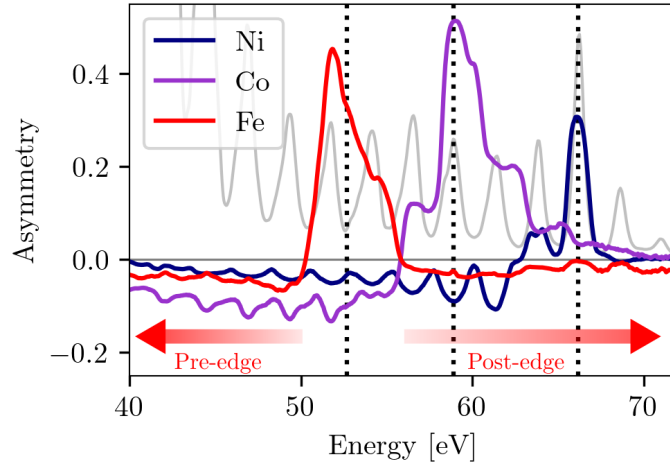
Figure 3.7. – Static magnetic asymmetries of the 3d FM Ni, Co, and Fe. The magneto-optical signal is maximized around the resonances of the given elements, which are indicated by dashed lines. Note that all asymmetries exhibit a sizeable off-resonant signal below (pre-edge) and, in the case of Fe and Co, also above the resonance (post-edge). The pre-edge and post-edge regions are indicated exemplarily for Fe. In these off-resonant parts of the magnetic asymmetries, the magneto-optical signal of the 3d FM overlaps. An exemplary high harmonic spectrum, consisting of harmonic energies separated by 2.4 eV, is shown in gray. The lack of photons in between the individual harmonics results in a valley-structure of the magnetic asymmetries between the harmonic energies. The range between the harmonics is therefore not representative of the actual magnetic asymmetries.

dashed lines in Figure 3.7. Note that the shape and the magnitude of the asymmetry around the resonances strongly depends on the angle of incidence[3.1]. This will be discussed later for the example of Ni in Chapter 5.

Origin of the large off-resonant signal

Most surprising is the observation of a large off-resonant signal extending from the lowest measured energy of 40 eV up to the resonances of the 3d FM. For Fe and Co, the off-resonant contribution also extends to energies above the resonance. This non-negligible contribution to the T-MOKE asymmetry has the opposite sign compared to the signal around the resonances and causes the magneto-optical signals of the individual elements to overlap. This fact should be taken into account for the analysis of multi-component systems such as multi-layers or alloys. While a certain broadening of the magneto-optical signal can be expected from the shape of the initial 3p states, it cannot account for the observed contributions far below and above the resonances (more than 20 eV in the case

---

[3.1]Additionally, the shape and magnitude of the magnetic asymmetry can be influenced by additional capping layers and the sample thickness.

of Ni).

A plausible explanation for the off-resonant signals in the pre-edge part of the spectrum was found in so-called off-resonant transitions. These off-resonant transitions are defined by transitions from occupied $3d$ states to higher-lying $4sp$-states, as indicated in Figure 3.8. This assumption was supported by *ab initio* calculations of the $3d$ FM in Ref. [24], where the pre-edge magneto-optical signal vanishes, when high-lying states (more than $20\,\mathrm{eV}$ above E_F) are not included into the calculations. As the final $4sp$ states are barely spin-polarized, these transitions consist of contributions from majority and minority carriers from below E_F. Thus, the off-resonant magneto-optical signal below the resonance can be understood as a probe of the overall magnetization of the sample, comparable to magneto-optical measurements with visible light.
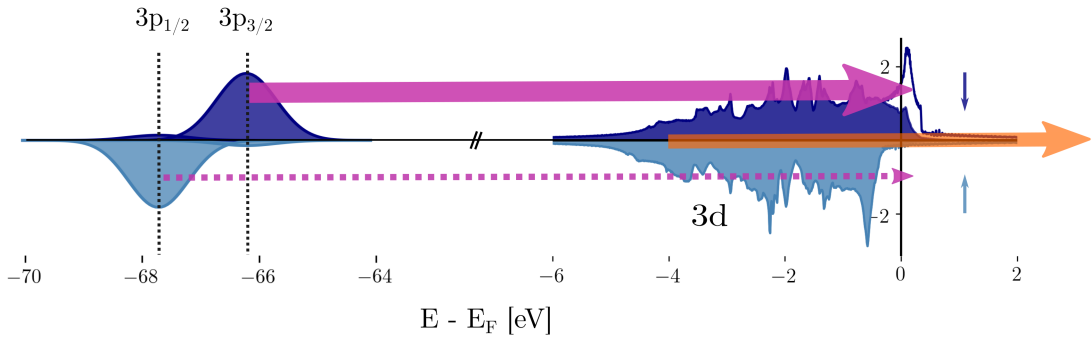
Figure 3.8. – Origin of the magneto-optical signal in the EUV spectral range. Due to the exchange-splitting of the $3d$ states, there are significantly more unoccupied minority states (uncolored area in the DOS of Ni). The absorption from the $3p$ states is therefore dominated by minority electrons (solid purple arrow) as compared to the absorption of majority electrons (dashed purple arrow). Transitions from the $3d$ states to higher-lying unoccupied $4sp$ states also contribute to the absorption and lead to an off-resonant pre-edge signal (orange arrow). The thickness of the arrows shall illustrate the transition probabilities. The broadening of the spin-resolved DOS of the $3p$ states is visualized by Gaussian envelopes with a width of $1.3\,\mathrm{eV}$. Adapted from [113].

Overall, the static magneto-optical T-MOKE signal consists of the following contributions (see Figure 3.8):

- At the resonance, the magneto-optical signal is dominated by transitions from the $3p$ states to the unoccupied $3d$ states, with a significantly larger contribution of transitions of electrons with minority character.

- In the pre-edge region, the magneto-optical signal is determined by the absorp-

tion of electrons from occupied $3d$ states to high-lying $4sp$ states, as reported by
WILLEMS et al. [24].

- The origin of the post-resonant signal found for Fe and Co far above the resonance
  cannot conclusively be determined within the scope of this thesis.

In summary, the transverse MOKE in the EUV spectral range is a powerful technique
to study magnetization dynamics with element-specificity. For the analysis of spectrally-
resolved data, the probing window of the initial $3p$ states needs to be considered, which
results in a smearing over all possible transitions with the same photon energy. It is
therefore not expected that subtle photo-induced changes in the occupation of the DOS
around E_F can be captured, as will also be shown later in Chapter 5. This fact, however,
does not apply specifically to the T-MOKE technique, but rather to all EUV and X-ray
magneto-optical techniques.

Furthermore, it should be pointed out that the T-MOKE asymmetry parameter in Equa-
tion 3.8 was found to be connected to the off-diagonal dielectric tensor ϵ_{xy} but not to
be directly linear to it. The relation between the T-MOKE measurement signal and the
magnetization is therefore more complex, and will be reviewed in detail in Chapter 5.

EUV T-MOKE setup

One of the main tasks of this thesis was to build up a new EUV T-MOKE setup based on a high repetition rate fiber laser. This novel EUV T-MOKE setup was constructed and built up in a joint effort together with Christina Möller and Johannes Otto. The successful operation and excellent performance of the setup was demonstrated by temperature- and time-dependent measurements of the magnetic asymmetry and published in the paper titled.: "Ultrafast element-resolved magneto-optics using a fiber-laser-driven extreme ultraviolet light source" [115]. Significant parts of this chapter are replicated from this publication in accordance with *Creative Commons Attribution 4.0* (**CC BY 4.0**) license and are marked with [†]. The author of this thesis contributed as follows to the publication: The author performed the corresponding measurements together with Christina Möller, carried out the analysis of the temperature-dependent static data on La_2NiMnO_6, took part in the interpretation of the data and contributed significantly to the writing of the manuscript. The measurement software and the processing of the measurement data for further analysis was developed by Johannes Otto in the framework of his master thesis. The correction of the distorted spectrum in the data analysis was implemented by Matthijs Jansen.

The chapter is structured as follows: The description of the setup is taken from Ref. [115]. Modifications of the original setup to meet the requirements of angle-resolved measurements and reflectivity measurements with s-polarized light are discussed in separate sections. The chapter closes with the benchmarking of the system by presenting energy- and time-resolved measurements of the magnetic asymmetry and the s-polarized reflectivity of a thin Ni film.

4.1. Setup for time-resolved T-MOKE at EUV wavelengths

In this section, we introduce a novel setup to measure the transverse magneto-optical Kerr effect and transient reflectivity in the extreme ultraviolet spectral range based on a fiber laser amplifier system with a repetition rate between 100 and 300 kHz. The setup is equipped with a strong electromagnet and a cryostat, allowing measurements between 10 and 420 K using magnetic fields up to 0.86 T.

4.1.1. The fiber-laser HHG light source

[†] Here, we present a T-MOKE setup using EUV light from a high-harmonic generation (HHG) light source to probe the sample. Ultrafast (de)magnetization dynamics are induced by tuneable pump pulses from the same high repetition-rate fiber laser system used to drive the HHG. After reflection from the sample, the EUV light is dispersed in a custom-built spectrometer and the diffracted harmonics are detected by a CCD camera. A schematic overview of the setup is shown in Figure 4.1.
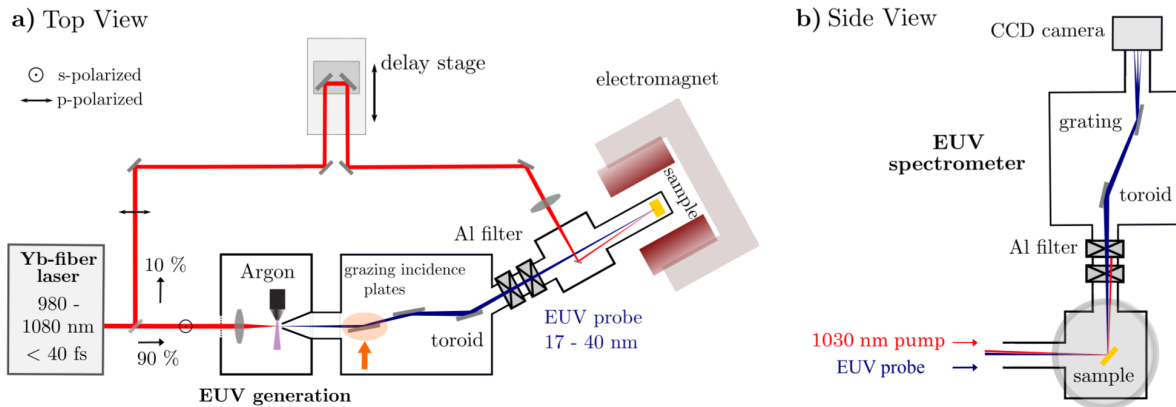
Figure 4.1. – Schematic overview of the setup: a) Top view: High harmonics are generated in an argon gas jet by intense IR pulses at a repetition rate up to 300 kHz. The fundamental beam is consequently filtered out by two grazing-incidence plates and an Al filter. The toroidal mirror focuses the EUV beam onto the sample inside the electromagnet. The first grazing-incidence plate marked by an orange arrow was later exchanged by a grazing-incidence plate optimized for *p*-polarized light in order to allow for pure reflectivity measurements. b) Side view: After reflection on the sample, the high harmonic spectrum is analyzed by our custom-built spectrometer composed of a toroidal mirror, a grating and a CCD camera. The pump beam is coupled into the vacuum chamber and blocked by a second Al filter after reflection on the sample. Note that the grating dispersion is shown to be in plane for visualization purposes and is in fact normal to the drawing plane. Adapted from [115] in accordance with *Creative Commons Attribution 4.0* (**CC BY 4.0**) license.

$\dagger$ Ultrashort laser pulses with a center wavelength of 1030 nm, tuneable repetition rate up to 300 kHz, pulse energy of up to 150 µJ and pulse lengths below 40 fs are generated by a fiber laser system (Active Fiber Systems). This is achieved by self-phase modulation of 300 fs pulses from an ytterbium-doped fiber amplifier in a krypton-filled hollow-core fiber and subsequent compression by chirped mirrors. The beam is split into a pump and a probe beam by a variable attenuator, consisting of a $\lambda/2$-plate and two broadband thin film polarizers. The s-polarized output of the attenuator is focused by a 100 mm focal length lens into an argon gas jet to generate high harmonics, which provides the probe beam in our experiment. In order to optimize the HHG process, the gas jet is mounted on a 3-axis positioning system. Efficient HHG was observed at an argon backing pressure of 17 bar for a gas nozzle diameter of 100 µm.

$\dagger$ Pumping of the HHG generation chamber is realized by placing a small conical aperture directly opposite to the gas outlet close to the HHG generation point, which already removes most of the gas load. In addition, a second bypass removes residual gas, leading to a pressure of 1.1 mbar in the generation chamber. To allow for high vacuum conditions in the mirror chamber, a 1 mm differential pumping aperture is placed less than 2 mm from the generation point. This yields a pressure of 2×10^{-4} mbar in the mirror chamber. The generated high harmonics are separated from the fundamental by two grazing-incidence plates (GIP) [116]. These fused silica plates are anti-reflection coated for 1030 nm on the front and backside, whereby most of the fundamental beam is transmitted and dumped outside the vacuum chamber. An additional top Ta_2O_5 coating of the GIP allows for a high reflection (76% calculated reflectivity for 54.2 eV) of the EUV spectrum at 10° grazing incidence. After the GIPs, a B_4C-coated toroidal mirror (276 mm focal length at 15° grazing incidence angle, 74% calculated reflectivity for 54.2 eV) focuses the probe beam onto the sample in a 350×140 µm² spot ($1/e^2$-diameter). The EUV light then passes a 100 nm thick aluminum filter which is mounted in front of the sample in a VAT valve to block any residual fundamental light.

$\dagger$ The generated EUV photon flux was estimated to be 1.9×10^{10} photons/second/eV assuming a reflection of 8×10^{-5} on a $Fe_{19}Ni_{81}$ sample [103] for 54.2 eV. This corresponds to an average generated power of 0.16 µW, and 4.6×10^9 photons/second/eV at the sample for the 45th harmonic.

4.1.2. Modification of the probe beam line for time-resolved reflectivity measurements

The original T-MOKE setup, as described in Ref. [115] was further modified to allow reflectivity measurements with *s*-polarized (with respect to the sample) high harmonics. For this purpose, the first grazing-incidence plate (GIP) in the mirror chamber was exchanged by a grazing-incidence plate optimized for *p*-polarized light (see Figure 4.1). The GIP consists of a fused silica plate with anti-reflection coating for 1030 nm on the front and backside[4.1]. The polarization of the incoming beam can be adjusted by a half-wave plate placed in front of the HHG chamber. For both polarizations (*s* and *p*), we find the combination of the two GIPs, each optimized for one polarization, to work sufficiently well, i.e., any residual fundamental beam light is blocked by the subsequent aluminum filter.

This modification of the setup represents a significant improvement to the already existing setup, as it allows easy change from measurements of the magnetization (T-MOKE with *p*-polarization) to measurements of the reflectivity (with *s*-polarization). In addition to measurements of magnetization dynamics, this also provides the potential to access pure charge dynamics of the system under investigation.

4.1.3. Pump beamline

[†] A second variable attenuator in the pump beamline allows for manipulation of the pump beam intensity. A motorized delay line changes the optical path length with respect to the probe path. After passing a 350 mm focal length lens, the pump beam is coupled into the vacuum chamber such that the angle between the pump and the EUV beamline is less than 2°. The beam diameter on the tilted sample was determined to be 760x1020 µm^2. The pulse duration is measured by intensity autocorrelation to be 58 fs, assuming a Gaussian pulse shape. The pump beam is *s*-polarized with respect to the plane of incidence on the sample for the measurements shown in this paper.

[4.1]The GIP is optimized for incidence angles between 75-80°. At 80° the reflection for 1030 nm was determined to be $< 0.5\,\%$ [117]

4.1.4. Sample environment

† The sample environment is a custom-made chamber based on a CF150 flange and designed to fit in the 45 mm wide pole gap of the electromagnet (see Figure 4.2). The flange can be opened from the side, which enables easy access to the sample. For this purpose the electromagnet surrounding the sample chamber is mounted on rails, allowing to remove the magnet and providing unobstructed access to the sample chamber. The switching time of the electromagnet varies from 60 ms for 100 mT up to 600 ms for the maximum field strength of 860 mT.

† The samples are mounted on a removable copper sample holder attached to a cryostat, which is fixed at a 45° angle with respect to the incoming pump and probe beams. In order to make small changes to the position and angle of the sample, the cryostat is attached to the chamber with an ultrahigh vacuum (UHV) port aligner. The continuous-flow UHV cryostat (Janis Research ST400) enables temperature control of the sample in the range of ≈10 to 420 K. Typically, the pressure inside the chamber is below 1×10^{-7} mbar during operation, however, even UHV conditions can be achieved by baking out the vacuum chamber.

† To verify spatial overlap of the pump and probe beam, the diffuse reflection of the pump and fundamental of the high harmonics on the sample is imaged with a CMOS sensor. The temporal overlap is achieved by observing sum frequency generation of both IR pulses in a beta barium borate (BBO) crystal at the sample position or recording interference fringes with a beam profiler. Both of these methods can be performed outside of the vacuum
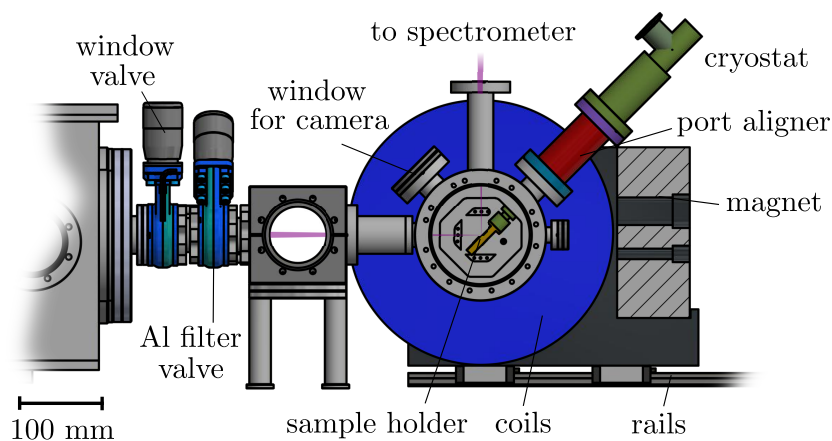

Figure 4.2. – Technical drawing of the custom-built sample chamber, providing a view directly into the sample chamber. Reprinted from [115] in accordance with *Creative Commons Attribution 4.0* (**CC BY 4.0**) license.

system by inserting a moveable mirror directly in front of the sample. This determination
of the temporal overlap is limited by a small difference in the optical path lengths of the
fundamental and the high harmonics. Therefore, a final determination of the temporal
overlap is done by searching for the onset of demagnetization as probed by the EUV light.

4.1.5. Adjustment of the angle of incidence

For the purpose of measurements with different incidence angles, the experimental setup
was extended with a new sample holder system in the sample chamber shown in Figure 4.3.
The sample is mounted on a motorized, non-magnetic and UHV-compatible tip-tilt sample
holder (SMARACT GMBH) which allows precise tilting of the sample with respect to the
plane of incidence. With this new sample holder system, the angle of incidence θ_i can
be adjusted easily from outside the vacuum chamber. A disadvantage of the new sample
holder compared to the cryostat is the loss of temperature control.

While it is challenging to determine the exact angle of incidence θ_i (close to 45°), the total
angle scan range can be estimated to be up to $\approx 2.5°$, with a step size of $\approx 0.2°$ between
the individual scan-positions. In order to obtain this estimate, an alignment laser was
adjusted onto the sample (near normal incidence) through the window flange opposite to
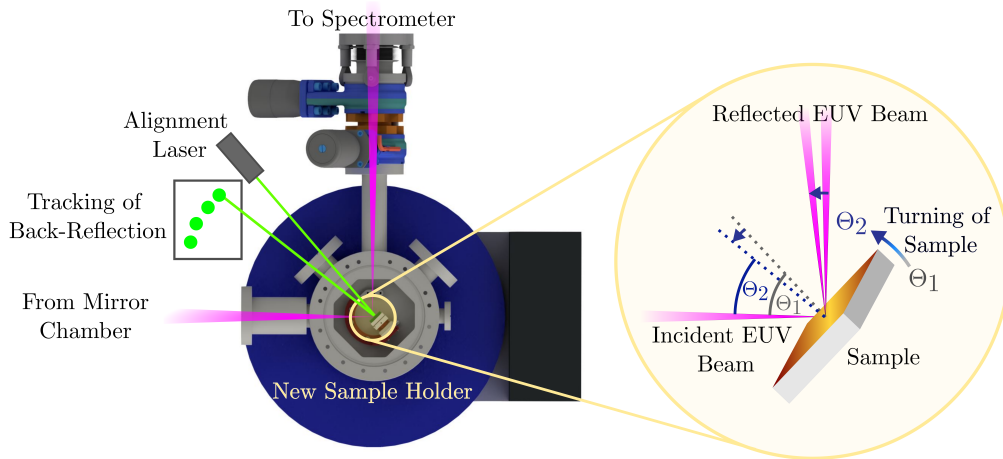
Figure 4.3. – Technical drawing of the custom-built sample chamber with the new sample holder
system. The sample holder mounted on the cryostat is exchanged by a motorized, non-magnetic and
UHV-compatible tip-tilt sample holder (SMARACT GMBH). The new sample holder system allows an
easy control of the angle of incidence θ_i by slightly turning the sample, which is demonstrated by the
schematic drawing on the right. The back-reflection of an alignment laser from the sample is tracked for
all measured angles. The movement of the laser spot can subsequently be used to determine the total
measured angular range.

the sample. The reflection from the sample was then monitored for the entire angular range on a screen outside the chamber. From the movement of the laser beam on the screen and the distance between the sample and the detection screen, the angular range is well-defined and can be precisely determined. The exact analysis of the determination of the angle range for a set of consecutive T-MOKE asymmetry measurements of Ni with different incidence angles is presented in more detail in Chapter A.

4.1.6. Spectrometer design

† Spectroscopy of the reflected EUV light allows for the investigation of the sample magnetization and is realized by a custom-built spectrometer based on a plane grating as the dispersive element and a toroidal mirror as the focusing element. The spectrometer was designed to achieve an energy resolution of about 1 eV to distinguish between the individual harmonics, while also achieving a high efficiency [118].

† The sample reflects both the pump and probe beams towards the spectrometer chamber (see Figure 4.1 (b)). Here, a second aluminum filter is introduced into the beam path to block the reflected pump beam. The EUV beam is focused towards the CCD-camera (GE
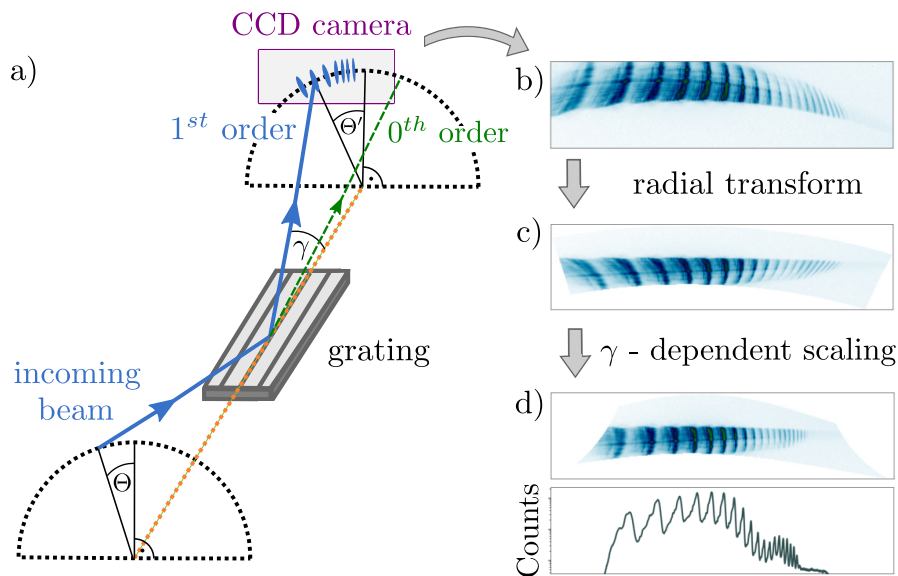
Figure 4.4. – a) Schematic overview of diffraction in the off-plane geometry for the planar grating: The light hits the grating with an azimuthal angle θ, the diffracted high harmonics lie on a cone with half-angle γ, also referred to as the altitude angle. b) Typical 2D high harmonic spectrum recorded with the EUV camera prior to any corrections. c) 2D spectrum after radial transformation onto a (θ', γ)-coordinate system. d) Fully corrected 2D and integrated high harmonic spectrum after a γ-dependent scaling of the diffraction angle. Reprinted from [115] in accordance with *Creative Commons Attribution 4.0* (**CC BY 4.0**) license.

2048 512 BI UV, Greateyes) by a toroidal mirror, which is identical to the toroidal mirror used to focus the EUV probe beam on the sample. As shown in Figure 4.4 (a), the planar reflection grating is positioned in the off-plane geometry, where the grating grooves lie parallel to the plane of incidence of the light. An advantage of this geometry is that it allows for the use of efficient blazed gratings while maintaining the low grazing incidence angle which is necessary for high reflectivities at EUV wavelengths [118]. The grating is gold-coated and has a groove density of 1800 lines/mm. Given the blaze angle δ of 9.3°, optimal diffraction efficiency is achieved at the altitude angle γ of 6.5° for wavelengths near the M-edges of the $3d$ ferromagnets. To prevent camera exposure during the sensor readout procedure, a shutter is positioned between the toroidal mirror and the grating.
[†] A consequence of this spectrometer design is that the EUV wavefront incident on the grating is curved. Equivalently, it can be said that the azimuth angle θ and the altitude angle γ of the beam on the grating have a certain spread. This will lead to a distortion of the measured spectrum (see Figure 4.4 (b)), which is calculated here. The grating equation for this system is [119]

$$m\lambda\sigma = \sin\gamma(\sin\theta - \sin\theta'), \tag{4.1}$$

where m is the diffraction order, λ the wavelength, σ the grating constant and θ' the exit angle. Substituting $\theta \to \theta_0 + \Delta\theta$ and $\gamma \to \gamma_0 + \Delta\gamma$ and performing a Taylor expansion around $\Delta\theta = \Delta\gamma = 0$, we find

$$\theta' = \theta_0' - c_1\Delta\theta + c_2\Delta\gamma + O(\Delta\theta^2 + \Delta\theta\Delta\gamma + \Delta\gamma^2). \tag{4.2}$$

[†] In our experimental geometry, $c_1 \approx 1.1$ and c_2 is typically on the order of 3. Higher order terms can be ignored because they are typically one to two orders of magnitude weaker than the linear terms. From this result, we can conclude the following: 1) the term linear in $\Delta\theta$ will increase the wavefront curvature, leading to an astigmatic focus of the diffracted beam. On the camera, this results in spots which are elongated perpendicular to the spectral direction. 2) the term linear in $\Delta\gamma$ will shift the diffracted beams depending on their altitude angle. Effectively, this leads to a grating dispersion which is stronger for shallower grazing incidence angles on the grating.
[†] In order to correct for this deformation of the measured spectrum, we first transform the cartesian coordinates of the camera onto a (θ', γ)-coordinate system. Next, we apply a γ-dependent scaling of the diffraction angle, eliminating the tilt of the high harmonics. Finally, we integrate the two-dimensional measurement along the spatial dimension

without loss of spectral resolution. An exemplary raw spectrum and the aforementioned procedure are shown in Figure 4.4 (b)-(d).

† In daily operation, the aluminum L_3-edge at 72.7 eV and the known separation of the high harmonics by twice the fundamental frequency are used to calibrate the energy of the recorded high harmonics. In addition, the energy calibration of the spectrum is verified by inserting a 200 nm thick tin filter, which transmits EUV light up to 23.6 eV allowing to identify the 19th harmonic (22.9 eV) of our fundamental driver.

4.2. Benchmarking of EUV spectral analysis

The successful operation of the novel EUV T-MOKE setup was first demonstrated by temperature-dependent and time-resolved measurements of the magnetic asymmetry in Ref. [115]. It was shown that the setup allows for the detailed measurement of element-specific magnetization behavior in complex samples such as the double perovskite La_2NiMnO_6 (LNMO). The capability to conduct time-resolved measurements of the laser-induced demagnetization with only 0.7% RMS noise within 12 hours was underpinned by the measurement of a $Fe_{19}Ni_{81}$ permalloy thin film, which served as a well-known reference sample [21, 101, 120–122]. The excellent capabilities of the setup motivated a more detailed study of the magnetic asymmetry for different energies around the M-edges, i.e., a spectrally-resolved analysis of the transient T-MOKE asymmetry. As prominently demonstrated by the example of OISTR, the spectral analysis of the T-MOKE asymmetry can provide even more information about the magnetic state of the system compared to the evaluation of large energetic regions. Additionally, a number of recent publications on spectrally-resolved behavior in the far-from-equilibrium state raised the question of the competing role of charge and spin dynamics in metallic thin films [29, 30]. On the basis of these publications, the existing setup from Ref. [115] was modified in order to assure sequential measurements of spin dynamics (with p-polarized light) and pure charge dynamics (with s-polarized light).

In the following, the capabilities of our novel EUV T-MOKE setup to measure spectrally-resolved spin and charge dynamics with excellent data quality will be shortly demonstrated for a 21 nm Ni thin film grown on amorphous Si_3N_4. We expect the sample to be covered by a thin non-magnetic NiO layer of ≈ 2 nm. For both polarization measurements, the sample was excited with ≈ 45 fs pulses at a central wavelength of 1030 nm. The absorbed

fluence was determined to $0.8\pm0.2\,\mathrm{mJ/cm^2}$ at $600\,\mathrm{mW}$ incident power. A magnetic field of $100\,\mathrm{mT}$ was applied to switch the magnetization of the sample.

4.2.1. Static magnetic asymmetry

The static magnetic asymmetry together with the high-harmonic spectrum for opposite magnetization directions is shown in Figure 4.5 (a) for energies between $40 - 72\,\mathrm{eV}$. The angle of incidence θ_i for this specific measurement was determined to $44.8 \pm 0.3°$. As will be shown in Chapter 5, the angle of incidence can have a significant impact on the shape and even on the sign of the magnetic asymmetry at certain energies. The magnetic asymmetry peaks at the M_3-resonance around $66\,\mathrm{eV}$ to a magnitude of roughly 30%. The asymmetry is further accompanied by a large off-resonant signal, which spreads down to the lowest measured energy of $40\,\mathrm{eV}$, i.e., down to energies more than $20\,\mathrm{eV}$ below the resonance. The observation of a large off-resonant magneto-optical signal below the M-edge is consistent with results shown in Refs. [123, 124] from T-MOKE and Ref. [125] from XMCD of Ni in the EUV spectral range. For a detailed overview on the origin of the static T-MOKE signal, the reader is referred back to Chapter 3.2.2.

Note that due to the discrete spectrum of odd harmonics of the fundamental frequency with an energy spacing of $2.4\,\mathrm{eV}$, the magnetic asymmetry should only be analyzed on the harmonic energies. In between the harmonics, we find a substructure which is modulated on the magnetic asymmetry. This modulation can be directly attributed to a low signal-to-noise ratio, resulting in a reduced value of the asymmetry parameter.

4.2.2. Time- and energy-resolved spin dynamics

For the time- and energy-dependent spin dynamics, the magnetic asymmetry was evaluated in $0.5\,\mathrm{eV}$ energetic intervals around the individual harmonics, as indicated in Figure 4.5 (a). The corresponding asymmetry time-traces are shown in (b) for the short timescale and in (c) for the long timescale up to $6\,\mathrm{ps}$. With a total measurement time of less than 8 hours for a total number of 102 delay positions, we find an RMS noise level of 1% for the measurement data before time zero t_0.

The magnetic asymmetry time-traces for the individual harmonics reveal a rather homogeneous behavior with a quenching down to about 40% percent of the initial value, except for the harmonic energy below the resonance at $E = 63.8\,\mathrm{eV}$. For this specific energy, the magnetic asymmetry displays an ultrafast increase of $\approx 8\%$ before the demagnetization
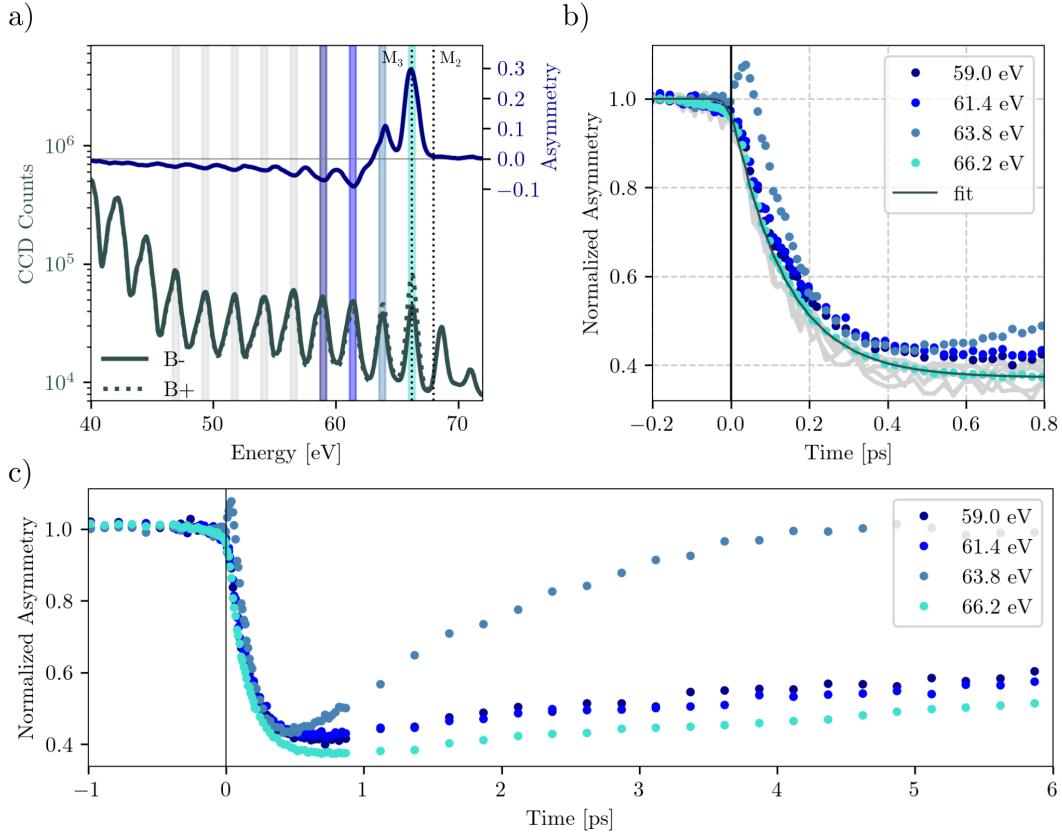
Figure 4.5. – Magnetic asymmetry and time-resolved demagnetization measurement of Ni. (a) Static T-MOKE asymmetry of a 21 nm Ni thin film on amorphous Si_3N_4 at an angle of incidence of 44.8° together with the high-harmonic spectrum for opposite magnetic field directions. The dashed lines signify the M-absorption edges of Ni at M_3=66.2 eV and M_2=68 eV. For the time-resolved analysis, the asymmetry was evaluated in the coloured 0.5 eV energy windows around the individual harmonics. (b) Zoom-in on the short-timescale dynamics for different harmonic energies, revealing homogeneous behavior for all energies except for 63.8 eV, where a surprising initial increase is found. The solid black line displays the double exponential fit for the harmonic energy at the resonance of 66.2 eV. (c) Demagnetization time-traces for harmonic energies close to the resonance.

sets in. While a similar increase has been reported in $Fe_{50}Ni_{50}$ due to OISTR from the sublattice of Ni to the sublattice of Fe [21], the observation of such an increase has not yet been reported for Ni by T-MOKE experiment. However, a similar increase below the resonance of Ni was recently reported by Hennes and coworkers in a combined study of EUV absorption spectroscopy and MCD around the Ni $M_{2,3}$-edge [30]. While the origin of this ultrafast increase could not be conclusively determined, the observation of distinct spin dynamics and red-shifts of the MCD spectrum were attributed to the competition of charge and magnetization dynamics [29, 30].

Table 4.1. – Fit results using Equation 4.3 of the demagnetization time-trace in Figure 4.5 (b) at the Ni resonance of 66.2 eV. For the least-squares fit, measurement data were weighted according to the data spread at each delay individually. The given error margins correspond to the 1-sigma standard deviations of the fit.

Ni, 66.2 eV	
t_0 (fs)	0 ± 1.3
ΔA_m	0.63 ± 0.004
τ_m (fs)	135 ± 3

In addition to the short timescale, the behavior of the transient asymmetry time-trace at 63.8 eV also deviates from all other energies at longer times and exhibits a significantly faster remagnetization to its initial value (see Figure 4.5 (c)). A detailed analysis of the spin dynamics in elemental Ni will follow in Chapter 5, where the distinct dynamics on the sub-100 fs-timescale will be carefully discussed.

As an exemplary analysis of the data, the evolution of the asymmetry time-trace at the resonance (around 66 eV) was fitted with an exponential function convolved with a Gaussian function $G(t)$ with a full width at half maximum of 60 fs, taking into account the pulse duration of the harmonics of about 15 fs. The fit model is given by

$$\frac{A(t)}{A(t < t_0)} = G(t) \circledast \left[1 - \Theta(t - t_0) \cdot \left[\Delta A_m \cdot \left(1 - e^{-\frac{t - t_0}{\tau_m}} \right) \right] \right], \tag{4.3}$$

where τ_m is the demagnetization constant and ΔA_m is proportional to the maximal fractional demagnetization. Θ represents the Heaviside step function and allows the exponential behavior to begin at t_0. The least-square fit results are given in Table 4.1. While the time-dependent magnetization behavior is strongly fluence-dependent, the demagnetization time $\tau_m = 135 \pm 3$ fs is in good agreement with reported combined angle-resolved photoemission spectroscopy (ARPES) and T-MOKE measurements around the Ni resonance [69, 126]. Note that we only fit the short-timescale, as the fitting of the remagnetization is very error-prone due to the relatively short scan range of 6 ps. The actual remagnetization of strongly quenched Ni was previously found to show a slow recovery of tens of picoseconds in a combined study of ARPES and T-MOKE experiment around the M-edge, as reported by TENGDIN et al. and YOU et al. [69, 126].

4.2.3. Time- and energy-resolved charge dynamics

Due to the modification in the mirror chamber described in Chapter 4.1.2, the setup also allows time-resolved reflectivity measurements with *s*-polarized light. On the short timescale, the measurement of the reflectivity with high harmonic energies gives access to charge dynamics (hot electrons). This allows us to track the optically induced excitation pathways in the DOS around E_{F}. On longer times, it provides insights to lattice dynamics. The increase in lattice temperature leads to the expansion of the lattice and induces thermal stress, thus facilitating the generation of strain waves through the sample and the substrate [127, 128]. In particular, for the study of ultrafast spin dynamics in the far-from-equilibrium state, this extension of the setup is a key advantage as it provides further insights into the potential roles of spin and charge dynamics after the optical excitation, which have been extensively discussed in the past [29, 30, 35, 38, 39, 86, 87, 90].
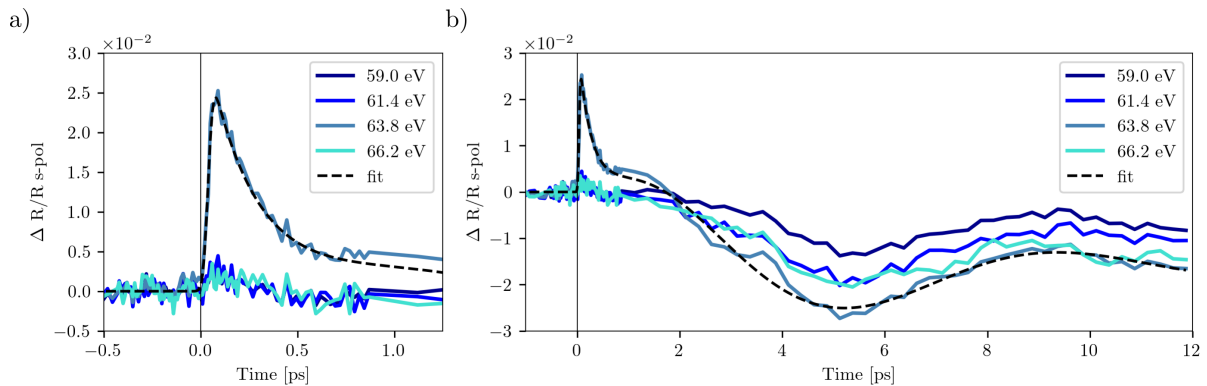
Figure 4.6. – Reflectivity change for different *s*-polarized high-harmonic photon energies from a 21 nm Ni thin film on amorphous Si_3N_4 for the short timescale (a) and for longer times (b). The sample was pumped with an absorbed fluence of $0.8 \pm 0.2\,\mathrm{mJ/cm^2}$. The dashed black line shows the fit for the reflectivity at 63.8 eV (details in the text).

The *s*-polarized reflectivities close to the resonance were analyzed in the same energetic intervals as the T-MOKE measurements presented in the previous section. At an energy of $E = 63.8$ eV, corresponding to roughly 2 eV below the Fermi level, an ultrafast spike of the reflectivity can be determined after $t = 0$ fs as shown in Figure 4.6. This increase of $\approx 2.5\%$ reaches its maximum in less than 100 fs and can be attributed to pump-induced hot electrons. An increase in the reflectivity of this magnitude close to the resonance is consistent with recently published reflectivity data of a Ni thin film by JOHNSEN et al. [124]. The reflectivity for all other evaluated energies close to the resonance is less affected on this ultrafast timescale, indicating that initially electrons are excited from just below E_{F} to unoccupied states above E_{F}. We fit the initial reflectivity

increase and subsequent recovery at 63.8 eV with a combination of an error-function and an exponential decay (dashed line in Figure 4.6 (a)).

On the long timescale, up to 12 ps, the reflectivity of all evaluated energies depicts an exponentially decaying oscillating behavior, shown in Figure 4.6 (b), which corresponds to the generation of acoustic waves in the film. These oscillations on longer times can be fitted with exponentially decaying sinusoids, as demonstrated for the 63.8 eV harmonic energy. A thorough characterization of the reflectivity can provide an extremely accurate characterization of the film thickness, as was shown by variable angle EUV reflectometry measurements, and thereby further extends the potential of our setup [129].

We note that the presented measurement illustrates the capability of our setup to resolve small changes of s-polarized reflectivity on the order of 10^{-2}. The presented data quality is found to be comparable to recently reported reflectivity measurements of a Ni thin film recorded with a similar EUV T-MOKE setup [124]. However, in Ref. [124], a reference spectrometer was needed to achieve this data quality.

In conclusion, the capabilities of the novel EUV T-MOKE setup were demonstrated by spectrally-resolved T-MOKE and s-polarized reflectivity measurements of a Ni thin film. Both datasets demonstrate the ability to perform element-resolved measurements of ultrafast magnetic, electronic, and acoustic excitations with excellent data quality within limited measurement time. For both measurements, a noise level of $< 1\%$ has been determined for the measurement data prior to time zero t_0, which can be directly related to the overall good stability of our fiber-laser-based HHG setup. As will be shown in the next chapters, the ability to measure energy-resolved magnetic and electronic responses allows for a more profound understanding of the microscopic processes underlying the dynamics in magnetic thin films after femtosecond laser excitation.

Analysis of spectrally-resolved spin and charge dynamics in EUV T-MOKE

5

In this chapter, we present spectrally-resolved asymmetry data of Ni for different incidence angles, which, depending on the photon energy, reveal dramatically different dynamics. This observation highlights that the classical analysis of the magnetic asymmetry data from EUV T-MOKE can lead to misinterpretations. On the basis of these surprising experimental results, we developed a new analysis in order to directly extract the off-diagonal dielectric tensor ϵ_{xy} with full femtosecond time resolution. Our reconstruction of the magneto-optical response provides a direct solution to the challenging experimental results and allows a quantitative comparison with theoretical predictions. We can now access both the magnetic and non-magnetic (transient refractive index changes) contributions to the measurement signal and, hence, follow up on recent discussions concerning the respective roles of charge and spin dynamics in the non-equilibrium state induced by femtosecond laser excitation [29, 30, 35, 86, 87, 90]. The power of our analysis is demonstrated by tracing the excitation of minority spins in Ni, where we find excellent agreement with theoretical predictions. Our method and related results were published as an arXiv preprint titled: "Unraveling Femtosecond Spin and Charge Dynamics with EUV T-MOKE Spectroscopy" [130] and is reprinted in this chapter in accordance with *Creative Commons Attribution 4.0* (**CC BY 4.0**) license.

The author of this thesis contributed to the publication as follows: The author performed the measurements mainly together with CHRISTINA MÖLLER and MAREN SCHU-MACHER, carried out the data analysis, took part in the interpretation of the data and contributed significantly to the writing of the manuscript. The fitting procedure to extract ϵ_{xy} and refractive index changes from angle-resolved T-MOKE data is based on ideas from CHRISTINA MÖLLER and was further developed in a joint effort together with the author of this thesis. The final analysis, including the transfer matrix formalism to account for

the multilayer structure of the thin film (capping/magnet/substrate) was implemented with essential assistance of MATTHIJS JANSEN. The TDDFT calculations were provided by SANGEETA SHARMA.

Abstract

The magneto-optical Kerr effect (MOKE) in the extreme ultraviolet (EUV) regime has helped to elucidate some of the key processes that lead to the manipulation of magnetism on ultrafast timescales. However, as we show in this paper, the recently introduced spectrally-resolved analysis of such data can lead to surprising experimental observations, which might cause misinterpretations. Therefore, an extended analysis of the EUV magneto-optics is necessary. Via experimental determination of the dielectric tensor, we find here that the non-equilibrium excitation in an ultrafast magnetization experiment can cause a rotation of the off-diagonal element of the dielectric tensor in the complex plane. In direct consequence, the commonly analyzed magneto-optic asymmetry may show time-dependent behavior that is not directly connected to the magnetic properties of the sample. We showcase such critical observations for the case of ultrafast magnetization dynamics in Ni, and give guidelines for the future analysis of spectrally-resolved magneto-optical data and its comparison with theory.

5.1. Introduction

With the advent and success of laser-based femtosecond element-specific M-edge magneto-optical Kerr spectroscopy in 2009 [131], a very successful series of experiments using this technique has helped to verify and elucidate a number of key findings in ultrafast magnetism [21, 22, 25, 74, 78, 101, 102, 125, 132–135]. As more powerful laser systems have become available over the years, this experimental technique is becoming available in a growing number of laboratories and becoming an important workhorse to study ultrafast magnetization dynamics [115, 120, 124, 136, 137]. However, the introduction of a new experimental capability also requires an ongoing check of the validity of the collected data, and a crosscheck of the results achieved with complementary experimental techniques. Such validation has been done, for example, for the case of photo-induced ultrafast spin currents and the heavily discussed relative delay of the Fe and Ni demagnetization in a Permalloy sample [29, 101, 115, 120–122].

Currently, spectrally-resolved analysis of femtosecond transverse magneto-optical Kerr effect (T-MOKE) data in the extreme-ultraviolet (EUV) is more frequently used, for example for the verification of the so-called optical intersite spin-transfer (OISTR) effect [12, 21, 22, 125, 138]. However, it has already been recognized that the interpretation of such data asks for a more detailed analysis of the collected T-MOKE asymmetry data [28, 37]. Similarly, the comparison of magneto-optical spectroscopy data with state-of-the-art time-dependent density functional theory (TDDFT) and similar theoretical methods requires careful analysis [24, 139].
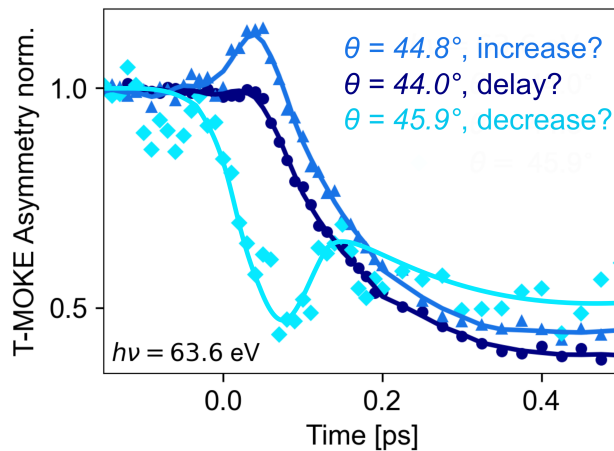
Figure 5.1. – Increase, delay, or decrease of the spin dynamics? Very different dynamics in the T-MOKE asymmetry are observed at 63.6 eV ($\pm 2\%$) photon energy for slightly different angles-of-incidence (dark blue: 44°, blue: 44.8°, light blue: 45.9°). The measurement clearly illustrates that a direct interpretation of T-MOKE asymmetry with ultrafast magnetization dynamics can be highly problematic. Note that the solid lines serve as a guide to the eye.

The urgency for a sophisticated analysis of spectrally-resolved T-MOKE data can be best introduced with an exemplary measurement of ultrafast magnetization dynamics in the prototypical 3d ferromagnet Ni. Figure 5.1 shows transient T-MOKE asymmetry data, measured with our setup [115], and analyzed at 63.6 eV ($\pm 2\%$) EUV photon energy for slightly varying incidence angles. Very disturbingly, the transient dynamics of the T-MOKE asymmetry shows completely distinct behavior. In particular, for the very same ultrafast pump-probe experiment, all heavily discussed experimental signatures, i.e. an increase, a delay, and a decrease in the T-MOKE asymmetry can be identified, which have previously been used to identify the OISTR effect [21, 22, 125], the influence of exchange scattering [101], and the typical demagnetization process [131]. Having just the information of this particular measurement available, all previous interpretations of

T-MOKE data would be in question. In the following, we will show how such critical T-MOKE data needs to be analyzed to obtain reliable access to the true spin dynamics. The overall topic of the paper is illustrated in Figure 5.2. Usually, the main quantity of interest is the global magnetization (top right) or the energy-resolved magnetic moment, given by the difference in majority and minority spins in the density of states (bottom right). In EUV T-MOKE experiments, the aim is to probe the time-dependent magnetization and magnetic moment, however neither magnetization (orange arrow) nor the energy-resolved magnetic moment (red arrow) are directly measured. Rather, as an optical technique, T-MOKE probes the dielectric tensor and is specifically sensitive to the off-axis dielectric tensor element ϵ_{xy} [89]. Since the dielectric tensor (including ϵ_{xy}) can be calculated from TDDFT calculations of the spin-resolved density of states [24, 139–142], a time-resolved extraction of ϵ_{xy} from T-MOKE data would allow for a quantitative comparison of experimental T-MOKE data and theoretical calculations.

In our work, we therefore develop a robust and easy-to-implement method to analyze transient dynamics of the dielectric tensor. With the help of this analysis, we elucidate that the non-equilibrium excitation by the optical pulse can lead to a rotation of the off-diagonal element of the dielectric tensor in the complex plane. This rotational behavior can lead to the observed increase, delay, and decrease of the T-MOKE asymmetry as seen in Figure 5.1, and these differing signals simply depend on the used measurement geometry of the T-MOKE experiment, i.e. the angle of incidence of the EUV light. As TDDFT is also able to provide transient dynamics of the dielectric tensor, we find that a direct comparison of experiment and theory becomes possible via such a dielectric tensor analysis from the data. In Ni, via comparison with theory, we can show that the observed dynamics at early times of the pump excitation (<50 fs) is dominantly driven by spin-conserving transitions in the minority channel. Besides a comparison of the same quantity, our approach also ensures that spectral broadening, multiple edges, and overlapping edges from multiple elements in multi-component materials is properly taken into account.

5.2. Magneto-optical spectroscopy

5.2.1. Magneto-optical asymmetry in T-MOKE

Previous magneto-optical studies have attempted to make a direct connection between the magneto-optical signal and the element-specific magnetization properties of the sample after an ultrafast excitation. However, as shown above and discussed in Figure 5.2, the
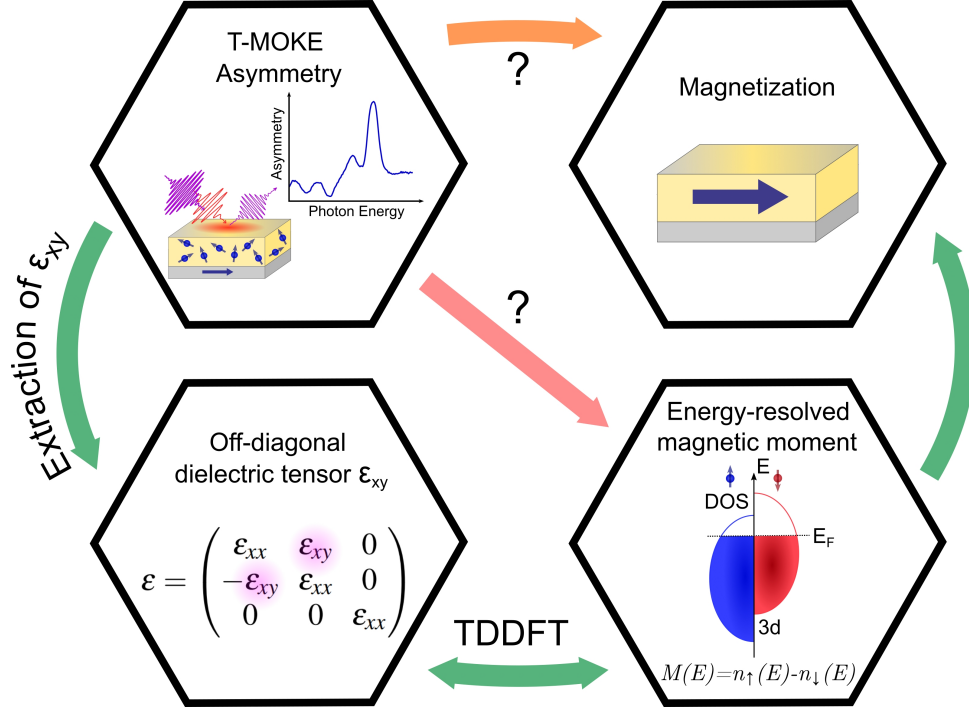
Figure 5.2. – Overview of the connections between experimental magneto-optical signal, the off-diagonal tensor-element and the magnetization.

relation between the measurement signal in a T-MOKE experiment and the magnetization is more complex, even in the equilibrium case. At the microscopic scale, the interaction of light with a material is given by the complex-valued dielectric tensor ϵ, which can be derived by counting the number of allowed optical transitions within the the spin-resolved band structure [20, 91, 139, 143, 144]. For a magnetic material, the imbalance between the different spin channels leads to off-diagonal terms in the dielectric tensor, which couple light fields of orthogonal polarization. For a typical (cubic) magnetic material that is magnetized along the z-axis, the dielectric tensor is commonly expressed as

$$\epsilon = \begin{pmatrix} \epsilon_{xx} & \epsilon_{xy} & 0 \\ -\epsilon_{xy} & \epsilon_{xx} & 0 \\ 0 & 0 & \epsilon_{xx} \end{pmatrix}. \tag{5.1}$$

Here, ϵ_{xx} can be directly related to the non-magnetic refractive index, mostly written as

$$\sqrt{\epsilon_{xx}} = n = 1 - \delta + i\beta, \tag{5.2}$$

while the off-axis dielectric tensor element ϵ_{xy} describes the magneto-optical response of the material.

Through the Fresnel equations, it is possible to express the signal in various magneto-optical techniques in terms of the dielectric tensor components. For example for XMCD, it is known that a signal can be extracted that is proportional to $\text{Re}(\epsilon_{xy})$ [24, 139]. For T-MOKE, the reflectivity of a single vacuum/magnetic material interface can to good accuracy be expressed as [68]

$$R_{\uparrow/\downarrow} = |R_0|^2 + |R_m\epsilon_{xy}|^2 \pm \text{Re}\{2R_0^* R_m \epsilon_{xy}\} \tag{5.3}$$

where $R_0 = \frac{n\cos\theta_i - \cos\theta_t}{n\cos\theta_i + \cos\theta_t}$ and $R_m = \frac{sin2\theta_i}{n^2(n\cos\theta_i + \cos\theta_t)}$ are the (complex-valued) non-magnetic and magnetic contributions to the reflectivity, respectively. $\text{Re}\{...\}$ indicates the real part, and the incidence angle θ_i and refraction angle θ_t are related by Snell's law. The $\pm$ sign in Equation 5.3 is directly linked to the magnetization direction, where switching the magnetization direction also switches the sign.

Based on Equation 5.3, the commonly-used measurement strategy in EUV T-MOKE is to measure the reflected intensity $I_{\uparrow/\downarrow}$ (which is proportional to $R_{\uparrow/\downarrow}$), and subsequently calculate the T-MOKE asymmetry for bulk magnetic material by [28, 37, 139, 145]

$$A = \frac{I_\uparrow - I_\downarrow}{I_\uparrow + I_\downarrow} = \frac{2\text{Re}(R_0^* R_m \epsilon_{xy})}{|R_0|^2 + |R_m\epsilon_{xy}|^2}. \tag{5.4}$$

By alternately measuring $I_\uparrow$ and $I_\downarrow$, this allows to efficiently filter out variations in the light source intensity. Then, it is useful to consider the following assumptions: if $|R_m\epsilon_{xy}|^2 \ll |R_0|^2$ and the refractive index n is constant, then the transient asymmetry $A(t)$ can be normalized to a reference asymmetry A_{ref} (commonly the T-MOKE asymmetry of the sample in equilibrium), and the signal

$$\frac{A(t)}{A_{\text{ref}}} = \frac{\text{Re}(R_0^* R_m \epsilon_{xy}(t))}{\text{Re}(R_0^* R_m \epsilon_{xy}^{\text{ref}})} \tag{5.5}$$

is acquired. Now, a further assumption can be made to finally quantitatively link the observed signal $A(t)$ to a change in ϵ_{xy}: namely that the angle of ϵ_{xy} in the complex plane does not change and only the magnitude $|\epsilon_{xy}|$ decreases/increases. However, as will become clear in the following analysis, the data that is presented in Figure 5.1 unambiguously shows that this set of assumptions cannot hold.

5.2.2. Angle-dependence of the T-MOKE asymmetry

It is well known that the reflectivity of a sample, and more specifically also the T-MOKE signal, depend strongly on the angle of incidence θ_i [71, 101, 102]. This is particularly true for the magneto-optical reflectivity close to the Brewster angle, where a strong magneto-optical signal is observed as the non-magnetic reflection is strongly suppressed. In order to understand this behavior, it is useful to consider $\epsilon_{xy} = \text{Re}(\epsilon_{xy}) + i\,\text{Im}(\epsilon_{xy})$ as a vector in the complex plane: $\vec{\epsilon}_{xy}$. Approximating the T-MOKE asymmetry to depend linearly on ϵ_{xy} (i.e., using $|R_0|^2 \gg |R_m \epsilon_{xy}|^2$ in Equation 5.4), we rewrite Equation 5.4 as

$$
\begin{aligned}
A(\epsilon_{xy}) &\approx \frac{2}{|R_0|^2} \cdot \text{Re}(R_0^* R_m \epsilon_{xy}) \\
&= \frac{2}{|R_0|^2} \cdot [\text{Re}(R_0 R_m^*) \cdot \text{Re}(\epsilon_{xy}) + \text{Im}(R_0 R_m^*) \cdot \text{Im}(\epsilon_{xy})] \\
&= \vec{p}_\theta \cdot \vec{\epsilon}_{xy} = |\vec{p}_\theta||\vec{\epsilon}_{xy}| \cos(\sphericalangle(\vec{p}_\theta, \vec{\epsilon}_{xy})).
\end{aligned}
$$

This analysis shows that it is possible to interpret the T-MOKE asymmetry $A(\vec{\epsilon}_{xy})$ as inner product of $\vec{\epsilon}_{xy}$ with a *probe vector* $\vec{p}_\theta$. For the simple case of a single vacuum/magnet interface, $\vec{p}_\theta$ is (up to a scaling factor) proportional to $(\text{Re}(R_0 R_m^*), \text{Im}(R_0 R_m^*))$. More generally, we define the probe vector as the derivative of the T-MOKE asymmetry with respect to ϵ_{xy}:

$$
\vec{p}_\theta = \left(\frac{\partial A}{\partial(\text{Re}(\epsilon_{xy}))}, \frac{\partial A}{\partial(\text{Im}(\epsilon_{xy}))} \right). \tag{5.6}
$$

We note that since $\vec{p}_\theta$ depends only on the geometric and non-magnetic properties of the sample, it can be calculated without (precise) a-priori knowledge of ϵ_{xy}. It is most important, however, to realize that $\vec{p}_\theta$ rotates strongly in the complex plane as the angle of incidence θ_i of the EUV light in the T-MOKE measurement changes.

This strong θ_i angle of incidence dependence is critical, because the T-MOKE asymmetry is proportional to the inner product of the vectors $\vec{\epsilon}_{xy}$ and the probe vector $\vec{p}_\theta$. If the angle $\sphericalangle(\vec{p}_\theta, \vec{\epsilon}_{xy})$ between these vectors approaches 90°, a particularly strong dependence of the asymmetry on the geometrical factors must be expected. This situation is illustrated in Figure 5.3 (a), where the measured T-MOKE asymmetry for three incidence angles close to $\theta_i = 45°$ is shown. In the spectral region marked with a rectangle, the T-MOKE asymmetry is strongly angle-of-incidence-dependent, and even flips from positive to negative values. This can be understood by looking at the schematic in Figure 5.3 (b), which illustrates the positive to negative change of the inner product of $\vec{p}_\theta$ and $\vec{\epsilon}_{xy}$ as a function of the angle-of-incidence and therewith $\sphericalangle(\vec{p}_\theta, \vec{\epsilon}_{xy})$.
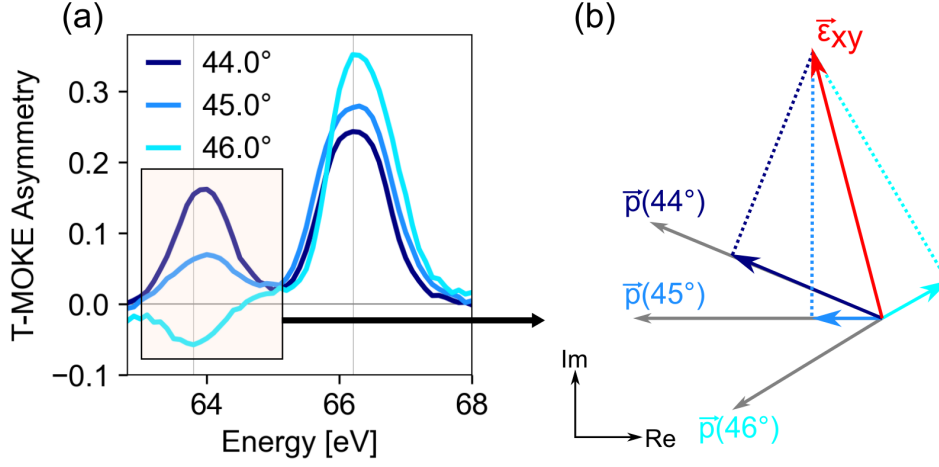
Figure 5.3. – Angle-dependence of the static T-MOKE asymmetry for Ni. (a) The observed T-MOKE
asymmetry for the 21 nm Ni sample for three different incidence angles θ_i close to 45°. (b) Schematic
representation of the probe vectors following Equation 5.6 for the different incidence angles in (a), and
the ϵ_{xy} that was determined from these measurements. For the calculation, we used the same sample
composition and refractive index values as in Section 5.3.1.

Another very important aspect for angles $\sphericalangle(\vec{p}_\theta, \vec{\epsilon}_{xy}) \approx 90°$ is the realization that even
small rotations of ϵ_{xy} in time-resolved measurements would lead to sign-changes in the
measured T-MOKE asymmetry. Indeed, we will show that this is exactly the reason for
the disturbing data presented in Figure 5.1, which was analyzed at a photon energy of
63.6 eV: here, a small transient rotation of ϵ_{xy} leads to very different transient T-MOKE
asymmetries for different angle-of-incidences, as we will fully analyze below.

On the other hand, if $\sphericalangle(\vec{p}_\theta, \vec{\epsilon}_{xy})$ is much larger or smaller than 90°, as is the case in
the spectral region around 66 eV, no such peculiar behavior is expected. An analysis of
transient T-MOKE asymmetry around 66 eV for different angles of incidence consequently
yields perfectly identical results (Figure 5.4), and the transient T-MOKE asymmetry now
reliably reflects the ultrafast magnetic behavior.

In summary, we can already conclude that angles of $\sphericalangle(\vec{p}_\theta, \vec{\epsilon}_{xy}) \approx 90°$ can lead to results in
the time-resolved data that are not straightforward to interpret. However, this particular
situation can readily be identified, if the asymmetry in a certain spectral range is highly
sensitive to the EUV angle-of-incidence and flips sign or approaches zero.

5.2.3. Beyond the bulk approximation

In the previous analysis, we have focused specifically on a single vacuum/magnet inter-
face, as the Fresnel equations for such a case are comparatively simple. However, the
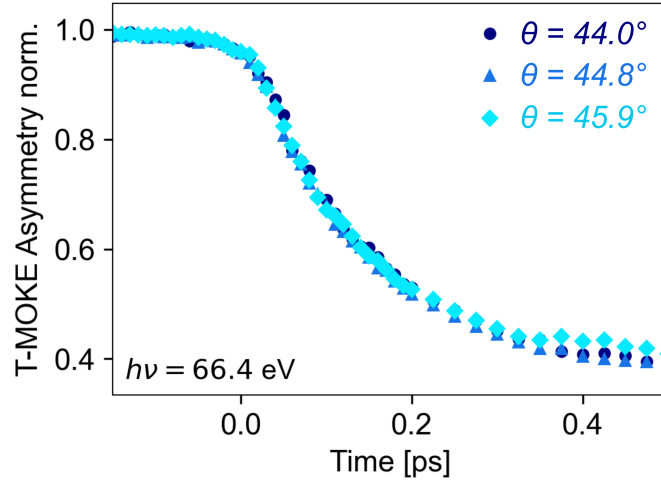
Figure 5.4. – Transient magneto-optical asymmetry at 66.4 eV, i.e., at the Ni resonance, yields identical dynamics for each angle.

magnetic samples studied in ultrafast magnetism, including also this study, are often best described as multilayer structures. In particular, a capping layer is often included to protect the magnetic material from the oxidizing environment; and if no capping layer is included, commonly a native oxide layer forms. For such a sample, expressions for the magnetization-dependent reflectivity can be derived using the transfer matrix formalism [146–148]. In the present study, we have implemented the transfer matrix formalism from Ref. [147] using a symbolic math package (SymPy) [149] for Python to calculate the reflectivity, the T-MOKE asymmetry, and the probe vectors $\vec{p}_\theta$ without relying on assumptions concerning the strength of the magneto-optic response.

5.3. Determination of dielectric tensor from T-MOKE data

The strong angle-dependence of the T-MOKE asymmetry can be leveraged in order to extract the complex-valued off-diagonal dielectric tensor element ϵ_{xy} [68, 71, 150]. Here, we present a unique approach to such magneto-optical reflectometry where only a small range of incidence angles needs to be measured for complete access to ϵ_{xy} at the given photon energies. Specifically, this approach takes advantage of the strong enhancement and dependence on the incidence angle of the T-MOKE asymmetry around 45°, and furthermore makes use of the well-known non-magnetic components of the dielectric tensor, which allows us to reliably calculate the probe vectors. This approach provides two cru-

cial advantages: the experimental setup can be integrated into a typical EUV T-MOKE setup without requiring a major overhaul, and since only a small number of incidence angles needs to be measured, full femtosecond time-resolved magneto-optical spectroscopy is possible with only a small (less than 5-fold) increase in the measurement time.

In the following, we will first discuss the extraction of the static off-diagonal dielectric tensor element, which is necessary in order to calibrate certain experimental parameters, before we continue with the extraction of the time-resolved dielectric tensor.

5.3.1. Extraction of the static off-diagonal dielectric tensor element

Several approaches exist to extract the magneto-optical dielectric tensor element ϵ_{xy} at extreme ultraviolet wavelengths [24, 68, 71, 150, 151]. For thin samples that are best probed in reflection, incidence-angle-dependent or polarization-dependent reflectivity measurements have demonstrated their value [68, 71, 150]. As these techniques rely on reflectivity measurements for linearly polarized light, they are commonly implemented in laboratory-scale experiments based on high-harmonic generation. A limiting factor for the implementation of these techniques, however, is that they typically require a dedicated experimental geometry. Consequently, there is a need for an ϵ_{xy} measurement technique that is compatible with, and can be implemented in, currently existing EUV femtomagnetism experiments. Here, we present the magneto-optical reflectometry method that we implemented in our table-top femtosecond EUV T-MOKE spectroscopy setup [115]. This was made possible by the implementation of a motorized, non-magnetic and UHV-compatible tip-tilt sample holder (SmarAct GmbH), which enabled a scan range of 2.5° (see Figure B.1 in the Supplemental Material (SM) [152]). As such, we anticipate that the method can be rapidly implemented in many setups that are currently being used for fixed-angle EUV T-MOKE.

In order to gain access to the off-axis dielectric tensor element of a magnetized Ni thin film, we performed a series of T-MOKE asymmetry measurements at 11 different incidence angles (shown in Figure 5.5 (a)). The sample consists of a 21 nm Ni film that was deposited by sputtering on a Si_3N_4-coated Si wafer. This thickness was chosen such that femtosecond optical pulses will excite the sample homogeneously, while simultaneously being thick enough that the reflection at the Ni/Si_3N_4 interface does not modify the observed T-MOKE asymmetry strongly. The 100 nm Si_3N_4 layer is thick enough that no reflection from the Si_3N_4/Si interface has to be accounted for. Finally, the Ni layer possesses a thin, native Ni oxide layer on top, which reduces the strength of the T-MOKE
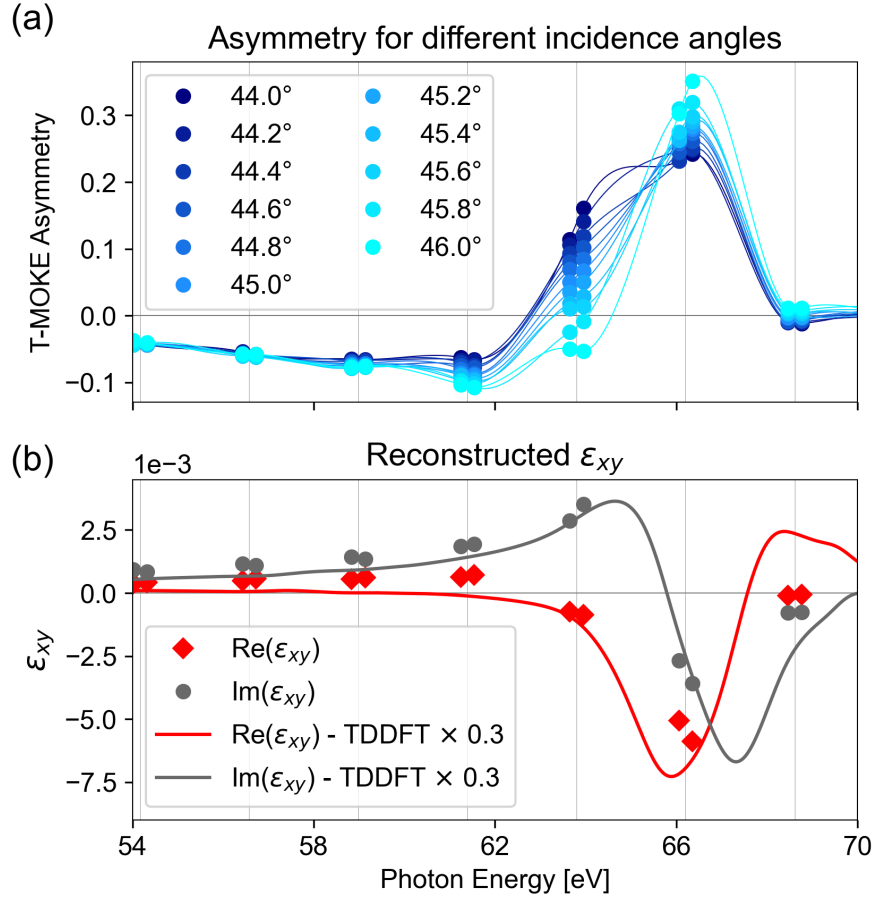
Figure 5.5. – Determination of a static ϵ_{xy}. (a) T-MOKE asymmetry for 11 incidence angles close to 45°. Due to the high resolution of the spectrometer, we were able to evaluate the T-MOKE asymmetry at two energies for each high harmonic, indicated by points. The connecting lines serve as a guide to the eye for the T-MOKE asymmetry. Note that only the relative angles were directly determined from the sample, while the absolute angle was retrieved from the analysis. (b) For comparison, we have calculated the real and imaginary parts of ϵ_{xy} by TDDFT. We find a good agreement with regard to the photon energy dependence, although TDDFT predicts an overall stronger magneto-optical response.

asymmetry. In line with literature [153–155], we set the thickness of the NiO layer to 2 nm. In our analysis, we then use the transfer matrix formalism and calculate expressions for the full three-layer system, including the NiO capping layer, the Ni magnetic layer and the Si_3N_4 bottom layer.

For our sample, the T-MOKE asymmetry depends on the complex-valued refractive indices of Ni, NiO and Si_3N_4, the layer thicknesses, the incidence angle, and the complex-valued ϵ_{xy} of Ni. Using the result of the transfer matrix formalism as the model for the sample, the energy-resolved complex-valued ϵ_{xy} can be determined from a set of angle-dependent T-MOKE asymmetry measurements using a standard least-square fitting pro-

cedure. In order to facilitate a reliable determination of ϵ_{xy} with few measurements over a small angular range, we fix the complex-valued refractive indices to literature values. Here, we retrieve the values for the dispersive (real) part of the refractive index δ from CXRO [103], while we used more recent measurements from Ref. [24] for the absorptive (imaginary) part β. Using other sources for β such as Refs. [151] or [103] leads to small variations in the overall amplitude of ϵ_{xy}, but does not affect the photon-energy dependence significantly.

The best-fit values for the real and imaginary part of the off-diagonal tensor element ϵ_{xy} in Ni are shown in Figure 5.5 (b). As expected, the largest values can be found around the M absorption edges of Ni around 66 eV (M_3-edge). We also find a good qualitative agreement with previously published data [24, 151]. Furthermore, the dielectric tensor can be accurately calculated based on (time-dependent) density functional theory complemented by calculations in the GW framework to achieve an accurate description of the 3p core states [20, 24, 139, 156]. Here, we find a good agreement between experiment and theory on the shape of the dielectric tensor, although theory indicates an overall larger amplitude of ϵ_{xy}. We attribute the discrepancy in the amplitude to a common overestimation of the film-averaged magnetic moment in the TDDFT calculation [28, 157]. In this regard, a better match between experiment and theory, particularly for the spectral region just above the edge, was recently also achieved by manually reducing the exchange splitting [24].

5.3.2. Systematics and uncertainties

There are several experimental uncertainties that may influence the extracted values for ϵ_{xy}. These include statistical and systematical effects. The statistical effects include shot-to-shot intensity fluctuations, position-dependent detection efficiency on the camera and an uncertainty in the relative angle determination. As we performed a large number of angle-dependent measurements with a relatively long measurement time, however, we estimate that the statistical errors are negligible compared to the systematic ones. We have identified several possible sources of systematic errors, which we analyse in the context of the present Ni sample:

First, the leading source of systematic errors is the calibration of the incidence angle. From Figure 5.3, it is clear that a change in the incidence angle leads to a rotation of the probe vectors, as well as a change in the length. Therefore, a systematic error in the angle determination leads to a rotation of $\vec{\epsilon}_{xy}$ in the complex plane, as well as a change

in amplitude. Performing the full ϵ_{xy} reconstruction for different angle calibrations, we find that a 0.5° calibration error in the incidence angle typically leads to a rotation of $\vec{\epsilon}_{xy}$ by 10° and a scaling of the amplitude by 10%. Considering the experimental setup, we estimate that the absolute angle calibration is accurate to within 0.3°.

Second, quantitative determination of the T-MOKE asymmetry relies on an accurate subtraction of the background signal in the spectrometer. This is particularly critical when the detected EUV flux is low. To avoid errors due to this effect, we have chosen to evaluate the data only at photon energies around the peaks of the high-harmonic generation (HHG) spectrum. Nevertheless, we note that close to the HHG cut-off energy (≈ 70 eV, cf. Figure B.2 in SM), the flux of each harmonic significantly decreases. At these photon energies, an imperfect background correction can lead to a reduction of the observed T-MOKE asymmetry and thereby an underestimation of the amplitude of ϵ_{xy}. For the data reported in this paper, we estimate this effect to be negligible.

Third, it was already discussed that the NiO capping influences the observed T-MOKE asymmetry. Unfortunately, no direct determination of the capping layer thickness was possible. Therefore, we have analysed the influence of the capping layer thickness on the retrieved ϵ_{xy} values. Within the range of expected NiO thicknesses (1.5 to 2.5 nm), we find that a thicker (thinner) NiO capping would reduce (increase) the size of the observed T-MOKE asymmetry and therefore would lead to a slightly larger (smaller) amplitude of ϵ_{xy}. Here, 0.5 nm change corresponds to less than 10% change in the amplitude. Also, a comparatively small rotation of the extracted ϵ_{xy} can be observed. Overall, the effect due to uncertainty in the capping layer thickness is less pronounced than the effect due to the angle of incidence calibration.

Fourth, we note that the presented ϵ_{xy} reconstruction technique depends on accurate values for the non-magnetic refractive indices of all materials in the sample. However, by performing the full analysis for different values of the refractive index of Ni (from Refs. [24, 103, 151]), we find only a minor effect on the shape and strength of ϵ_{xy}. Related to that, also an accurate calibration of the photon energy is necessary. Within the experimental uncertainty of the photon energy calibration, which is $< 2\%$, we find no significant change in the reconstructed ϵ_{xy}.

5.3.3. Probing the transient dielectric tensor

Next, we proceed to determine the time-resolved ϵ_{xy} during optically-induced ultrafast demagnetization with sufficient time resolution to trace the full demagnetization process

and thereby provide an ideal basis for comparison with theoretical methods that describe
the dynamics of the electron, spin and lattice degrees of freedom. Compared to the static
case that was previously discussed, we make two observations: First, as a consequence
of the optical excitation, it is not possible to fix the refractive index to literature values;
rather, the dynamical behavior of β and δ (see Equation 5.2) must be extracted from
the experimental data. Second, the number of measured angles must be limited as much
as possible to facilitate the measurement of a larger number of pump-probe delays. We
find that these points can be addressed by choosing the reflectivity $R_{\uparrow/\downarrow}$ (Equation 5.3;
more precisely its equivalent from the transfer matrix formalism) as a starting point for
the time-resolved analysis, rather than the T-MOKE asymmetry (Equation 5.4). Instead
of a single value per photon energy and pump-probe delay, this yields two measurement
values (for two magnetization directions) which contain both magnetic and non-magnetic
contributions.
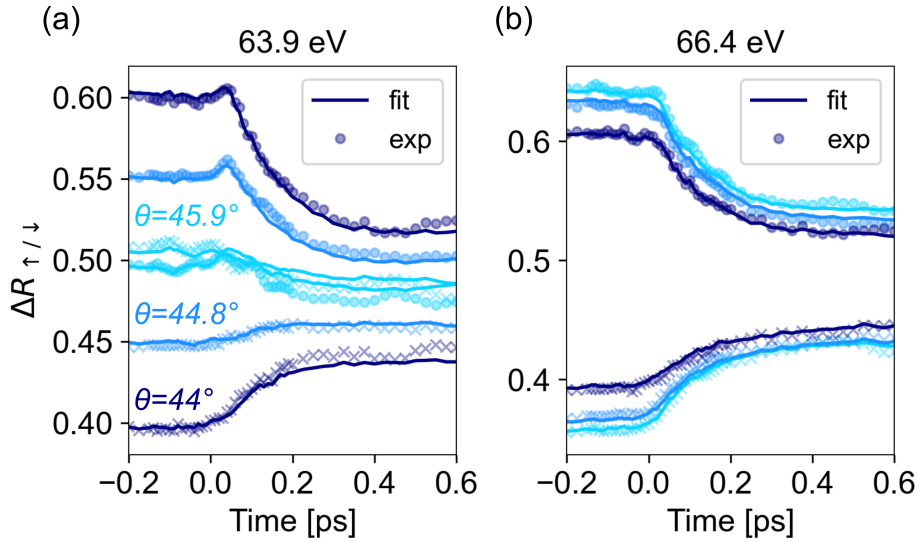
Figure 5.6. – Fitting of the time-resolved data to extract both ϵ_{xy} and β. (a, b) The measured (points)
and reconstructed (line) transient relative reflectivity $\Delta R_{\uparrow/\downarrow}(t)$ for opposite magnetization directions (cf.
Equation 5.7) during optically-induced magnetization dynamics for photon energies just below (a) and
close to (b) the Ni M-edge.

As the absolute reflectivity cannot be measured in our experiment, we consider only the
relative changes compared to the unpumped ($t < 0$) case. From a measurement series of
the delay-dependent intensity $I_{\uparrow/\downarrow}(t)$, we extract the relative reflectivity

$$\Delta R_{\uparrow/\downarrow}(t) = \frac{1}{2}\frac{R_{\uparrow/\downarrow}(t)}{R_{\uparrow/\downarrow}(t_{\mathrm{ref}})} = \frac{I_{\uparrow/\downarrow}(t)}{I_{\uparrow}(t_{\mathrm{ref}}) + I_{\downarrow}(t_{\mathrm{ref}})}, \tag{5.7}$$

where t_{ref} indicates the reference time interval where the probe arrives at the sample before the pump pulse. This yields a signal that reflects the static asymmetry at times before the pump pulse and provides a measure of the transient magneto-optical and non-magnetic reflectivity changes at times after the pump pulse has arrived. Figure 5.6 (a) and (b) show such measurement data for the same experimental situation that was presented in Figure 5.1, namely the optically-induced demagnetization of Ni.

The full data set contains the magnetization-dependent relative reflectivity for the full high-harmonic spectrum at 3 incidence angles θ_i (44°, 44.8° and 45.9°, as determined from the static analysis). In order to extract the time-dependent ϵ_{xy}, we apply a similar fitting procedure as was used in the static case: Each photon energy and each pump-probe delay are considered independently. For each combination of these, our reconstruction algorithm determines the optimal values for $\text{Re}(\epsilon_{xy})$, $\text{Im}(\epsilon_{xy})$, β and δ.

We find that δ generally does not influence the predicted reflectivity strongly, and consequently it cannot accurately be determined with a least-square fitting routine. To address this, we employ a self-consistent two-step approach: 1. keeping δ fixed, we use a least-square fitting to determine $\text{Re}(\epsilon_{xy})$, $\text{Im}(\epsilon_{xy})$ and β. 2. We use a Kramers-Kronig (KK) transform to determine δ [158]. Repeating steps 1 and 2 up to ten times has shown excellent convergence and a good reconstruction of the measured values, as shown in Figure 5.6 (a) and (b). We note that although $\text{Re}(\epsilon_{xy})$ and $\text{Im}(\epsilon_{xy})$ are also connected by the KK relations, the implementation of such a transform is challenging due to the sparsely sampled nature of our spectrum. We have therefore achieved better results without linking $\text{Re}(\epsilon_{xy})$ and $\text{Im}(\epsilon_{xy})$ by KK.

5.4. Interpretation

5.4.1. Rotation of ϵ_{xy}

Having reconstructed the transient dielectric tensor including both the magnetic (ϵ_{xy}) and non-magnetic (ϵ_{xx}) part, we proceed with the interpretation of these results. In a first step, it is instructive to return to the special case that was identified in Ni at 64 eV photon energy (Figure 5.1). Figure 5.7 (a) and (b) show the real and imaginary part of the off-diagonal dielectric tensor element, respectively, as a function of time for two selected energies (more data, including the extracted variation of δ, are shown in Figure B.5 in the SM [152]). First, we recognize that the overall magnitude $|\epsilon_{xy}|$ decreases over time to approximately 40% of its original length after 600 fs. More interesting, however, we also
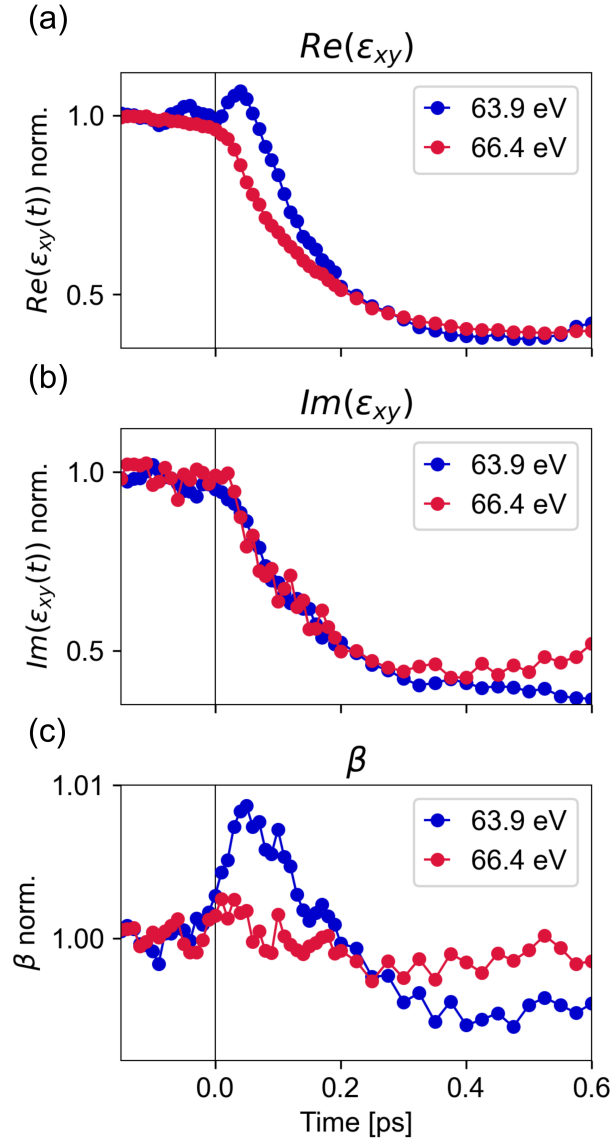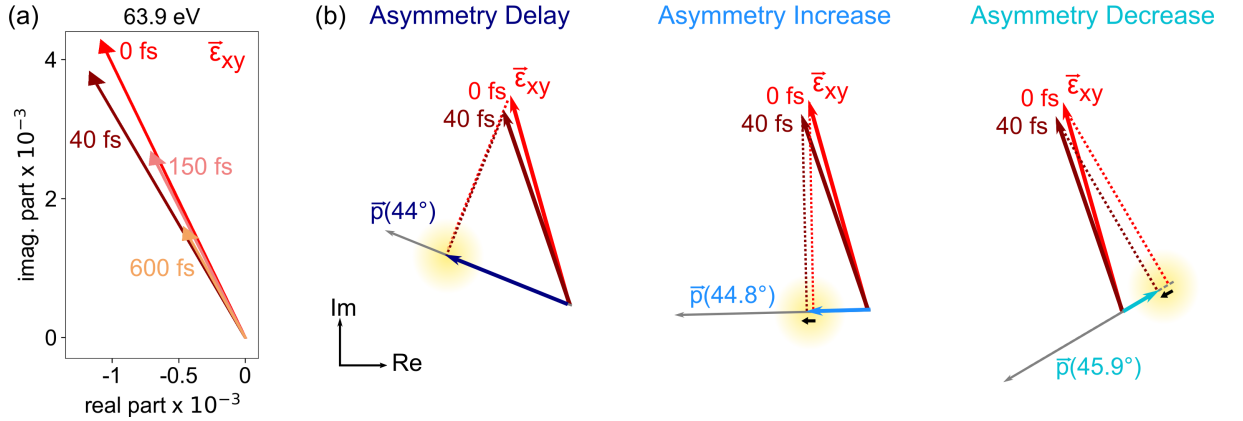
Figure 5.7. – (a, b) Transient evolution of ϵ_{xy} after the optical excitation. ϵ_{xy} rotates in the complex plane, because the real and imaginary part do not change identically. The rotation of ϵ_{xy} is of particular importance to understand the differences in the asymmetry time-traces for different incidence angles below the resonance. (c) Transient changes of the imaginary part of the refractive index (β) of Ni retrieved from the angle-resolved EUV T-MOKE data. We find a strong change of β at $h\nu = 63.9$ eV that is indicative for the strong excitation of electrons.

see that $\mathrm{Re}(\epsilon_{xy})$ and $\mathrm{Im}(\epsilon_{xy})$ do not quench identically as a function of time, especially for $h\nu = 64$ eV, where a transient increase of $\mathrm{Re}(\epsilon_{xy})$ is observed. This means that ϵ_{xy} must transiently rotate in the complex plane. This rotation in the complex plane is visualized in Figure 5.8 (a) and is a key factor in the explanation of the diverse transient effects that

Figure 5.8. – (a) Transient evolution of $\vec{\epsilon}_{xy}$ for selected times after the optical excitation. $\vec{\epsilon}_{xy}$ rotates in the complex plane, as the real and imaginary part do not change identically. (b) A rotation of $\vec{\epsilon}_{xy}$ in the complex plane can lead to an increase, a decrease, or no effect on the magnetic asymmetry, which can be understood from the alignment of $\vec{\epsilon}_{xy}$ and $\vec{p}_\theta$. Here, we specifically consider the change in $\vec{\epsilon}_{xy}$ of Ni at 64 eV and 40 fs after the onset of demagnetization. At 44°, the rotation of $\vec{\epsilon}_{xy}$ is such that the projection on $\vec{p}_\theta$ does not change. Hence, no change in the magnetic asymmetry is observed. At 44.8°, the rotation leads to an increase of the projection (magnetic asymmetry), while at 45.9°, a pronounced decrease is observed. The change of the projection from $\vec{\epsilon}_{xy}$ on $\vec{p}_\theta$ between unpumped and at 40 fs is highlighted in yellow.

were observed in Ni at 64 eV (Figure 5.1). However, we note that a rotation of ϵ_{xy} can also be observed for many other photon energies, and does not necessarily have a large impact on the T-MOKE asymmetry data, as is evident from the measurement shown in Figure 5.4. Therefore, a rotation of ϵ_{xy} alone is not sufficient to explain the peculiar data of Figure 5.1.

At 64 eV, we find that, in addition to the transient rotation of ϵ_{xy}, the probe vector $\vec{p}_\theta$ and the off-diagonal dielectric tensor element ϵ_{xy} are close to orthogonal. This is evident by the zero-crossing of the static magnetic asymmetry for different angles-of-incidence (see Figure 5.3 and 5.5). This situation does not occur at the other photon energies that we have observed, and it provides the second key to the explanation of the data in Figure 5.1. The T-MOKE asymmetry can be approximated by the projection of ϵ_{xy} on the probe vectors $\vec{p}_\theta$. In Figure 5.8 (b), we now apply this method again to visualize how the experimentally-determined transient rotation of ϵ_{xy} can influence the measured T-MOKE asymmetry. We find that changes of the orientation of ϵ_{xy} can lead to dramatic effects, which furthermore depend strongly on the precise angle $\sphericalangle(\vec{p}, \vec{\epsilon}_{xy})$, and in particular if this angle is more or less than 90°. We can readily construct scenarios that predict a delay, a rapid increase and a rapid decrease in the T-MOKE asymmetry - exactly as was observed for Ni (cf. yellow areas in Figure 5.8 (b)). Furthermore, we note that a complete reversal of the T-MOKE asymmetry might also occur. A naive interpretation of the T-MOKE

asymmetry might confuse this observation for a reversal of the magnetic moment, which we emphasize is not the case here. Thus, we conclude that in experiment, where the transient change of the T-MOKE asymmetry is always normalized to its value before the pump excitation, even very small angle changes of ϵ_{xy} can have a huge impact on the qualitative trend of the transient T-MOKE asymmetry data.

Since the T-MOKE asymmetry depends on the relative angle $\sphericalangle(\vec{p}, \vec{\epsilon}_{xy})$, it is clear that not just a rotation of ϵ_{xy}, but also a rotation of $\vec{p}_\theta$ might lead to unexpected dynamics in the time-resolved T-MOKE asymmetry signal. Since such rotations can arise due to changes of the refractive index, they are commonly referred to as non-magnetic artifacts in the ultrafast magnetism community [37, 159]. However, we note that in our time-resolved analysis, β (Figure 5.7 (c)) and δ (Figure B.5 in SM) are reconstructed in addition. Therefore, this analysis allows to separate the rotation of ϵ_{xy} from any rotation in $\vec{p}_\theta$. Equivalently, this analysis separates the magnetic and non-magnetic effects. For Ni at 64 eV, we find that the $\vec{p}_\theta$ vectors change insignificantly in comparison to ϵ_{xy}, indicating that the angle-dependent T-MOKE asymmetry changes are dominated by the rotation of ϵ_{xy}.

In summary, we find that the optically-induced non-equilibrium excitation in Ni leads to a transient rotation of the off-diagonal element of the dielectric tensor. In consequence, we show that the T-MOKE asymmetry may exhibit increased, decreased, and delayed behavior, which must not be directly interpreted as transient dynamics of the magnetization of the sample.

5.4.2. Comparison to theory

Before we carry out a direct comparison to theory, it is instructive to have a qualitative look at the resonant M-edge transitions that are probed in experiment with EUV T-MOKE spectroscopy. Figure 5.9 (a) shows a schematic of the spin-split 3d and 4s density of states of Ni and the spin-split Ni 3p core levels, for which we include the approximate intrinsic linewidth broadening. As can be seen from this schematic, the spin-split 3p core levels overlap and cover an energy range of ≈ 5 eV, which is comparable to the energy range of the full valence and conduction band structure of Ni. Therefore, a specific EUV energy (pink arrow in Figure 5.9 (a)) does not only probe a specific energy within the spin-split DOS, but an extended region of several electronvolts. In consequence, the collected T-MOKE asymmetry is strongly broadened, and it is not straightforward to identify spectrally-resolved dynamics in the T-MOKE asymmetry or even the extracted dielectric
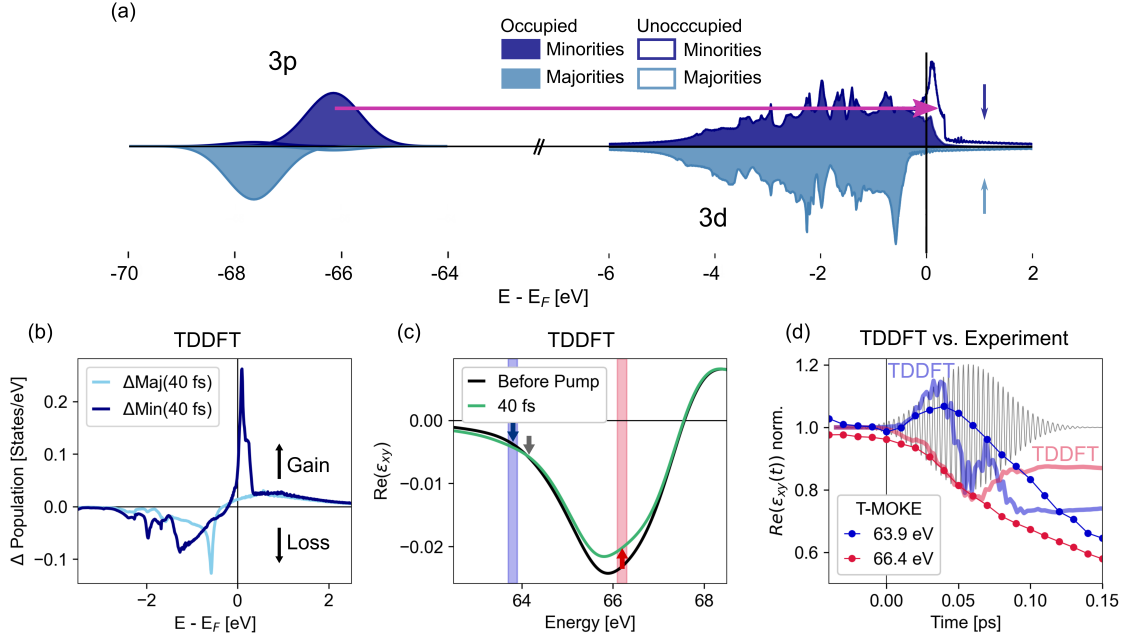
Figure 5.9. – Femtosecond spin dynamics from TDDFT, compared to experiment. (a) Spin-resolved density of states from density functional theory and the equilibrium occupation at 300 K for the 3p, 3d and 4s states in Ni. Due to the exchange splitting, significantly more minority states (upper part) are unoccupied (unshaded region around E_F), thereby allowing for more optical transitions (purple arrow). (b) As seen in the population change at 40 fs, the optical excitation with 1.2 eV photons leads to a strong redistribution of the population in the minority channel (dark blue), populating empty states at 0-0.5 eV above E_F and creating empty states below E_F. In comparison, the majority channel (light blue) is less affected. (c) The redistribution of spins and charge carriers leads to a modification of the magneto-optical response (ϵ_{xy}). Depending on the position with respect to the M-edge photon energy E_M, the spectral dynamics of $\text{Re}(\epsilon_{xy})$ show regions with a strong relative decrease of $\text{Re}(\epsilon_{xy})$ (indicated with a red arrow) but also regions with a relative increase of $\text{Re}(\epsilon_{xy})$ (blue arrow) or a delayed onset of dynamics (grey arrow). (d) The calculations can be directly compared to experiment by evaluating $\text{Re}(\epsilon_{xy})$ as a function of time. Here, we observe that the predicted relative increase in $\text{Re}(\epsilon_{xy})$ is confirmed from experiment (see Figure 5.6 (a)). The time axis of experiment and theory were shifted according to each, as visualized by the electric field of the pulse used for the theory calculations.

tensor with occupation changes or band renormalizations in the electronic structure of the investigated material.

However, if we look at our TDDFT calculations in Figure 5.9 (b), such a comparison seems necessary at first. For 1.2 eV and 47 fs pump pulses, we find that the time-resolved change in minority and majority occupation of the DOS exhibits spectrally very distinct dynamics. For example, because of the large unoccupied DOS in the minority channel of Ni just above the Fermi-level (cf. Figure 5.9 (a)), Figure 5.9 (b) shows that pumping with 1.2 eV leads to a peaked increase of minority spins in a ≈ 300 meV spectral region above the Fermi level. In other words, we see a strong minority inter-energy transfer of spins from below to above the Fermi-level. In the majority channel, we also pump electrons from

below to above the Fermi-level, but much less efficient, because there are much less empty
states available for the transition. In total, this means that the optical excitation leads
to a magnetic moment increase below the Fermi-level (loss of minority electrons), and an
overall magnetic moment decrease (gain of minority electrons) just above the Fermi-level.
However, all of these distinct spectral signatures will be broadened in experiment due to
the large linewidth of the Ni 3p core levels.

We can overcome this problem by directly calculating the transient changes in the dielec-
tric tensor, which takes all EUV transitions into account and moreover is a quantity that
we now can directly compare with experiment. Specifically, we focus on the real part of
ϵ_{xy}, which can be related to the spin polarization of the unoccupied states. Figure 5.9 (c)
shows the theoretical transient dynamics of $\text{Re}(\epsilon_{xy})$ in the corresponding energy range.
First, we recognize that the spectrally distinct dynamics as seen in the transient occu-
pation changes in Figure 5.9 (b) are completely smeared out. Nevertheless, we still find
broad energetic regions where the inter-energy spin transfer as seen in Figure 5.9 (c) can
be verified: Below the energy marked with the grey arrow in Figure 5.9 (c), $\text{Re}(\epsilon_{xy})$ shows
an ultrafast relative increase, and an ultrafast decrease for energies above. If $\text{Re}(\epsilon_{xy})$
would be extracted exactly at the energy of the green arrow, we would expect a delayed
behavior in the dynamics.

Having this theoretical result on transient dynamics of $\text{Re}(\epsilon_{xy})$, we now carry out a direct
comparison with experiment, where we were able to extract $\text{Re}(\epsilon_{xy})$ at the energies marked
with blue- and red-shaded areas in Figure 5.9 (c). Figure 5.9 (d) shows this comparison of
time-resolved dynamics of $\text{Re}(\epsilon_{xy})$ for theory (solid lines) and experiment (data points).
Clearly, the predicted relative increase and decrease in $\text{Re}(\epsilon_{xy})$ after optical pumping can
be confirmed. We also find that for longer time-delays >100 fs, the experimental data
shows a further reduction of $\text{Re}(\epsilon_{xy})$, while the theory data stays constant. This is to
be expected, because TDDFT does not take all possible spin-flip scattering processes
into account, which in experiment lead to the overall demagnetization of the sample on
timescales larger than 100 fs.

In summary, TDDFT predicts an OISTR-like process, i.e., an optically-driven inter-energy
spin transfer similar to the intersite spin transfer in the usual OISTR process. This
pumping of spins happens predominantly in the minority channel and leads to distinct
spectrally-dependent magnetization increase and decrease below and above the Fermi-
level, respectively. Via a direct calculation of the real part of the off-diagonal element
of the dielectric tensor, $\text{Re}(\epsilon_{xy})$, we are able to pinpoint the inter-energy transfer in the
transient dynamics of $\text{Re}(\epsilon_{xy})$. As $\text{Re}(\epsilon_{xy})$ can be directly extracted from our experimental

data, we are able to unambiguously verify the optically-driven inter-energy spin-transfer process in Ni.

5.5. Conclusion

In conclusion, we have discussed an intriguing effect in EUV T-MOKE magnetism studies, where different transient dynamics were observed under almost identical experimental conditions. This observation conclusively illustrates that it is not always possible to directly compare time-resolved T-MOKE data with time-resolved calculations of the spin-resolved density of states. Here, we show that a quantitative comparison with TDDFT can be achieved by extracting the transient dynamics of the off-axis dielectric tensor element ϵ_{xy}.

We have presented a robust technique to retrieve ϵ_{xy} from experimental T-MOKE data with full femtosecond time resolution at little experimental cost. The data that we have achieved solves the controversy that slightly different incidence angles lead to dramatically different dynamics in the T-MOKE asymmetry. Even more, our technique allows to directly reconstruct the magnetic and non-magnetic parts of the refractive index. Studying the prototypical case of femtosecond demagnetization in Ni, we show that this data is ideal for a quantitative analysis and comparison with TDDFT calculations and allows to trace the optically-induced spin and charge dynamics in exceptional detail. We want to emphasize that besides a comparison of the same quantity, i.e. ϵ_{xy}, this approach also ensures that spectral broadening, multiple edges, and overlapping edges from multiple elements in multi-component materials is properly taken into account.

Beyond this exemplary case, we expect that femtosecond ϵ_{xy} spectroscopy will be especially valuable to shed light on the recently discovered OISTR effect and similar femtosecond optically-induced spin dynamics. In Ref. [26], we perform such a study, and discuss the implications for OISTR, which was, after all, first experimentally evidenced by EUV T-MOKE.

Acknowledgements

5.6. Charge excitation and refractive index changes

From our newly developed analysis, we were able to retrieve ϵ_{xy} from experimental T-MOKE data of Ni with full femtosecond time resolution. In addition to that, we were also able to reconstruct the non-magnetic parts of the refractive index $n = 1 - \delta + i\beta = \sqrt{\epsilon_{xx}}$, where we found an increase of the absorptive part β around $64\,\text{eV}$ (cf. Figure 5.7). Hence, we find that the spin transfer process is accompanied by a strong redistribution of charges from below the Fermi level to energies above E_{F}, resulting in an increase of the EUV absorption at the given energy, as expected. Note that comparable changes in the absorption at EUV energies close to the resonance of Ni have previously been reported in Refs. [29, 30, 124].

It is worth noting that the changes in the absorption influence the magneto-optical signal, leading to an asymmetric behavior of the reflected intensities $I_{\uparrow/\downarrow}(t)$. This anti-mirror symmetry becomes apparent when comparing the transient relative reflectivity $\Delta R_{\uparrow/\downarrow}(t)$ at $63.9\,\text{eV}$ at early timescales with the symmetric changes of the reflectivity at $66.4\,\text{eV}$, as shown in Figure 5.6 (a) and (b), respectively. Such a signature in the magneto-optical signal due to a strong charge response after optical pumping has already been pointed out by PETER OPPENEER for XMCD technique [160]. In consequence, we observe a mixed signal of magnetic and charge contributions, which we are only able to reproduce in our analysis if we include changes of refractive index (see Figure B.4 in Chapter B for the analysis excluding changes of refractive index).

In order to further crosscheck the validity of our results of the optical changes from the fitting procedure, we measured the transient reflectivity with s-polarized EUV light, which is independent of the magnetization (cf. Equation 3.5 in Chapter 3). However, it provides access to the excited electron dynamics, i.e., it reflects the transient variation of the refractive index [37]. Based on the reconstructed values of the refractive index changes from the p-polarized T-MOKE data, we can now calculate the corresponding transient s-polarized reflectivity. As illustrated in Figure 5.10, we find good qualitative agreement between the reconstructed and the measured reflectivity on the short timescale ($t < 300\,\text{fs}$), where refractive index changes are the most important due to the far-from-equilibrium electron distribution. The reconstructed values of the optical changes allow reproducing the increase observed in the experiment at $63.9\,\text{eV}$, but the overall magnitude of the increase is underestimated. We attribute this to the following possible reasons:

- We do not directly fit the transient changes in refractive index of the NiO capping layer. Instead, the same change as for the Ni layer is assumed.

- Our analysis does not account for depth-dependent effects, which have been shown to have a spectral dependence on the T-MOKE observable [102].

- Pump-induced dynamics in the Si_3N_4 are neglected, as they are assumed to play a minor role.
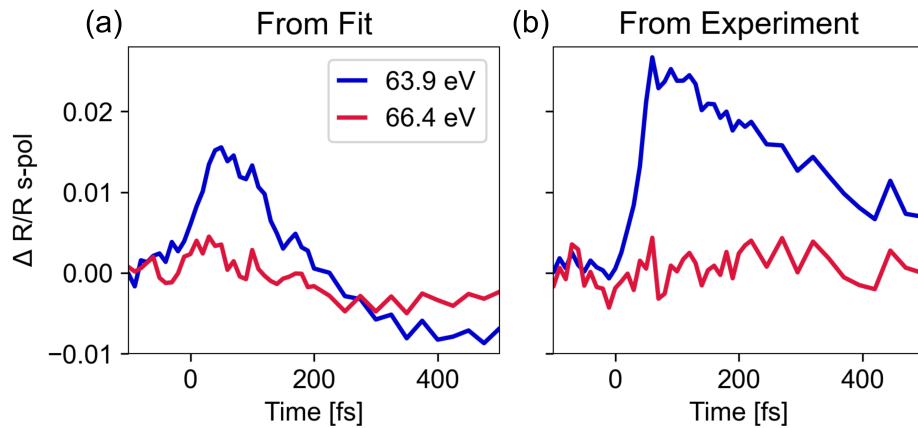
Figure 5.10. – Comparison of the reflectivity change for *s*-polarized high harmonic photon energies close to the Ni resonance, reconstructed from the fit of the T-MOKE data (*p*-polarized) in (a) and the measured *s*-polarized reflectivity in (b). Qualitatively, we find the same behavior for both energies in the reconstructed and the measured data.

5.7. Does OISTR in FeNi exist?

A key signature used to identify OISTR in $Fe_{50}Ni_{50}$ was the observation of an increase of the T-MOKE asymmetry below the Ni resonance [21]. However, as we showed in this chapter, a similar increase of the magnetic asymmetry can be found for pure Ni, where naturally a spin transfer to another subsystem is not possible. Further, we found that depending on the experimental geometry, drastically different dynamics of the magnetic asymmetry can appear. Therefore, it is necessary to ask what implications these findings have on the OISTR in FeNi compounds.

For this purpose, we revisited the laser-induced dynamics that were previously used to verify the OISTR process and applied our analysis for a full time-resolved reconstruction of the dielectric tensor to angle-resolved transient magnetic asymmetry data of $Fe_{50}Ni_{50}$
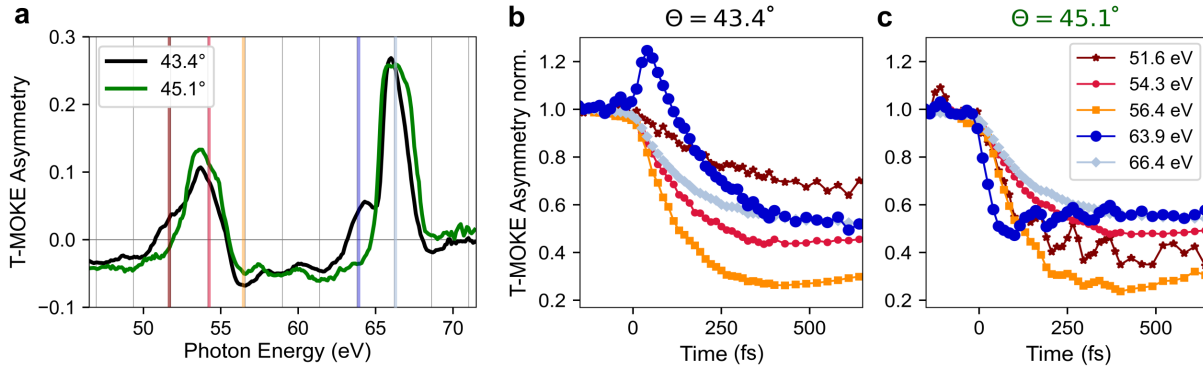
Figure 5.11. – Apparently contradictory EUV T-MOKE measurements of OISTR in $Fe_{19}Ni_{81}$, recorded at different EUV incidence angles and otherwise identical conditions. (a) Static T-MOKE asymmetry for two incidence angles, where the magnetic asymmetry changes sign around 52 eV and 64 eV for the two different incidence angles. (b, c) Time-resolved magnetic asymmetry traces for 43.4° and 45.1° incidence angle, respectively. The analyzed photon energies around the M-absorption edges of Fe and Ni are marked as colored bars in (a). At 43.4°, the typical transient increase at 63.9 eV that was previously associated with OISTR is seen [21], while no such increase is visible at 45.1°. Reprinted from [26] in accordance with *Creative Commons Attribution 4.0* (**CC BY 4.0**) license.

and $Fe_{19}Ni_{81}$. The results have been published as an arXiv preprint titled "Verification of ultrafast spin transfer effects in FeNi alloys" [26]. Parts of this section are replicated from this publication in accordance with *Creative Commons Attribution 4.0* (**CC BY 4.0**) license. The author of this thesis contributed to the publications as follows: The author performed the measurements together with Christina Möller, Maren Schumacher and Mariana Brede, took part in the discussion and interpretation of the data and contributed to the writing of the manuscript. The data evaluation was performed by Christina Möller.

As already seen in the Ni data, we find the magnetic asymmetry in both FeNi compounds to show the same intriguing feature of apparently contradictory dynamics below the Ni resonance depending on the angle of incidence θ (exemplarily shown for $Fe_{19}Ni_{81}$ in Figure 5.11). This highlights the importance of a crosscheck of the validity of the OISTR process in these materials.

Figure 5.12 (a) shows the extracted transient evolution of $Re(\epsilon_{xy})$ for the spectral region where the OISTR-induced increase was expected and verified in the case of $Fe_{50}Ni_{50}$ (dashed line) together with the results of $Fe_{19}Ni_{81}$ (dotted line) and pure Ni (solid line). For all samples, we find an increase of $Re(\epsilon_{xy})$ which is indicative of the loss of minority spins in Ni due to optical pumping. The extraction of $Re(\epsilon_{xy})$ allows for direct comparison to theory calculations (see Figure 5.12 (b)), where we find good qualitative

agreement. From the magnitude and duration of the increases, we also find differences in the efficiency of the spin transfer in the materials. It follows that the OISTR-relevant transition is most efficiently excited in the $Fe_{50}Ni_{50}$, less efficiently in $Fe_{19}Ni_{81}$, and even less in Ni (find details on the measurements of all samples and the TDDFT calculations in Chapter B.2).
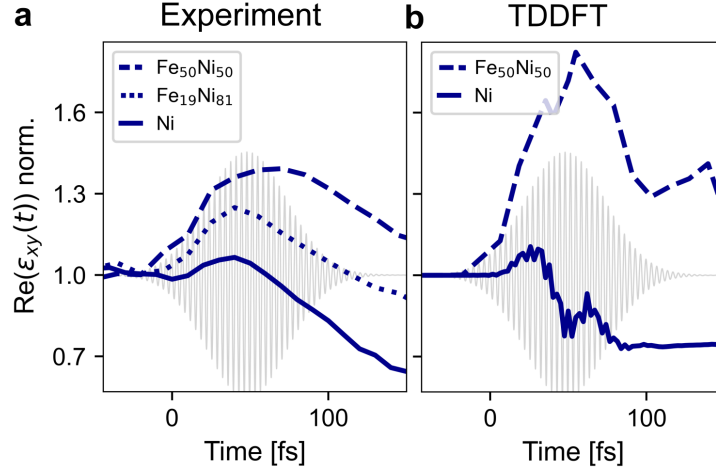
Figure 5.12. – Comparison of the transient off-diagonal tensor element $Re(\epsilon_{xy})$ for 63.9 eV for $Fe_{50}Ni_{50}$, $Fe_{19}Ni_{81}$ and Ni, (a) extracted from measured EUV T-MOKE data, and (b) calculated by TDDFT. The spin transfer between Ni and Fe is visible by an increase of $Re(\epsilon_{xy})$ at 63.9 eV, which probes Ni minority states below the Fermi level. In experiment, the spin transfer is found to be more efficient in $Fe_{50}Ni_{50}$ than in $Fe_{19}Ni_{81}$. In Ni, minority electrons are excited from below to above the Fermi level, which results in a short and comparatively small increase of $Re(\epsilon_{xy})$. Note that we do not provide data of $Fe_{19}Ni_{81}$ by TDDFT, as due to the large required supercell size the calculation is computationally very costly and was therefore not performed for the present study. Reprinted from [26] in accordance with *Creative Commons Attribution 4.0* (**CC BY 4.0**) license.

We determine the origin of the excitation efficiency to differences in the band-structure of the materials, and thereby differences in the possible excitation pathways. For Ni, the pumping with $1.2\,eV$ leads to a peaked increase of minority spins above the Fermi-level, which is limited to a small energetic range of $\approx 300\,meV$ (cf. Figure 5.9 (a) and (b)). In FeNi compounds, empty minority Fe states are added to the DOS above E_F, resulting in additional minority channel final states. This allows for transitions from the Ni minority states below the Fermi level to the Fe minority states above the Fermi level, which is immediately apparent from the occupation changes in $Fe_{50}Ni_{50}$ from theory in Figure 5.13. Note that the number of available Fe minority states above E_F scales with the Fe doping. Thus, the efficiency of the spin transfer between the two subsystems is lower in $Fe_{19}Ni_{81}$ than in $Fe_{50}Ni_{50}$ [161].
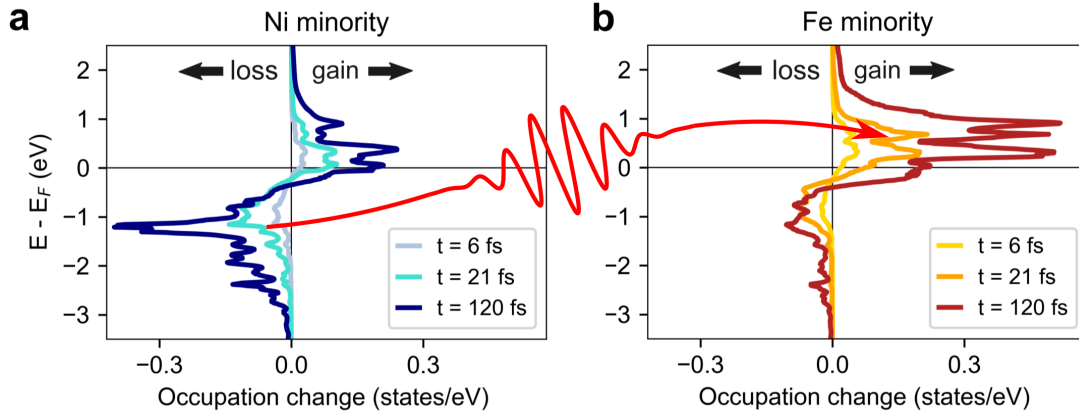
Figure 5.13. – TDDFT calculations of the occupation change in $Fe_{50}Ni_{50}$. The transient occupation change of minority spins at the Ni (a) and Fe (b) sites in $Fe_{50}Ni_{50}$ as calculated by TDDFT. The pump pulse excites minority spins in Ni from below E_F to Fe minority states above E_F. Adapted from [26] in accordance with *Creative Commons Attribution 4.0* (**CC BY 4.0**) license.

In principle, from the theory calculation, we would expect to see the rapid decay of the energy-resolved magnetic moment below the Fermi edge of Fe. Unfortunately, due to the high-harmonic spacing in our experiment, we are not able to probe the relevant energy to see this effect. However, we were able to reproduce the modified efficiency of the spin transfer transition between the three materials.

We conclude that by extracting the real part of the off-diagonal element of the dielectric tensor $Re(\epsilon_{xy})$, we were able to carry out a comparative study of the transient spin transfer dynamics in Ni, $Fe_{19}Ni_{81}$ and $Fe_{50}Ni_{50}$. In particular, through the comparison with TDDFT, we were able to elucidate the origin of the observed signals. For a more complete overview on the spin dynamics in FeNi alloys and the corresponding data analysis, the interested reader is referred to Refs. [26, 85].

Far-from-equilibrium spin dynamics in 3d ferromagnets

The investigation of the non-equilibrium state of magnetic materials after femtosecond optical excitation is fundamental for our understanding of ultrafast spin dynamics. In this regard, consideration of a non-equilibrium between thermalized spin, electron, and lattice subsystems has helped to explain many features of the ultrafast demagnetization process induced by strong optical excitation. Recently, with the discovery of the optically induced intersite spin transfer (OISTR), the importance of the non-thermal far-from-equilibrium state in the electronic system arising upon optical excitation was highlighted and did furthermore indicate the possibility of few-femtosecond spintronic applications [12, 21, 23, 26, 125, 162]. However, a thorough understanding of such femtosecond spin dynamics has remained challenging. The non-equilibrium upon optical excitation presents a state of matter that is not only strongly different from the ground state, but also one that is highly challenging to thoroughly characterize by experimental or theoretical means [163]. Nevertheless, such a characterization is crucial for our understanding of fundamental spin dynamics induced by the laser excitation and their potential future applications. The functionality of magnetic systems is often governed by the complex interplay of several constituents. This makes the understanding of spin dynamics even more challenging. It is therefore essential to first acquire an understanding of the far-from-equilibrium spin dynamics in elemental systems. For this purpose, we consider the prototypical materials for the study of ultrafast magnetization dynamics: the elemental $3d$ FM Ni, Co, and Fe.

In the following, we will present spectrally-resolved T-MOKE asymmetry time-traces of the $3d$ FM, which we will discuss together with time-dependent density functional theory calculations of the occupied density of states. For our interpretation of the observed dynamics, we consider our findings from Chapter 5, where an intriguing effect in EUV

T-MOKE magnetism studies was discussed. The findings from Chapter 5 should therefore serve as a basis for the results presented in this chapter. Note that the analysis to extract the off-diagonal dielectric tensor element ϵ_{xy} has only recently been developed [130] and the necessary angle-resolved measurements could not be performed for further samples investigated in this thesis. Nevertheless, we will use our newly acquired knowledge to carefully review the spectrally-resolved T-MOKE dynamics of all $3d$ FM, Ni, Co and Fe, and examine differences as well as the similarities in the observed dynamics. At the end of the chapter, we extend the discussion to possible microscopic processes driving the ultrafast demagnetization in these systems.

6.1. Spectrally-resolved spin dynamics: experiment and theory

This chapter discusses spectrally-resolved spin dynamics in the prototypical materials for the study of ultrafast magnetization dynamics: the elemental $3d$ FM Ni, Co, and Fe. To ensure the measurement of bulk ferromagnetic properties, we consider nanocrystalline, sputtered thin film samples, namely 21 nm Ni on amorphous $Si_3N_4/Si(100)$, 44 nm Co on MgO(100), and 23 nm Fe on MgO(100)[6.1]. These are driven into a strong far-from-equilibrium state by excitation with a 1.2 eV pump pulse. For each sample, the pump fluence was tuned to achieve a sizeable ultrafast demagnetization. For Ni, Co and Fe, the absorbed pump fluences were 0.8 ± 0.2 mJ/cm², 1.6 ± 0.4 mJ/cm² and 2.5 ± 0.6 mJ/cm², respectively. For the sake of completeness, the data for Ni, which was already presented in the previous chapters, is repeated here and serves for the interpretation of the overall discussion of far-from-equilibrium spin dynamics in laser-excited $3d$ FM. Here, we choose to show the dataset at an angle of incidence of $\theta = 44.8°$, as it was found to best reflect the actual spin spectral dynamics in the system [130].

6.1.1. Spectrally-resolved transient T-MOKE asymmetry

In order to get insight on the spectrally-resolved spin dynamics of the $3d$ FM, the magnetic asymmetry was analyzed in 0.5 eV wide energetic intervals centered on the individual harmonics. The dynamics of the observed magnetic signals are summarized in Figure 6.1.

[6.1]Additional information and standard characterization of the samples can be found in Chapter C.

For specific energies around resonances, we find distinct signatures in the time-resolved
magnetic asymmetry which deviate from the overall expected demagnetization process.
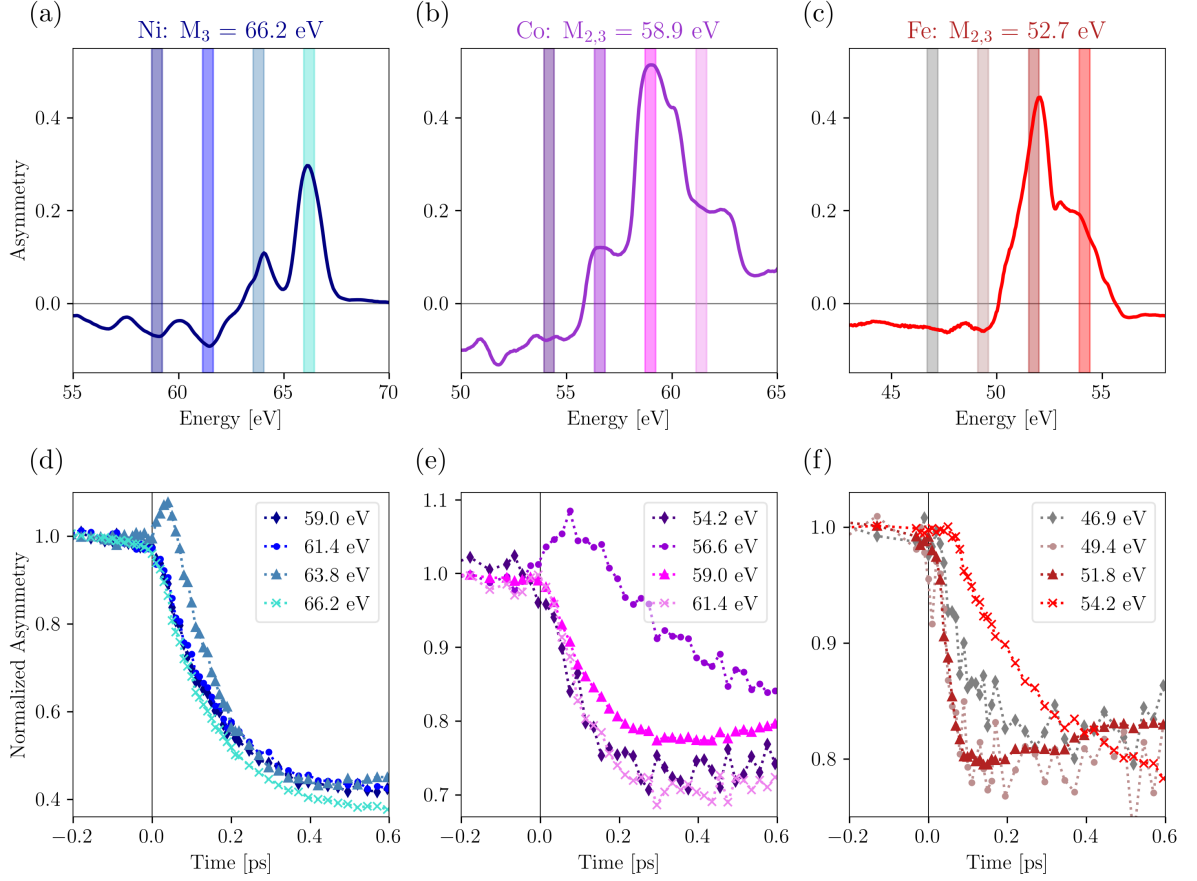
Figure 6.1. – Measured static T-MOKE asymmetries of Ni (a), Co (b) and Fe (c). The indicated 0.5 eV
intervals correspond to the evaluated areas in the asymmetry for the time-resolved analysis. The measured
asymmetry traces of the $3d$ FM as a function of time for EUV photon energies around the resonances
are shown in (d)-(f) for Ni, Co, and Fe, respectively. In all samples, the energy dependent asymmetry
exhibits distinct dynamics, which deviate from the overall expected demagnetization process. These
spectral dynamics are manifested by a rapid increase of asymmetry in Ni and Co below the resonance.
Fe displays a strong dependence of the transient magnetic asymmetry on the probing energy, reflected by
rapid decreases, different onsets and quenchings of the observed dynamics. The values for the M-edges
of the $3d$ FM are taken from Ref. [103].

For many photon energies in each data set, we observe transient dynamics that fit to the
normally observed ultrafast demagnetization process. However, in each data set, we also
observe spectral regions in which the dynamics are strongly deviating from the collective
behavior at other photon energies. For Ni and Co, the most significant deviation from
the usual demagnetization process manifests in an ultrafast increase of asymmetry below
the resonance.

In contrast, the asymmetry signal decreases for all other observed energies. For Fe, on the other hand, we find a rather different behavior of the energy- and time-resolved magnetic asymmetry, where for all energies below the resonance the asymmetry rapidly decreases. Strikingly, we observe at photon energies of 49.4 eV and 51.8 eV, that the transient asymmetry reaches its minimum in less than 100 fs (pastel red and dark red in Figure 6.1 (f)). In addition, at 54.2 eV the onset of the spin dynamics is significantly delayed with respect to all other energies.

Finally, we find that these atypical asymmetry increases, rapid decreases, and delayed onsets in all of the elements are found at very early times, i.e., during and just after the optical excitation. Thereafter, the usual and well-known demagnetization processes dominate the response, and a decrease of the magnetization is observed for all samples and at all energies.

A naive approach to these observed distinct dynamics would be a direct interpretation of the dynamics as increases, decreases, and delays of the energy-resolved magnetic moment. However, as prominently illustrated by the example of Ni in Chapter 5, direct inference from T-MOKE asymmetry time-traces can under certain circumstances lead to misinterpretations of the actual spin dynamics. This is exactly the case, when the angle between the *probe vector* $\vec{p}_\theta$ and the off-diagonal dielectric tensor $\epsilon_{xy} \sphericalangle(\vec{p}_\theta, \vec{\epsilon}_{xy})$ approaches 90°. The best approach for the interpretation of the spectrally-resolved T-MOKE data was therefore found to be the extraction of the transient evolution of ϵ_{xy}. However, since no angle-resolved data for Co and Fe are available at this point, an interpretation of the dynamics via this analysis is not possible. Instead, we attempt to shed light on the origin of the observed dynamics by *ab initio* calculations of the occupied density of states that consider all possible transitions and the according redistribution of electrons and spins in the density of states as a function of time.

6.1.2. Ab initio calculations of the occupied density of states

In order to get a more complete view on the actual spin dynamics in the $3d$ FM after optical excitation, TDDFT calculations of the occupied DOS were performed by the group of Sangeeta Sharma. For the calculations, a pump pulse with a central photon energy of 1.2 eV, a Gaussian intensity profile with FWHM = 36 fs and a fluence of $\approx 9\,\mathrm{mJ/cm^2}$ was used. From the theory, it is possible to fully determine the spectrally-resolved optically-

induced modifications in the occupation of the majority and minority spin channels with respect to the unperturbed material.

In Figure 6.2 (a)-(c), the population difference of the spin-resolved occupied density of states is shown as a function of energy for different timesteps during the optical excitation. For both Ni and Co, a dominant loss of charge carriers below E_F is found in the minority states, as indicated by the solid lines. The most pronounced change in the charge occupation can be found at low energies of $\approx 0.5 - 1.5\,\text{eV}$ below E_F, where the DOS is most strongly affected by the $1.2\,\text{eV}$ pump pulse, leading to a depletion of dominantly minority states. However, also at energies below -1.5 eV, the DOS of both elements is affected by the pump excitation, with greater losses in the minority states. This dominant loss is best illustrated by the energy-resolved magnetization change calculated as the difference of the ground state M_0 and $M(t)$ at $59\,\text{fs}$, as shown in Figure 6.2 (d)-(e). Here, positive values below E_F indicate an overall increase in the energy-resolved magnetization due to the loss of minority electrons. The excited charges end up in the unoccupied DOS, as visualized by the peaked increase of minority spins above E_F (Figure 6.2 (a) and (b)).

For Fe, the TDDFT calculations of the occupied density of states after optical excitation show a rather different behavior of the spin dynamics. From the population change during excitation, it is possible to identify energetic regions where predominantly minority carriers are excited, and regions with approximately equal contributions from both channels, but also regions with predominant depletion of majority carriers (see Figure 6.2 (c) and (f)). Overall, the changes in the occupation of both spin channels are more complex compared to Ni and Co.

Note that for Ni the redistribution of charges leads to an occupation in a relatively small energetic range ($\approx 300\,\text{meV}$) above the Fermi level, where empty states are available. In contrast, Co and Fe have substantially larger unoccupied DOS above E_F, allowing for an excitation of charges even up to more than $2\,\text{eV}$ above E_F for the case of Fe.
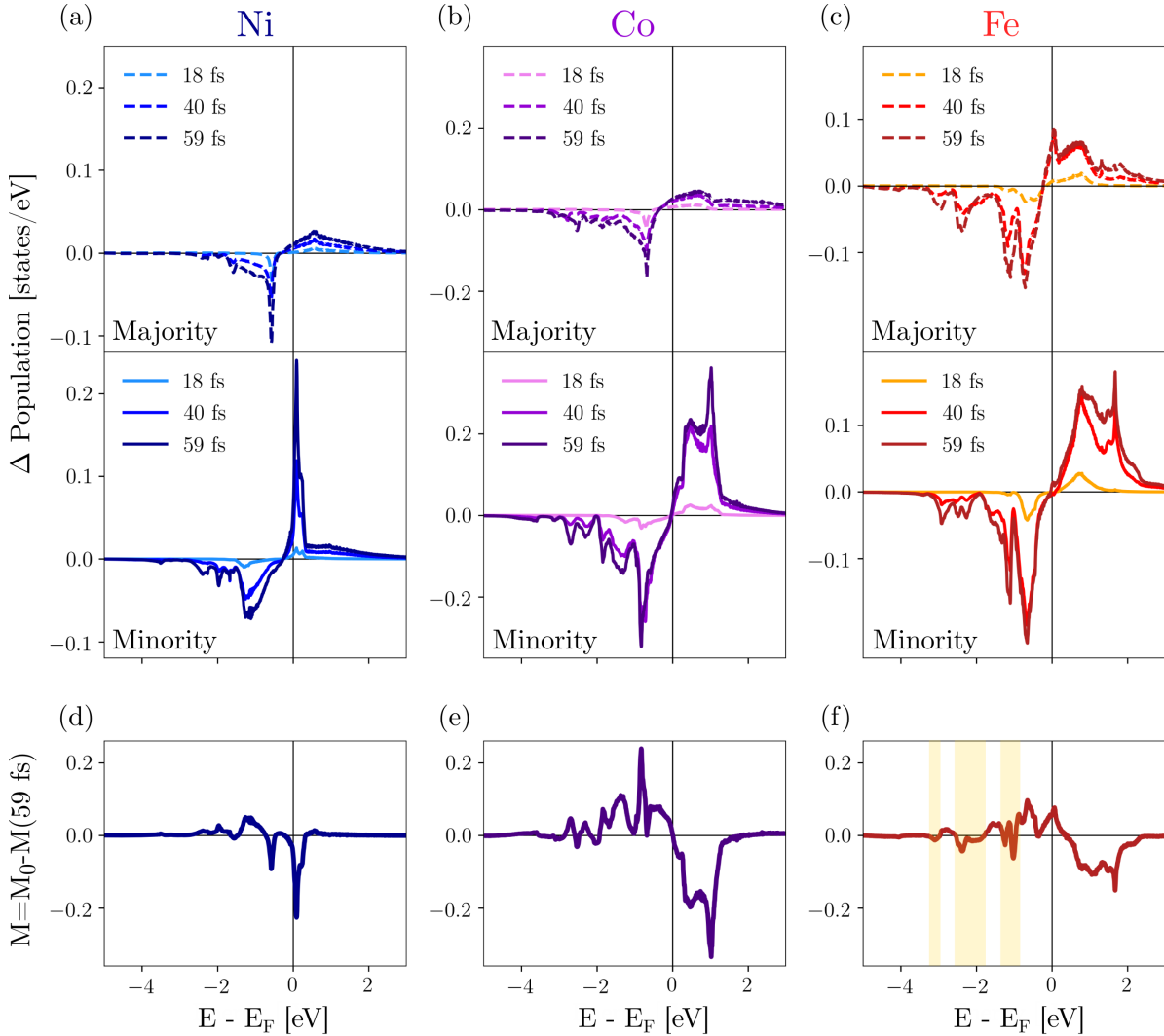
Figure 6.2. – TDDFT results of optically-induced spin dynamics in (a) Ni, (b) Co and (c) Fe. The top and middle row show the population change as a function of binding energy for the minority and majority spin states, respectively, while the bottom row ((d)-(f)) shows the energy-resolved magnetization change calculated as the difference of the ground state M_0 and $M(t)$ at 59 fs after the optical excitation. In Ni and Co, a dominant loss of minority carriers below E_F compared to a much smaller change in the majority carriers is apparent. The population loss below E_F is accompanied by a gain of charges above E_F. For Fe, a loss of charge can be found in both spin channels below E_F (regions with predominant loss of majority carriers marked in yellow), accompanied by a gain of charges above E_F.

6.1.3. Combining experiment and theory

Next, we attempt to classify our findings, joining the results from experiment and theory. At this point, one has to consider that an exact quantitative comparison of experiment and theory is challenging, as T-MOKE probes the dielectric tensor rather than the occupied local density of states that was calculated by TDDFT. However, clearly, the comparison of the results from experiment and TDDFT enables a more complete view on the far-from-equilibrium spin dynamics.

Another key aspect of our detailed analysis of the magneto-optical signal in Chapter 5 was the better understanding of the magneto-optical signal itself. Due to the linewidth of the initial $3p$ states, a specific EUV energy can probe an extended region of several electron-volts in the unoccupied density of states of the material. Thus, the magneto-optical signal yields a broadened response of all the distinct signatures induced by the pump excitation (see Figure 6.2). Based on this, we revisit the theory results of optically-induced spin dynamics in the $3d$ FM. For Co and Ni, we find a strong minority inter-energy transfer of spins from below to above the Fermi-level. For Co, where the dominant excitation of minority charges is clearly visible down to approximately $-3\,\mathrm{eV}$ below E_{F}, this effect is even stronger than for Ni. Similarities are also found in the transient T-MOKE asymmetry, where we find an ultrafast increase below the resonance (see Figure 6.1 (a) and (b)). In contrast, both TDDFT calculations and experimental asymmetry time-traces for Fe present an entirely different behavior. For Fe, the transient asymmetry rapidly decreases, shows delayed behavior and different demagnetization times depending on the probe energy. This manifold behavior is also illustrated by the calculated population changes, where both minority and majority electrons contribute strongly to the excitation of charges. On this basis, the question of a classification of the spin dynamics according to the concepts of strong (Ni, Co) and weak (Fe) ferromagnetism arises.

Classification of the dynamics according to weak and strong ferromagnetism?

In the strong ferromagnets Ni and Co negligible majority d-states exist above E_{F} and the dominant available contribution of charge redistribution by the laser pulse must be expected within the minority d-states (see Figure 6.3 (a)). Initially, the pump excitation therefore leads to a depletion of minority states at distinct energies below E_F and to a matching occupation of minority states above E_F, as calculated in theory. Furthermore, we know from our analysis of the spectrally-resolved dynamics of Ni and the corresponding TDDFT calculation in Chapter 5 that the depletion of minority carriers below E_{F}
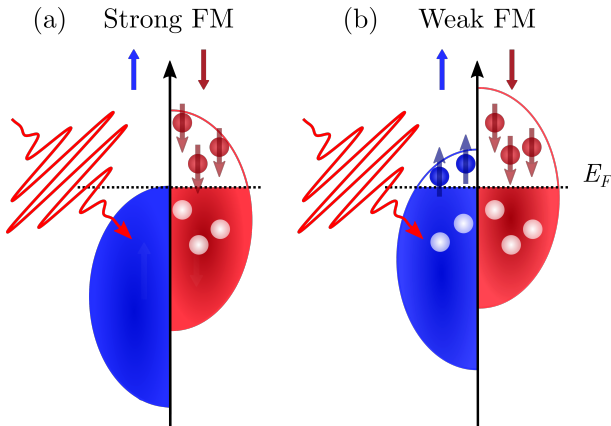
Figure 6.3. – Schematic overview of the optically induced dynamics in a strong and weak ferromagnet. (a) In strong ferromagnets (Ni and Co) negligible majority d-states exist above E_F and the dominant available contribution of charge redistribution by the laser pulse must be expected within the minority d-states. (b) For the weak ferromagnet Fe, where both majority and minority states are present around E_F, the situation is more complex as excitation from both majority and minority states below E_F can be expected.

also manifests in an increase of the off-diagonal dielectric tensor below the resonance (see Figure 5.9 (d) in Chapter 5). From the overall similarities of the experimental and theoretical data of Ni and Co, it is concluded that the observed increase in the T-MOKE data of Co below the resonance is indicative of a strong inter-energy transfer of minority carriers. An increase of the magnetic moment below the Fermi level of Co after optical excitation, was also recently proposed by PONTIUS and coworkers in a joint work of theory (TDDFT) and experiment (helicity-dependent soft X-ray absorption spectroscopy (HXAS) at the L-edges of Co) [164]. As in the present work, the authors also find the increase in magnetic moment at early times to be a consequence of the spin-preserving excitation of minority electrons from below the Fermi energy. Further, it is argued that the initial increase in magnetic moment below E_F is interrupted once spin-flip processes begin to dominate over optical excitations and lead to the demagnetization of the material. The spin-flip processes belong precisely to the processes that we have previously described as the usual and well-known demagnetization processes, which drive the overall reduction in magnetic moment after optical excitation.

For the weak FM Fe, where both majority and minority states are present around E_F, the situation is more complex, as excitation from both majority and minority states below E_F can be expected (visualized in Figure 6.3 (b)). The population change in Figure 6.2 (c), as determined by TDDFT calculations of the occupied density of states, reflects the complex interplay of both spin channels in the charge excitation. Note that it is challenging to compare excitation channels directly in Fe between experiment and theory, due to the strong energy dependence of spin dynamics in theory and the energetic smearing of these dynamics in experiment. Further, a precise determination of the Fermi energy cannot be achieved by our experiment, i.e., E_F can only be determined from tabulated values

of the M-edge[6.2]. Despite these facts, the TDDFT results indicate clearly that the weak ferromagnet Fe should behave strongly different from the strong ferromagnets Ni and Co, as is indeed observed in our experiment.
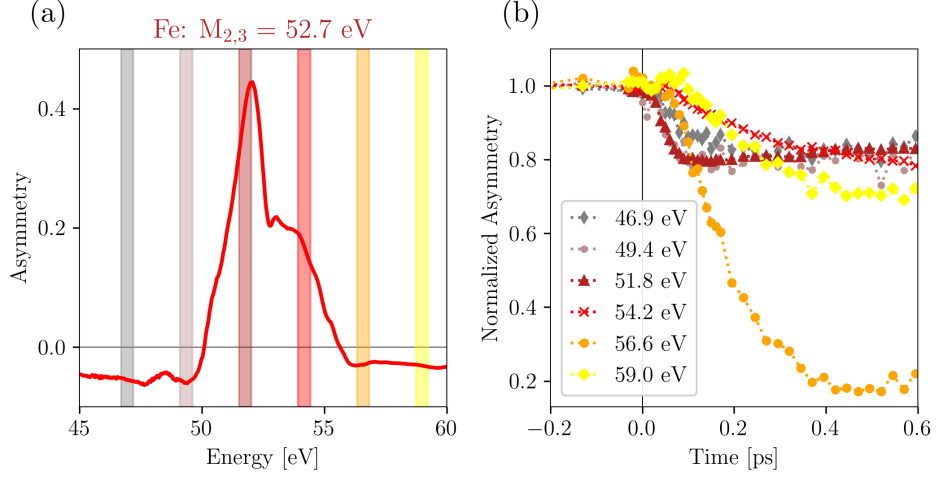
Figure 6.4. – (a) Static magnetic asymmetry of Fe. The indicated $0.5\,\mathrm{eV}$ intervals correspond to the evaluated areas in the asymmetry for the time-resolved analysis. (b) The transient magnetic asymmetry for different energies around the resonance indicates the complexity of the optically induced dynamics. Overall, we observe strongly different onsets, quenchings and demagnetization times for different harmonic energies.

The complexity of the dynamics induced by the laser pulse in the weak FM Fe is further illustrated when considering energies far above the resonance. For Fe, the asymmetry spans up to several electronvolts above the resonance. For these high energies, shown in Figure 6.4, we again find very different dynamics with different onsets, quenchings and demagnetization times compared to all other energies. Note that transient changes of the magnetic asymmetry for energies several electronvolts above the resonance were also found for Co. However, here we find a rather homogeneous behavior of the magnetic asymmetry traces, as shown in Figure C.3 in Chapter C.

Overall, these results raise the question of how the optical excitation can affect the magnetic asymmetry so far above the Fermi energy. In the following, we try to get to the bottom of this question by considering different magnetic excitation processes upon demagnetization.

[6.2] The values of the M-edges of the $3d$ FM can vary depending on the reference. Here, we use the tabulated values of Ref. [103].

6.2. Particular dynamics depending on the type of magnetic excitation?

In a next step, we attempt to discuss our findings of the transient magnetic asymmetry of Ni, Co, and Fe upon demagnetization in the context of commonly considered processes during the ferromagnetic-paramagnetic phase transition after optical excitation. Here, we will focus on secondary processes which occur on longer timescales ($>100\,\text{fs}$) which lead to the overall demagnetization of the systems compared to coherent effects like OISTR-like spin transfer processes.
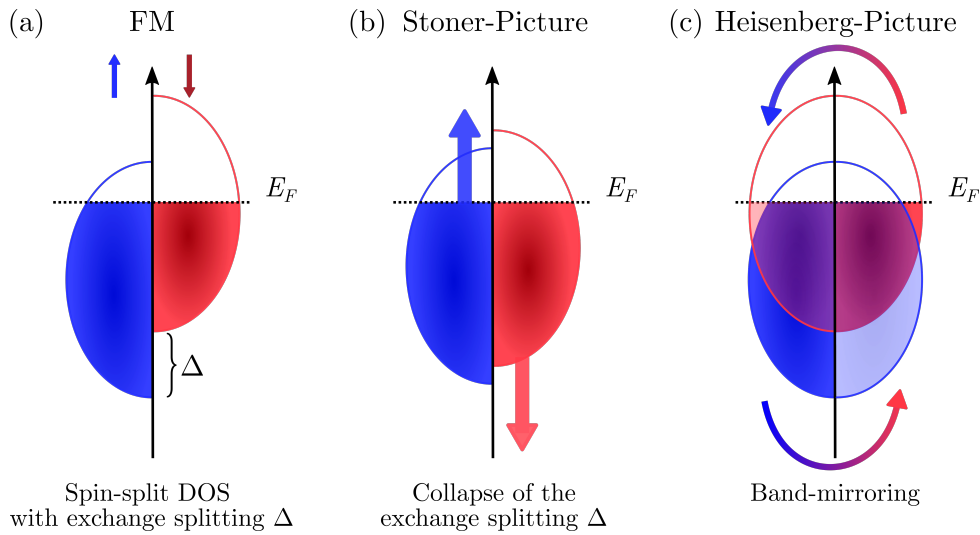
Figure 6.5. – Schematic of potential band structure renormalization in laser-induced demagnetization. (a) Spin-split DOS of a $3d$ FM. (b) Reduced magnetization in the Stoner-like picture induced by a collapse of the exchange splitting Δ and (c) by the collective excitation of magnons in the Heisenberg picture, leading to a band-mirroring effect of the majority and minority bands. Inspired by [70].

Mainly, two mechanisms are discussed in the context of ultrafast demagnetization of $3d$ FM and can be divided into the pictures of the Stoner model of itinerant ferromagnetism on the one hand and the Heisenberg picture of localized spins on the other [67, 70, 71]. Both mechanisms have been heavily discussed to drive ultrafast demagnetization in the simple ferromagnets and are sketched in Figure 6.5 (b) and (c) [66, 67, 70, 71, 165]. In the Stoner-like picture, the magnetization is reduced via single-particle excitations (longitudinal spin-flip processes) that result in an overall collapse of the exchange splitting of the FM. This results in a shift of the d-bands. The Heisenberg picture considers correlated spin excitations, namely magnons, which reduce the net mag-

netization by creating a spatially and time-dependent modification of the spin orientation.
Under experimental conditions, only the macroscopic average of these spin fluctuations
can be measured, thus resulting in the measurement of a band-mirroring of the spin-split
DOS. In the past, contributions of both types of mechanisms have been intensively de-
bated in the context of ultrafast demagnetization of the $3d$ FM with no conclusive and
even contradictory experimental results [65–67, 70, 71, 165].

In a combined study of EUV T-MOKE experiment and density functional theory (DFT),
Jana et al. try to shed light on the origin of the spectrally distinct signatures in the
transient magnetic asymmetry of Ni and Fe (see Figure 2.5), precisely by considering
the above-mentioned different types of magnetic excitations [28]. For this purpose, the
authors performed *ab initio* calculations to determine the relationship between the off-
diagnoal dielectric tensor ϵ_{xy}, the magnetic asymmetry and the magnetization. For the
theory work, different types of magnetic excitations were modeled consisting of:

- Stoner-like excitations

- long wavelength magnon excitations, corresponding to gradually tilted magnetic
  moments

- and short wavelength magnons, corresponding to randomly tilted magnetic mo-
  ments.

For Fe, the magnetic asymmetry and ϵ_{xy} are strongly dependent on the specific type of
excitation, as demonstrated by the calculations of $Re(\epsilon_{xy})$ in Figure 6.6. In particular,
Stoner-like excitations show clear fingerprints in the off-diagonal component of the di-
electric tensor. This is especially pronounced for energies above the resonance (indicated
by a red arrow), where significant changes in the spectral features of $Re(\epsilon_{xy})$ can be ob-
served. From the connection of the T-MOKE asymmetry and $Re(\epsilon_{xy})$ in Equation 5.6,
a reflection of these signatures in the magnetic asymmetry is not surprising and even
expected. According to the calculations of $Re(\epsilon_{xy})$ in Figure 6.6, the evolution of the
transient magnetic asymmetry of Fe must show drastically different behavior depending
on the selected energy and the specific type of excitation. In contrast, for Ni, the con-
sidered different types of excitations were found to produce practically indistinguishable
modifications in $Re(\epsilon_{xy})$ (see Figure 6.6 (d)-(f)). $Re(\epsilon_{xy})$ displays an overall reduction
around the resonance, without evident energy-dependent specific signatures. Thus, the
transient magnetic asymmetry can be expected to be rather insensitive to the type of
excitation and to display an energy-independent homogenous behavior.
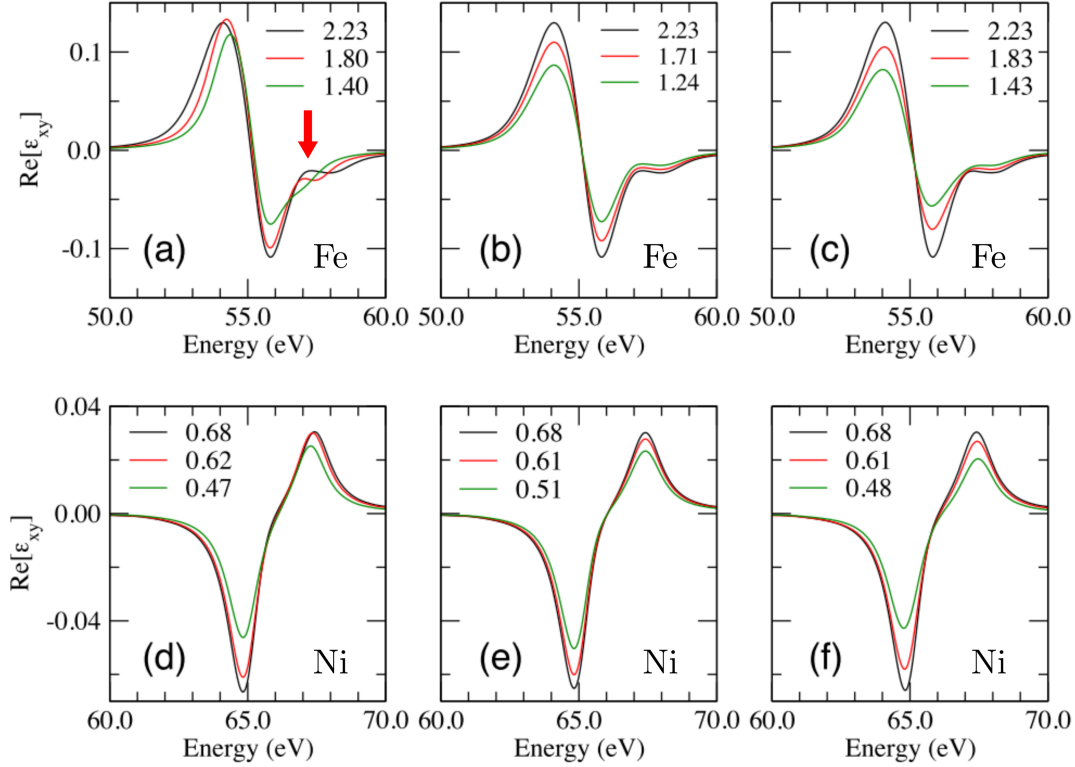
Figure 6.6. – Calculated real part of the off-diagonal component of the dielectric tensor ϵ_{xy} for different values of reduced magnetization $[\mu_B]$. Panels (a) - (c) show the results obtained for Fe and (d) - (f) the results for Ni. Calculations for Stoner-like excitation in panels (a) and (d), long wavelength magnon excitations in panels (b) and (e), and a high density of short wavelength magnons in panels (c) and (f). Adapted and reprinted from Ref. [28] in accordance with *Creative Commons Attribution 4.0* (**CC BY 4.0**) license.

Note that distinct fingerprints in the magneto-optical signal depending on the specific type of excitation (Stoner-like or spin-wave) have already been predicted in earlier studies [71, 89]. For Co, both Stoner-like excitations and ultrafast magnon generation were found to drive the ultrafast demagnetization by combining ultrafast time-, energy-, and angle-resolved measurements of T-MOKE at the Co resonance with advanced *ab initio* magneto-optical calculations [71]. However, both mechanisms were found to act on different timescales: a strong magnon contribution to ultrafast demagnetization on sub-picosecond timescales and a persistent reduction in the exchange splitting (Stoner-like excitations) up to several picoseconds.

In this work, we find the overall behavior of the transient magnetic asymmetry of Fe to be in line with the results of JANA et al. [28]. Fe displays a strong dependence of the transient magnetic asymmetry on the probing energy, while the transient magnetic asymmetry of Ni and Co decreases homogeneously for most evaluated energies. In general,

an overall homogenous behavior of the spin dynamics is suggestive for the generation
of magnons, which act in the same way for all energies. The collapse of the exchange
splitting, however, is more likely to induce energetically distinct dynamics. Due to the
irregular shape of *d*-states of Fe (see Figure 6.7), a shift of the *d*-bands should lead to
strong changes in the energy-resolved spin-polarization, resulting in energy-dependent
distinct spin-dynamics. For Ni and Co, which have a more regularly shaped DOS, this
effect should be less pronounced.
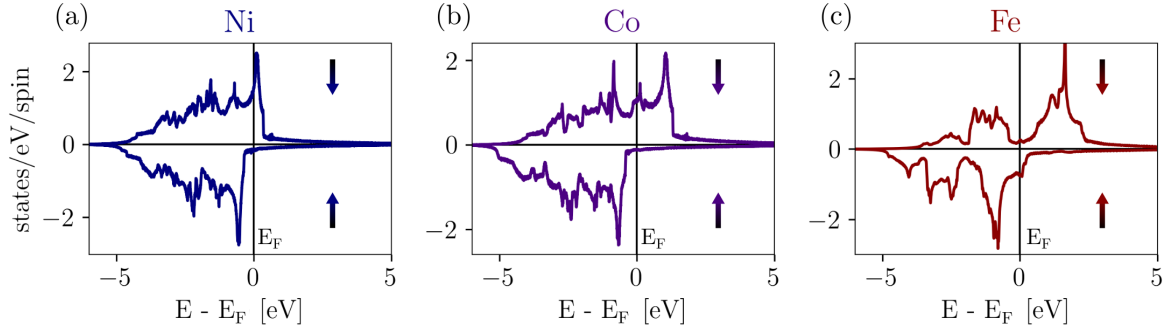
Figure 6.7. – Spin-split density of states of the $3d$ FM Ni (a), Co (b), and Fe (c). The strong FM Ni
and Co have a more regularly shaped DOS compared to the weak FM Fe.

In first approximation, the theory results of JANA et al. in Figure 6.6 support a strong
contribution of Stoner-like excitations to the demagnetization of Fe, which manifest in
a strongly energy-dependent behavior of $Re(\epsilon_{xy})$. On the contrary, it was found by
CARPENE et al. using femtosecond magneto-optical and reflectivity spectroscopy that
magnon generation (collective excitations) dominates the demagnetization process in Fe
[65]. This finding was further supported by GORT et al. with time- and energy-resolved
photoelectron spectroscopy measurements of Fe/W [67, 165]. Note that the spin-transport
properties of the underlying substrate can affect the observed spin dynamics and might be
responsible for partially contradicting experimental results. For example, the demagneti-
zation of Co on Cu(001) in the first 100 fs was found to be mainly driven by spin currents,
which induce a band-mirroring in the electronic structure [70]. In contrast, significantly
slower demagnetization times were reported for Co on insulating substrates [71, 166].
In order to further investigate microscopic mechanisms that are likely to be responsible for
the demagnetization of Fe, we performed transient *s*-polarized reflectivity measurements.

6.2.1. Transient reflectivity measurements of Fe

The transient *s*-polarized reflectivity change for different photon energies around the Fe
resonance is shown in Figure 6.8. The absorbed fluence of 2.5 ± 0.6 ᵐᴶ/cm² of this mea-
surement was chosen to be equivalent to the T-MOKE measurement in Section 6.1.1. In
the first 100 fs, we find the reflectivity of Fe to be affected in a large energetic range down
to several electronvolts below the resonance. For these energies (46.9 eV to 54.2 eV), the
transient reflectivity displays an ultrafast increase. The largest change of almost 6% is
observed at 51.8 eV, which corresponds to an energy region below E_F. Below that energy
and at 54.2 eV, the reflectivity shows a change of roughly 2%. The reflectivity of the
highest evaluated energies (above E_F) is not affected on this short timescale.
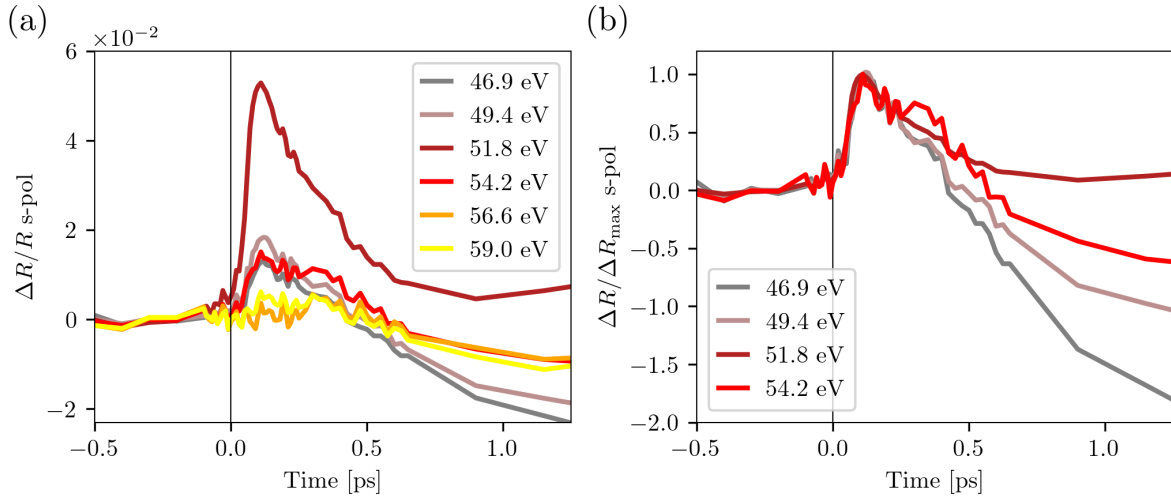
Figure 6.8. – (a) Reflectivity change for different *s*-polarized high harmonic photon energies around
the Fe resonance. In (b) the reflectivity change was normalized to the maximum change for each photon
energy.

Like the changes in the transient magnetic asymmetry, the overall behavior of the reflec-
tivity of Fe differs from the observed behavior of Ni, where an increase in the reflectivity
can only be identified for one energy below the resonance (see Figure 4.6). For Ni, this
increase at 63.8 eV can be traced down to the pump-induced excitation of charges from
below E_F. However, for Fe, where the reflectivity is affected for many probe energies,
the question arises how the pump excitation can modify the electronic occupation so far
below E_F. Generally, the observation of ultrafast dynamics in the transient reflectivity
for energies significantly below E_F can only be achieved by changes in the DOS. At these
energies, the pump pulse cannot be expected to directly excite electrons.

In an attempt to further classify our findings of the transient reflectivity of Fe, we normalized the reflectivity change to the maximum change for each photon energy, as shown in Figure 6.8 (b). The increase in reflectivity in the first 100 fs behaves uniformly for all energies. We find the transient reflectivity changes of Fe around the resonance to be suggestive of a collapse of the exchange splitting, which would indeed change the DOS down to the lowest energies and may also support the observation of different signatures in the spin dynamics far above E_{F} in Figure 6.4. The creation of magnons, on the other hand, could change the spin polarization down to energies well below E_{F}, but no change in the s-polarized reflectivity would be expected, since the actual total electron occupancy would not be changed by the spin mirroring.

Overall, the reflectivity data of Fe supports a dominant contribution of the collapse of exchange splitting Δ to the ultrafast demagnetization. The reflectivity results are thus consistent with the strongly energy-dependent behavior of the transient magnetic asymmetry, which according to calculations of $Re(\epsilon_{xy})$ (in Figure 6.6 (a)) could be related to Stoner-like excitations. It should be noted that further processes contributing to demagnetization cannot be excluded and that the results presented here should only be taken as an indication for the possible underlying microscopic processes.

Conclusion

In conclusion, we have presented spectrally-resolved spin dynamics of the ferromagnetic transition metals Ni, Co, and Fe and find very rich and distinct dynamics of the transient T-MOKE asymmetry around the M-edges. These results shed new light on a number of transient signals that were recently reported [28–30]. Our experimental findings and the comparison to TDDFT calculations of the occupied density of states provide evidence that distinct energy-resolved spin dynamics in Ni, Co, and Fe at early times after optical excitation are connected to a far-from-equilibrium electron distribution. At this early stage, the observed energy-resolved magneto-optical asymmetry change is dominated by energetically distinct spin-conserving charge transitions, which we were able to unambiguously identify for Ni by the extraction of $Re(\epsilon_{xy})$ in Chapter 5. Further, we find that the energy-resolved dynamics of the $3d$ FM on the sub-100 fs-timescale can be classified according to the concepts of strong and weak ferromagnetism. However, we note that future experiments are necessary to verify this hypothesis, as we found the T-MOKE magnetic asymmetry may show time-dependent behavior that is not directly connected to the magnetic properties of the sample [130]. In order to verify charge and spin excita-

tion channels in Co and Fe, future investigations should be based on an angle-dependent
measurement of the transient magnetic asymmetry, which enables a direct comparison
with TDDFT via our analysis for the determination of $Re(\epsilon_{xy})$.

Beyond the sub-100 fs-timescale, the transient dynamics of Ni and Co were found to be-
have rather homogeneously, whereas the dynamics in Fe are strongly dependent on the
probing energy. The diverse behavior of the energy-resolved magnetic asymmetry in com-
bination with theory calculations of $Re(\epsilon_{xy})$ from Ref. [28], as well as transient s-polarized
reflectivity measurements, provide indication that a collapsing exchange splitting domi-
nates the demagnetization of Fe. In contrast, intuitively, an energy-independent behavior
of the transient spin dynamics of Ni and Co would suggest the generation of magnons.
The contribution of both processes, band-mirroring and collapse of exchange splitting, to
ultrafast demagnetization has been intensively discussed in recent years, but a general
statement about the magnetic excitations in ultrafast demagnetization of $3d$ FM has re-
mained elusive [66, 67, 70, 71, 166]. We note that our findings contribute towards the
understanding of ultrafast demagnetization in these systems, however, at this point we
cannot yet provide clear evidence on the actual microscopic processes that are responsible
for the demagnetization of these systems.

Conclusion

7

In this thesis, the laser-induced spin and charge dynamics in the $3d$ FM Ni, Co, and Fe were explored with a novel T-MOKE setup in the EUV spectral range. In particular, the focus was laid on dynamics that occur during or shortly after the optical excitation ($< 100\,\mathrm{fs}$), when the electron system is in a far-from-equilibrium state. This state is highly challenging to characterize with experimental and theoretical means [163]. Within this context, the goal was to investigate the dependence of the T-MOKE asymmetry on the probing energy and to identify distinct optically-induced spin and charge dynamics in the band structure of the materials. As motivated by recent previous studies [28–30], distinct spectral dynamics are expected in the M-edge magneto-optical signal of the $3d$ FM, however, a thorough understanding of the origin of these dynamics has remained elusive so far.

In the following, I will summarize our findings by answering the research questions that were raised at the beginning of this thesis.

Starting point of the spectrally-resolved analysis of the $3d$ FM was to gain a better understanding of our experimental observable, i.e., the T-MOKE asymmetry.

> What is the relationship between the T-MOKE asymmetry and other magneto-optical quantities, such as the magnetization? Can we relate the T-MOKE asymmetry at a given energy directly to the energy-resolved magnetic moment?

A key message of this thesis is that the relationship between the T-MOKE asymmetry and other magneto-optical quantities is more complex than earlier works have suggested. In previous studies, the T-MOKE asymmetry was frequently treated as being in first approximation linearly proportional to the off-diagonal dielectric tensor ϵ_{xy} and thus also as linearly proportional to the magnetization [74, 120, 145]. However, as discussed in Chapter 5, neither the magnetization nor the energy-resolved magnetic moment are directly measured in T-MOKE experiment. The fact that a linear relationship between the

energy-dependent T-MOKE asymmetry and the magnetic moment is not always valid has previously been discussed in Ref. [28]. We note that the experimental observations of OISTR [12, 21–24, 26] demonstrate that the spin dynamics can vary considerably as a function of the photon energy. This shows that a uniform transient behavior of the energy-resolved asymmetry $A(E)$ cannot ultimately be assumed.

In fact, the most surprising finding of this thesis is discussed in Chapter 5, where we show that depending on the angle of incidence, drastically different dynamics of the transient T-MOKE asymmetry of Ni can occur, i.e., an increase, a delay, and a decrease for the same energy below the resonance. Therefore, a direct interpretation of the transient asymmetry can be highly problematic and a straightforward translation into spin dynamics is often not possible. However, by analyzing this critical observation, we introduce a new and simple description of the T-MOKE asymmetry, which we can express as the inner product of $\vec{\epsilon}_{xy}$ with a *probe vector* $\vec{p}_\theta$, where $\vec{p}_\theta$ depends solely on the angle θ_i and the refractive index n of the material. The T-MOKE asymmetry can then be understood as the projection of ϵ_{xy} on the probe vector $\vec{p}_\theta$. When the angle $\sphericalangle(\vec{p}_\theta, \vec{\epsilon}_{xy})$ between these vectors approaches 90°, the asymmetry is particularly dependent on the geometric factors and can lead to a change from positive to negative projection within a small angle range. For this particular case, a small rotation of either of these vectors can lead to unexpected dynamics in the transient T-MOKE asymmetry signal, as observed for Ni below the resonance. Based on this, we were able to develop a fitting procedure that allows to extract the off-diagonal dielectric tensor element ϵ_{xy} and optical changes of the refractive index n with full temporal resolution. We are thus able to disentangle the contributions of charge and spin dynamics to the magneto-optical signal. As TDDFT is able to provide the transient dynamics of the dielectric tensor element ϵ_{xy}, we can now also provide a direct comparison between experiment and theory. In combination with calculations of magnetic moment and occupation changes in the spin-split DOS (also accessible by TDDFT), we can finally directly analyze other magnetic properties such as the magnetization and the energy-resolved magnetic moment. Overall, we provide a method which allows us to trace optically-induced spin and charge dynamics in exceptional detail.

> What is the role of charge and spin dynamics on the ultrashort timescale? Is it possible to identify OISTR-like processes within a single element?

Via the direct calculation of the real part of the off-diagonal dielectric tensor element $Re(\epsilon_{xy})$, we were able to trace the pump-induced spin dynamics in Ni at early times

of the optical excitation (< 50 fs). Comparing our results to TDDFT calculations, we were able to unambiguously identify an optically driven inter-energy spin-transfer process in Ni, which is expressed by an increase of $Re(\epsilon_{xy})$ below the resonance. We find that the pumping of spins happens predominantly in the minority channel and leads to a spin-conserving excitation of charge from below to above the Fermi level. Thus, we were indeed able to identify an OISTR-like process within a single element.

With our approach, we are also able to address the constantly discussed question of non-magnetic artifacts to the magneto-optical signal.

> Can we exclude optical artifacts in the T-MOKE asymmetry?

The spin-transfer process in Ni is accompanied by a strong redistribution of charges, resulting in a significant increase of the EUV absorption below the Ni resonance. This strong change in the absorption is also reflected in the magneto-optical signal and was found to lead to a non-symmetric behavior in the reflected T-MOKE intensities $I_{\uparrow/\downarrow}(t)$. However, our time-resolved analysis reconstructs both magnetic (ϵ_{xy}) and non-magnetic (δ and β) contributions to the magneto-optical signal, which can now be examined separately. Thus, we find the change of the $\vec{p}_\theta$ vectors to be insignificant in comparison to ϵ_{xy} and conclude that the angle-dependent behavior of the transient T-MOKE asymmetry is dominated by the rotation of ϵ_{xy} and not by non-magnetic contributions to the magneto-optical signal.

In Chapter 6, the transient energy-dependent T-MOKE asymmetry was discussed for all $3d$ FM. Our study was motivated by recently published results of the spectrally-resolved magneto-optical behavior of the $3d$ FM in the EUV spectral range [28–30], which led us to the following research question:

> Is it possible to pinpoint differences and similarities in the spectral dynamics of the $3d$ FM?

First, the $3d$ FM represent the simplest systems to investigate the complex interplay of spin and charge dynamics in the far-from-equilibrium state. However, even for these simple materials, we find a strong dependence of the T-MOKE asymmetry on the particular probing energy. In particular, the transient dynamics of Fe were found to be strongly different from the dynamics observed for Ni and Co. In combination with

TDDFT calculations of the population changes in the spin-split DOS, we were able to classify the observed dynamics according to the concepts of strong (Ni and Co) and weak (Fe) ferromagnetism. From the overall similarities in the experimental and theoretical data of Co and Ni, we also find in Co evidence for an inter-energy transfer of minority carriers from below to above E_{F}, even though at present, we do not have access to the full ϵ_{xy}-analysis. In Fe, however, excitations from both spin channels apparently lead to highly complex changes in the occupation of the spin-split DOS.

Beyond the sub-100 fs-timescale, we discussed our results in the framework of different types of magnetic excitations. From the overall homogeneous behavior of the energy-resolved asymmetry in Ni and Co, we consider the generation of magnons as the predominant excitation process. For Fe, the diverse behavior of the energy-resolved magnetic asymmetry and the changes of the transient s-polarized reflectivity over a broad energy range around E_{F} provide indication that a collapsing exchange splitting contributes strongly to the demagnetization.

In summary, within the scope of this thesis we have built a T-MOKE setup in the EUV spectral range, which allowed us to investigate the spectrally-resolved magnetization dynamics of the $3d$ FM with excellent data quality and high signal-to-noise ratio [115, 130]. Through our in-depth study of the energy-resolved T-MOKE asymmetry, we have gained valuable insights on how the T-MOKE measurement signal should be understood and which connections exist between the magneto-optical signal and other magnetic properties, i.e. ϵ_{xy}, the magnetization and the energy-resolved magnetic moment. We presented an intriguing effect, where under almost identical experimental conditions, drastically different transient dynamics of the T-MOKE asymmetry were observed. To overcome the challenge of interpreting these surprising results, we developed a sophisticated analysis in order to directly extract the off-diagonal dielectric tensor element ϵ_{xy} and refractive index changes n with full temporal resolution. The reconstruction of optical changes in addition to ϵ_{xy} also extends previous approaches reported by ZUSIN et al. and TURGUT et al. [68, 71]. By separating the magnetic and non-magnetic contributions to our magneto-optical signal, we address the long-lasting debate of optical artifacts to the measurement signal [31–39, 145]. In addition, our analysis provides a direct comparison to TDDFT calculations and ensures that spectral broadening, multiple edges and overlapping edges of different elements are taken into account.

We note that despite the fact that our newly developed analysis could not be applied to all the data presented in this thesis, our findings on the spectrally-resolved spin dy-

namics in the $3d$ FM contribute towards the understanding of ultrafast demagnetization in these systems. Finally, we note that within the last few years, the interest on spectrally-resolved data from materials driven strongly out of equilibrium has been growing constantly. Therefore, we are convinced that our findings and the corresponding interpretations will be of valuable interest for the magneto-optics community.

Outlook

At last, I would like to point out future studies based on the results of this thesis. A logical outlook on the results in Chapter 6 is to perform angle-resolved measurements of the transient T-MOKE asymmetry of Co and Fe. This allows the application of our novel fitting routine to extract ϵ_{xy}. Thereby, we could verify our interpretation of the spin dynamics and would ensure a better comparability with theory calculations. It is worth to mention that even static measurements at different incidence angles can serve as a good starting point to reveal critical regions in the T-MOKE asymmetry. Particular attention must be paid to regions that are close to zero crossings, which suggest that the angle $\sphericalangle(\vec{p}_\theta, \vec{\epsilon}_{xy})$ approaches $90°$. We note that a different approach to reunite results from T-MOKE experiment and theory has recently been used in Ref. [25], where a direct comparison between experiment and theory was ensured by the determination of the transient T-MOKE asymmetry by means of TDDFT.

To overcome the limitations of our experiment due to spectral broadening, a combined study of the T-MOKE experiment and spin-resolved photoemission could provide valuable additional insights into the spin dynamics of the $3d$ FM. In particular for Fe, on the sub-100 fs-timescale, complex occupation changes in the DOS of the material are predicted by calculations from TDDFT. By using femtosecond EUV probe pulses for the photoemission study, the measurement of events in the far-from-equilibrium state would be feasible even for high binding energies and with high energy resolution. In the time-resolved momentum microscopy setup in our group, the energy resolution is mainly determined by the bandwidth of the HHG and was estimated to $\approx 200\,\text{meV}$ [167]. A spin filter is already implemented in the setup, which therefore provides the capability for a more detailed study of (spin-conserving) excitation pathways around E_F, as has already been shown by Eich et al. and Gort et al. [67, 70, 165]. In addition, spin-resolved photoemission could be used to further investigate the microscopic processes that lead to the ultrafast demagnetization of the $3d$ FM. As discussed by Eich et al., band-mirroring

and collapse of exchange splitting renormalize the band structure in different ways and can therefore be identified by photoemission [70, 168].

Another exciting opportunity for future research lies in the investigation of magnetization processes on longer timescales, which has not been treated within the scope of this thesis. As we have briefly introduced in Chapter 4.2.2, distinct dynamics of the energy-resolved T-MOKE asymmetry of Ni can also be observed when the magnetization recovers. Similar observations have also been made for Co and Fe. Thus, a next step is to extend our analysis of the ϵ_{xy}-extraction to longer time scales to uncover the cause of these distinct dynamics, which in principle can initially be presumed to be caused by band-renormalization effects.

Appendix for Chapter 4

A

A.1. Determination of the angle scan range

To determine the total angle scan range achievable with the UHV compatible tip-tilt sample holder, we used a camera to record the position of the back-reflection of an alignment laser from the sample surface on a screen (see Figure 4.3). Figure A.1 shows the tracked beam for consecutive measurements of the static asymmetry of Ni for different incidence angles θ_i. The corresponding data is shown in Figure 5.5 in Chapter 5. As the angle of incidence changes, the beam travels on the screen. Taking the center of mass (red dots) of the laser spot allows us to accurately record the movement of the beam. From the pixel size, the total beam displacement for the angle scan range can be calculated from the movement in x- and y-direction to $d \approx 12\,\text{mm}$ (the first 4 angles are omitted, see Figure A.2). This distance yields an angle range of 1.7°, which corresponds to a change of $\approx 0.2°$ in between two consecutive measurements (distance sample to screen: 40.5 cm). A total scan range of 2.5° in our experiment was determined as described above for the static measurement of 13 different angles of incidence for the measurement of $\text{Fe}_{19}\text{Ni}_{81}$. The corresponding data is shown in Ref. [85].
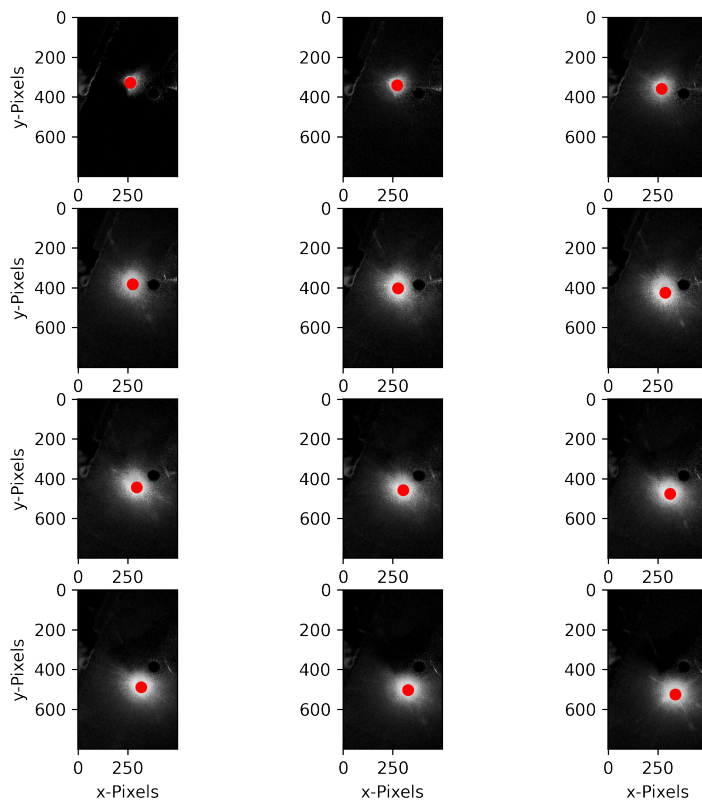
Figure A.1. – Reflected beam of the alignment laser from the sample for different angles of incidence. The beam was tracked by taking the center of mass (red dots) of the laser spot. As the angle of incidence changes, the beam travels on the screen. This displacement is tracked for the full angle scan range.
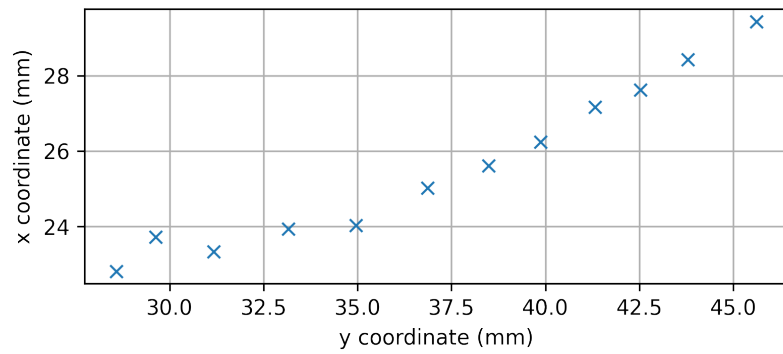
Figure A.2. – Pixel coordinates of the center of mass as indicated in Figure A.1 for all incidence angles. The plot reveals a displacement of the reflected beam from the sample on a straight line. The first 4 points (4 angles) should be ignored, as the reflected beam was clipped for these measurements.

Appendix for Chapter 5

B.1. Supplemental material

I. Experimental setup and analysis details

The experimental setup used for the determination of the time-resolved dielectric tensor is based on the EUV T-MOKE setup that was described in Ref. [115]. We pumped the samples with a 47 ± 5 fs pulse (Gauss FWHM) with a photon energy of 1.2 eV. The absorbed fluence for the measurements was 0.8 ± 0.2 mJ/cm². The reflected 100 kHz EUV probe beam spans energies between $30-72$ eV. For the data acquisition at different angles
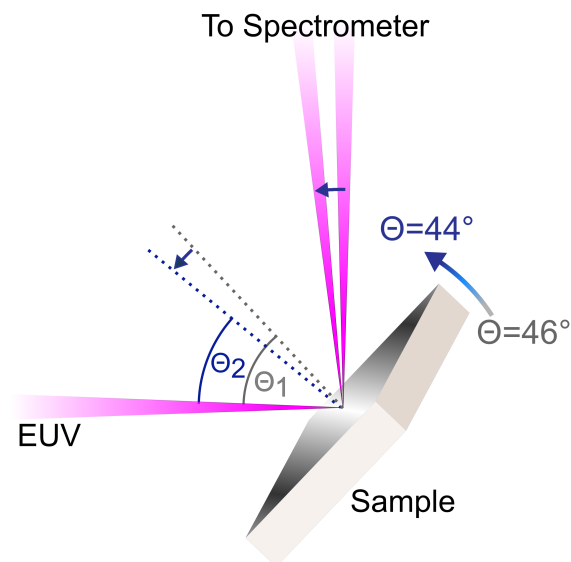
Figure B.1. – Schematic of the T-MOKE experiment. A small, non-magnetic tip-tilt holder enables repeatable control of the incidence angle in a range of 2.5° around 45°.

of incidence (see Figure B.1), an accurate and repeatable control of the incidence angle

was ensured by mounting the sample on a small non-magnetic, UHV-compatible tip-tilt stage (SmarAct GmbH, STT-12.7-UHVT-NM, Figure B.1).
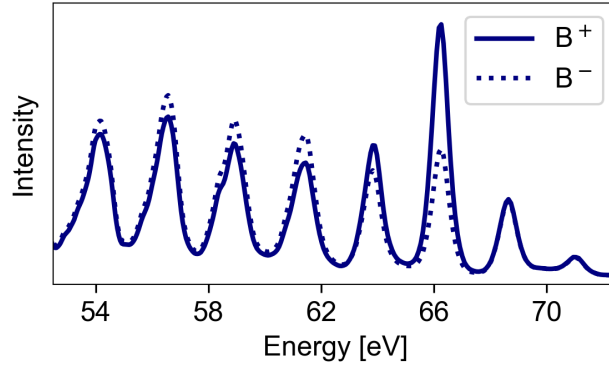
Figure B.2. – Typical high-harmonic spectrum after the reflection from the Ni thin film for opposite magnetization directions. The discrete nature of the spectrum of odd harmonics of the fundamental beam is clearly visible. The magneto optical response is largest around the Ni resonance at ≈ 66 eV, which is visible by the large difference in intensity for opposite magnetization directions.

After reflection from the sample, the EUV light is analyzed in the EUV spectrometer. A typical spectrum is shown in Figure B.2. The energy axis of our spectrometer is determined from the spacing of the high harmonics, which is given by twice the fundamental photon energy of 1.2 eV. This leads to a relative uncertainty of $< 2\%$ on the photon energy calibration. From the energy-resolved dynamics, we estimate the spectral resolution to be better than 0.2 eV.

For the determination of the off-diagonal dielectric tensor ϵ_{xy} from T-MOKE data, the asymmetry was evaluated in 0.1 eV energy windows separated by 0.3 eV (center-to-center) at energies close to the high harmonic maxima. Fit results of the static magnetic asymmetries for the extraction of ϵ_{xy} (Section 5.3.1) together with the observed T-MOKE asymmetry are shown in Figure B.3 and yield good agreement with the measured static T-MOKE asymmetries. We note that the T-MOKE asymmetry is strongly reduced in-between high harmonic energies due to the comparably higher background contribution at those energies.

The transient evolution of the off-diagonal dielectric tensor ϵ_{xy} was determined from the measured reflectivities $R_{\uparrow/\downarrow}$ (Section 5.3.3). For the fitting of $R_{\uparrow/\downarrow}$, good agreement with the experimental data on early timescales can only be achieved by the inclusion of transient optical changes of the complex refractive index $n = 1 - \delta + i\beta$. In particular, this is important below the resonance (around ≈ 64 eV), where we probe states below E_{F}, which are most strongly affected by the excitation of electrons by the pump pulse. Not including
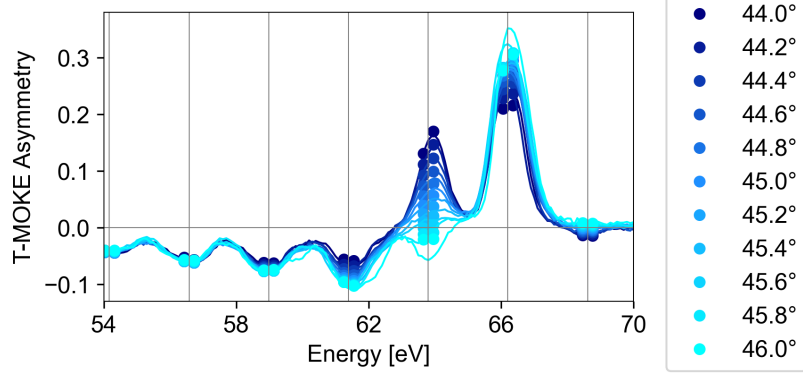
Figure B.3. – Fit of the static magnetic asymmetries for the extraction of ϵ_{xy} as described in Section 5.3.1. The results from the fit procedure (colored circles) provide a satisfactory description of the experimental data (solid lines).

the refractive index changes yields a poor agreement between the measured $R_{\uparrow/\downarrow}$ and the fit, as shown in Figure B.4. The extracted transient evolution of the real and imaginary part of the off-diagonal dielectric tensor element ϵ_{xy} and the optical changes of δ and β for selected energies around the Ni resonance are shown in Figure B.5.
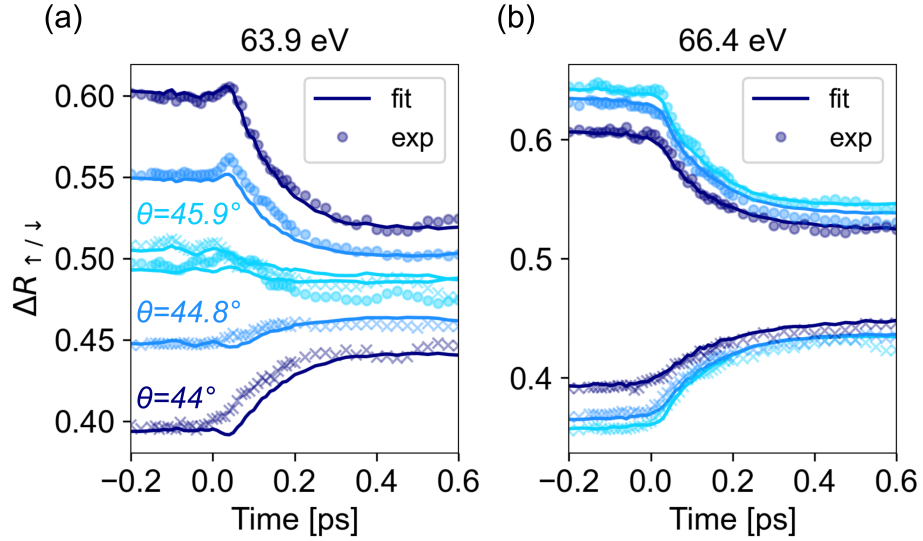
Figure B.4. – Time-resolved analysis of the dielectric tensor, if transient changes of the refractive index in the sample are neglected. The panels show the measured (points) and reconstructed (line) transient relative reflectivity $\Delta R_{\uparrow/\downarrow}(t)$ for opposite magnetization directions (cf. Equation 5.7 in the main text) during optically-induced demagnetization for photon energies just below (a) and close to (b) the Ni M-edge – equivalent to Figure 5.6 (a) and (b) in the main text. The exclusion of transient optical changes of the refractive index results in a poor fit of the experimental data, especially at the energy below the resonance, where the $\Delta R_{\uparrow/\downarrow}(t)$ curves deviate from the usual mirror-symmetric behavior. At this energy, the excitation of electrons by the laser pulse is most dominant and has a strong effect on the refractive index.
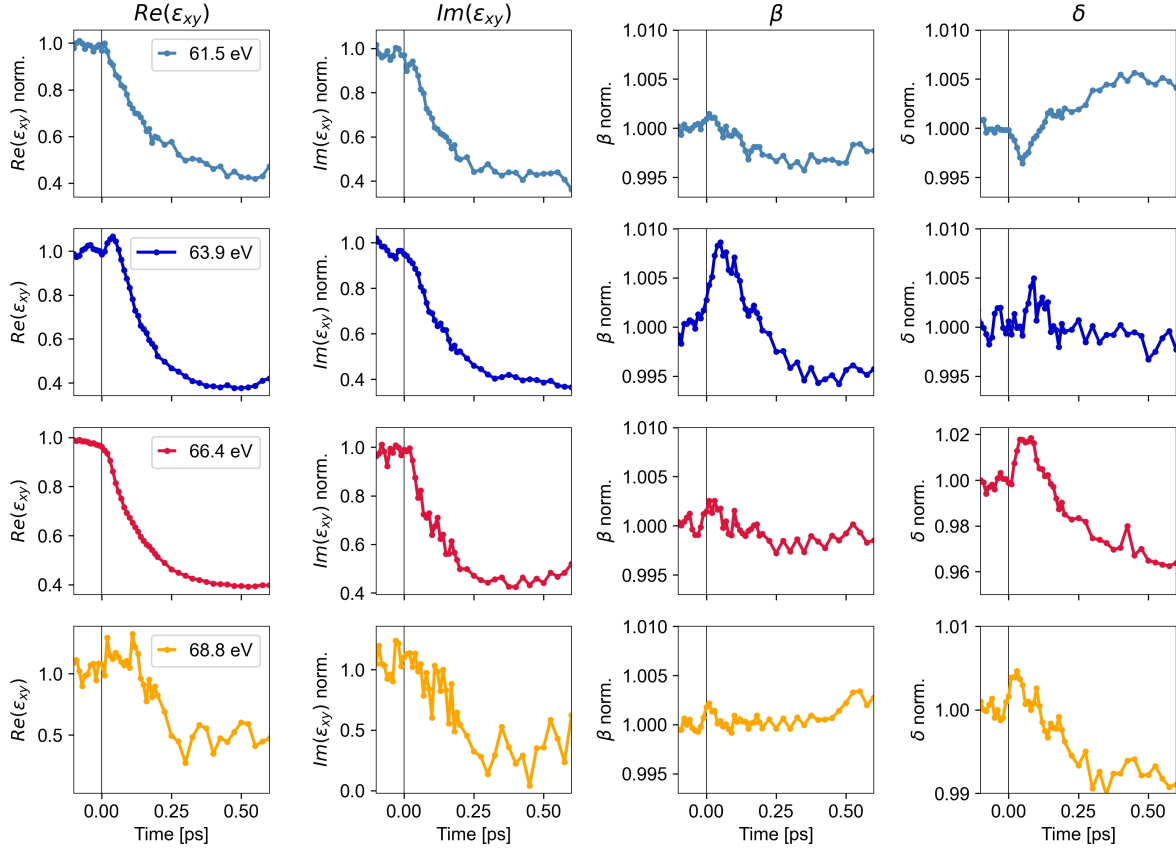
Figure B.5. – Fit results of the transient behavior of ϵ_{xy} and n for different energies around the Ni M-edge.

II. Time-dependent Density Functional Theory

For the TDDFT calculations a pump pulse with a central photon energy of 1.2 eV, a Gaussian intensity profile with FWHM = 47 fs and an incident fluence of ≈ 18 mJ/cm² was used. For the details of the method and the code, see Refs. [20, 156, 162].

B.2. Details of FeNi data

For the measurements of $Fe_{50}Ni_{50}$, $Fe_{19}Ni_{81}$ and Ni, the samples were pumped with a 47 ± 5 fs pulses (Gauss FWHM) with a photon energy of 1.2 eV. The absorbed fluence is slightly different for each measurement: 0.8 ± 0.2 mJ/cm² for Ni, 1.1 ± 0.2 mJ/cm² for $Fe_{50}Ni_{50}$ and 0.8 ± 0.2 mJ/cm² for $Fe_{19}Ni_{81}$.

For the TDDFT calculations, the pump pulse energy (1.2 eV) and pulse duration (47 fs) were adapted to the parameters used in experiment. The fluence was 18 mJ/cm².

Appendix for Chapter 6

C.1. Sample information and characterization

All samples from Chapter 6 (see Table C.1) were provided by THOMAS BREDE and MICHEL KUHFUSS from the Institute of Materials Physics, University of Göttingen and were obtained by Ar ion beam sputtering using a Kaufman source. The thicknesses were determined by X-ray reflectometry measurements. X-ray diffraction (XRD) measurements of the three samples are shown in Figure C.1.

Table C.1. – Sample information for the Ni, Co, and Fe thin films.

	Substrate	Thickness [nm]
Ni	$Si_3N_4/Si(100)$	21
Co	MgO(100)	44
Fe	MgO(100)	23

The samples exhibit an in-plane magnetization with a coercive field of less than $10\,\text{mT}$, as determined by the hysteresis measurements shown in Figure C.2. The measurements were performed by TIM TITZE with a visible MOKE setup in longitudinal geometry.
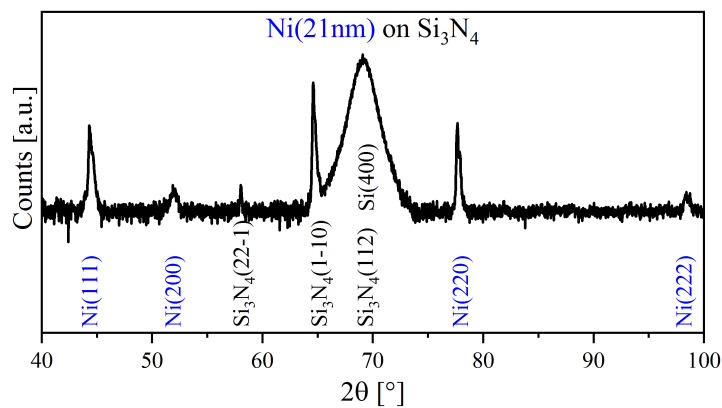
(a)
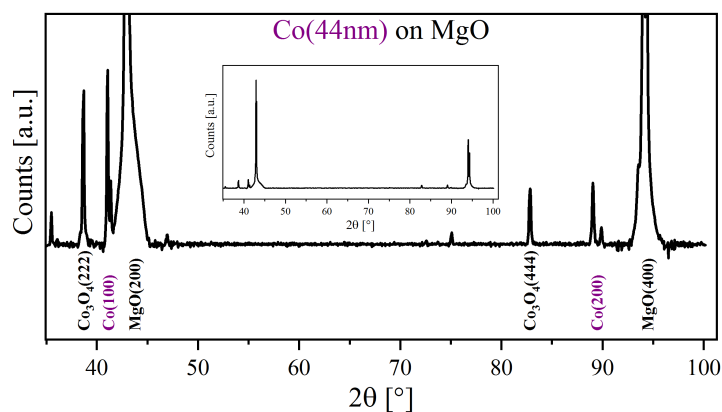
(b)
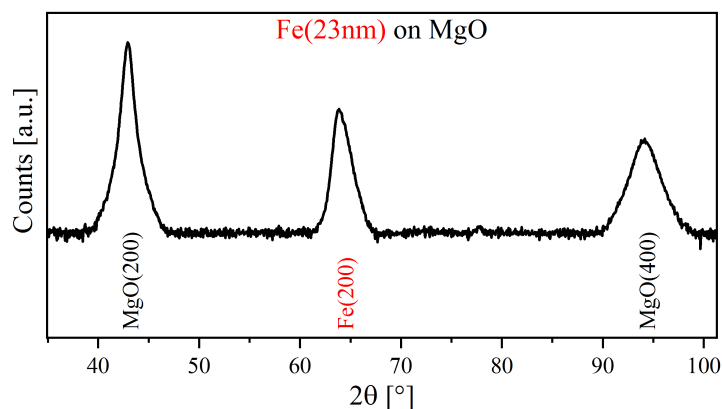
(c)

Figure C.1. – XRD measurements of (a) Ni, (b) Co, and (c) Fe. (a) Grazing incidence θ-2θ XRD reveals a bulk-like texture of the Ni film. (b) XRD measurement shows pure and oxidized phases of Co as well as non-identified peaks at $35.501°$, $46.981°$, and $75.103°$ which indicate a higher amount of impurities. The inset shows the non-zoomed XRD measurement. (c) Grazing incidence θ-2θ XRD reveals a strong (100) out-of-plane texture of the Fe film.

(a)

(b)

(c)
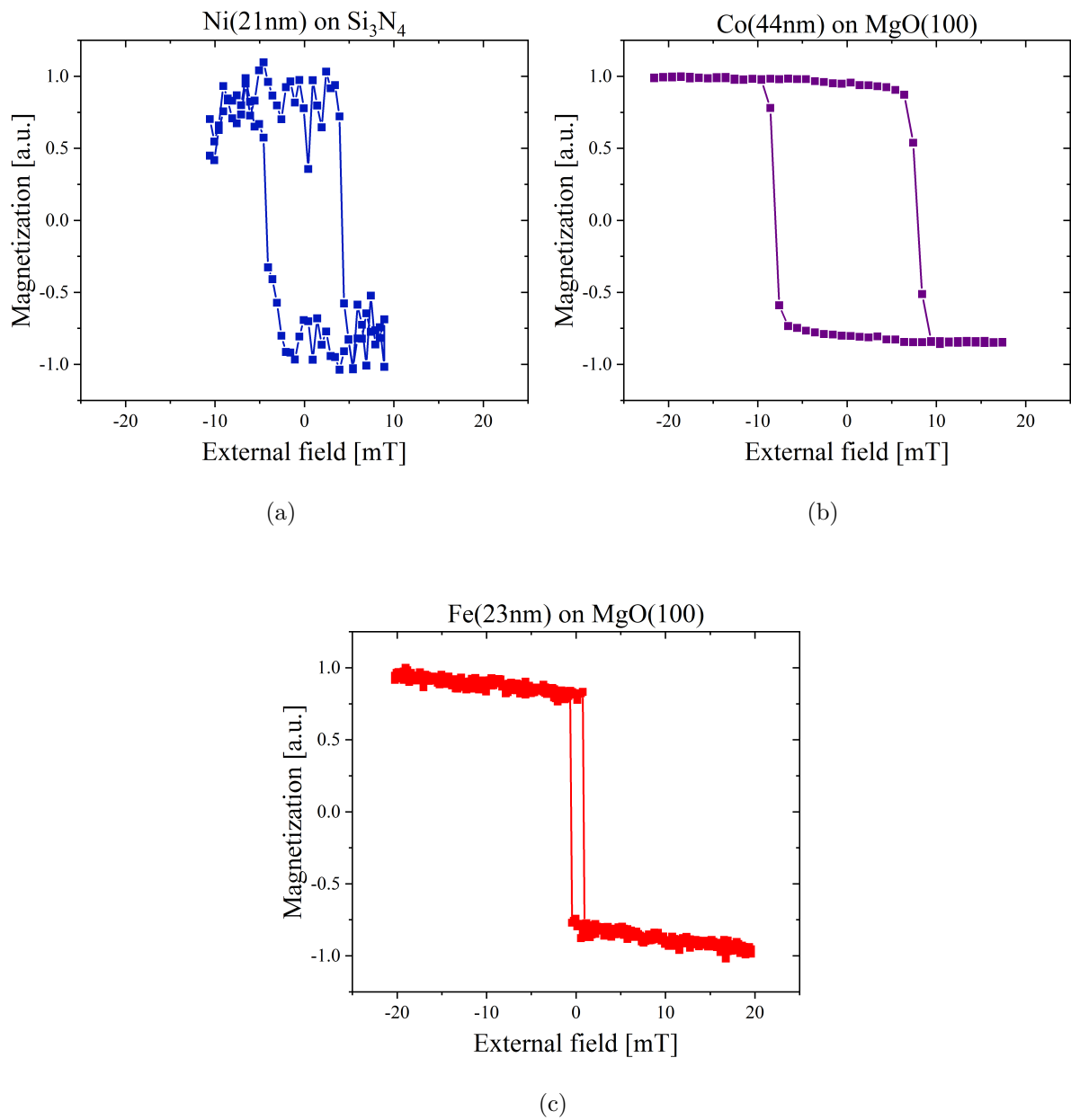
Figure C.2. – Hysteresis measurements of (a) Ni, (b) Co, and (c) Fe.

C.2. Supplementary information - Combining experiment and theory

Similar to the measurement of Fe, transient changes of the magnetic asymmetry for energies several electronvolts above the resonance can also be found for Co. However, here we find a rather homogeneous behavior of the magnetic asymmetry traces, as shown in Figure C.3
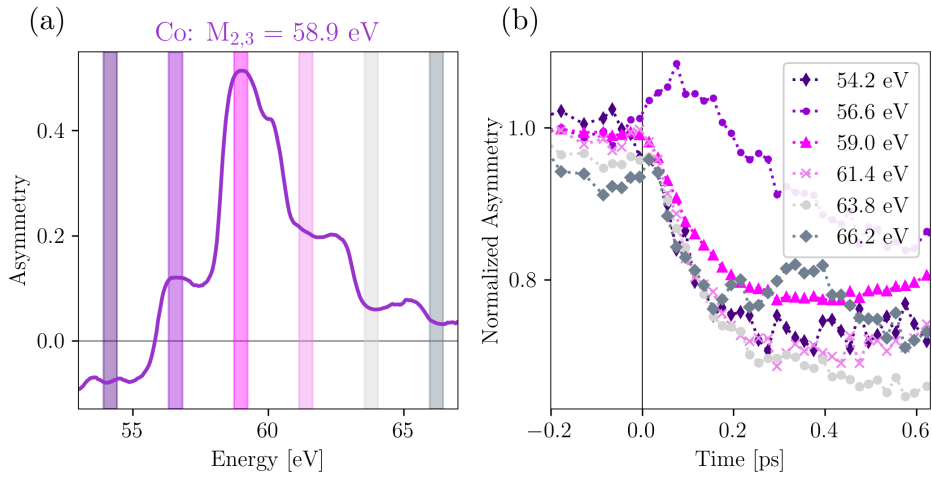
Figure C.3. – (a) Static magnetic asymmetry of Co. The indicated 0.5 eV intervals correspond to the evaluated areas in the asymmetry for the time-resolved analysis. (b) The transient magnetic asymmetry of Co for energies spanning several electronvolts below and above the resonance. Omitting the harmonic energy of 56.6 eV, all other energies show a rather homogeneous behavior of the transient magnetic asymmetry.

Bibliography

[1] Michael Faraday. On the magnetization of light and the illumination of magnetic lines of force. *Philosophical Transactions of the Royal Society of London*, 136:1–20, 1846.

[2] John Kerr. XLIII. On rotation of the plane of polarization by reflection from the pole of a magnet. *The London, Edinburgh, and Dublin Philosophical Magazine and Journal of Science*, 3(19):321–343, 1877.

[3] J. C. Maxwell. *A Treatise on Electricity and Magnetism*. Clarendon Press, 1873.

[4] H. A. Lorentz. *Versuch einer Theorie der electrischen und optischen Erscheinungen in bewegten Körpern*. E. J. Brill, Leiden, 1895.

[5] P. Drude. Zur Elektronentheorie der Metalle; II. Teil. Galvanomagnetische und thermomagnetische Effecte. *Annalen der Physik*, 308(11):369–402, 1900.

[6] A. Kimel, A. Zvezdin, S. Sharma, et al. The 2022 magneto-optics roadmap. *Journal of Physics D: Applied Physics*, 55(46):463003, 2022.

[7] O. N. Tufte and D. Chen. Optical techniques for data storage. *IEEE Spectrum*, 10(2):26–32, 1973.

[8] Di Chen and J. D. Zook. An overview of optical data storage technology. *Proceedings of the IEEE*, 63(8):1207–1230, 1975.

[9] M. Takahashi, H. Shoji, Y. Hozumi, and T. Wakiyama. Giant magnetic Kerr rotation for Pt substituted MnSb compound films with NiAs type structure. *Journal of Magnetism and Magnetic Materials*, 131(1-2):67–75, 1994.

[10] M. Mansuripur. *The physical principles of magneto-optical recording*. Cambridge University Press, Cambridge, 1995.

[11] E. Beaurepaire, J. Merle, A. Daunois, and J. Bigot. Ultrafast spin dynamics in ferromagnetic nickel. *Physical Review Letters*, 76(22):4250–4253, 1996.

[12] F. Siegrist, J. A. Gessner, M. Ossiander, et al. Light-wave dynamic control of magnetism. *Nature*, 571(7764):240–244, 2019.

[13] C. D. Stanciu, F. Hansteen, A. V. Kimel, et al. All-optical magnetic recording with circularly polarized light. *Physical Review Letters*, 99(4):047601, 2007.

[14] I. Radu, K. Vahaplar, C. Stamm, et al. Transient ferromagnetic-like state mediating ultrafast reversal of antiferromagnetically coupled spins. *Nature*, 472(7342):205–208, 2011.

[15] G. Ju, J. Hohlfeld, B. Bergman, et al. Ultrafast generation of ferromagnetic order via a laser-induced phase transformation in FeRh thin films. *Physical Review Letters*, 93(19):197403, 2004.

[16] T. Kampfrath, A. Sell, G. Klatt, et al. Coherent terahertz control of antiferromagnetic spin waves. *Nature Photonics*, 5(1):31–34, 2011.

[17] A. Kirilyuk, A. V. Kimel, and T. Rasing. Ultrafast optical manipulation of magnetic order. *Reviews of Modern Physics*, 82(3):2731–2784, 2010.

[18] J.-Y. Bigot and M. Vomir. Ultrafast magnetization dynamics of nanostructures. *Annalen der Physik*, 525(1-2):2–30, 2013.

[19] J.-Y. Bigot, M. Vomir, and E. Beaurepaire. Coherent ultrafast magnetism induced by femtosecond laser pulses. *Nature Physics*, 5(7):515–520, 2009.

[20] K. Krieger, J. K. Dewhurst, P. Elliott, S. Sharma, and E. K. U. Gross. Laser-induced demagnetization at ultrashort time scales: Predictions of TDDFT. *Journal of chemical theory and computation*, 11(10):4870–4874, 2015.

[21] M. Hofherr, S. Häuser, J. K. Dewhurst, et al. Ultrafast optically induced spin transfer in ferromagnetic alloys. *Science Advances*, 6(3):eaay8717, 2020.

[22] P. Tengdin, C. Gentry, A. Blonsky, et al. Direct light-induced spin transfer between different elements in a spintronic Heusler material via femtosecond laser excitation. *Science Advances*, 6(3):eaaz1100, 2020.

[23] D. Steil, J. Walowski, F. Gerhard, et al. Efficiency of ultrafast optically induced spin transfer in Heusler compounds. *Physical Review Research*, 2(2), 2020.

[24] F. Willems, S. Sharma, C. V Korff Schmising, et al. Magneto-Optical Functions at the 3p Resonances of Fe, Co, and Ni: Ab initio Description and Experiment. *Physical Review Letters*, 122(21):217202, 2019.

[25] S. A. Ryan, P. C. Johnsen, M. F. Elhanoty, et al. Optically controlling the competition between spin flips and intersite spin transfer in a Heusler half-metal on sub-100 fs timescales. arXiv:2305.16455 [cond-mat.mtrl-sci], 2023.

[26] C. Möller, H. Probst, G. S. M. Jansen, et al. Verification of ultrafast spin transfer effects in FeNi alloys. arXiv:2306.02793 [cond-mat.mtrl-sci], 2023.

[27] D. Attwood. *Soft X-Rays and Extreme Ultraviolet Radiation: Principles and Applications.* Cambridge university press, 2000.

[28] S. Jana, R. S. Malik, Y. O. Kvashnin, et al. Analysis of the linear relationship between asymmetry and magnetic moment at the M edge of 3d transition metals. *Physical Review Research*, 2(1):013180, 2020.

[29] K. Yao, F. Willems, C. von Korff Schmising, et al. Distinct spectral response in M -edge magnetic circular dichroism. *Physical Review B*, 102(10):100405, 2020.

[30] M. Hennes, B. Rösner, V. Chardonnet, et al. Time-Resolved XUV Absorption Spectroscopy and Magnetic Circular Dichroism at the Ni $M_{2,3}$-Edges. *Applied Sciences*, 11(1):325, 2021.

[31] B. Koopmans, M. van Kampen, J. T. Kohlhepp, and W. J. de Jonge. Ultrafast magneto-optics in nickel: magnetism or optics? *Physical Review Letters*, 85(4):844–847, 2000.

[32] L. Guidoni, E. Beaurepaire, and J.-Y. Bigot. Magneto-optics in the ultrafast regime: thermalization of spin populations in ferromagnetic films. *Physical Review Letters*, 89(1):017401, 2002.

[33] J.-Y. Bigot, L. Guidoni, E. Beaurepaire, and P. N. Saeta. Femtosecond spectrotemporal magneto-optics. *Physical Review Letters*, 93(7):077401, 2004.

[34] P. M. Oppeneer and A. Liebsch. Ultrafast demagnetization in Ni: theory of magneto-optics for non-equilibrium electron distributions. *Journal of Physics: Condensed Matter*, 16(30):5519–5530, 2004.

[35] K. Carva, D. Legut, and P. M. Oppeneer. Influence of laser-excited electron distributions on the X-ray magnetic circular dichroism spectra: Implications for femtosecond demagnetization in Ni. *EPL (Europhysics Letters)*, 86(5):57002, 2009.

[36] K. Carva, M. Battiato, and P. M. Oppeneer. Is the controversy over femtosecond magneto-optics really solved? *Nature Physics*, 7(9):665, 2011.

[37] C. La-O-Vorakiat, E. Turgut, C. A. Teale, et al. Ultrafast Demagnetization Measurements Using Extreme Ultraviolet Light: Comparison of Electronic and Magnetic Contributions. *Physical Review X*, 2(1), 2012.

[38] B. Vodungbo, J. Gautier, G. Lambert, P. Zeitoun, and J. Lüning. Comment on "Ultrafast Demagnetization Measurements Using Extreme Ultraviolet Light: Comparison of Electronic and Magnetic Contributions". *Physical Review X*, 3(3), 2013.

[39] E. Turgut, P. Grychtol, C. La-O-Vorakiat, et al. Reply to "Comment on 'Ultrafast Demagnetization Measurements Using Extreme Ultraviolet Light: Comparison of Electronic and Magnetic Contributions' ". *Physical Review X*, 3(3), 2013.

[40] J. Stöhr and H. C. Siegmann. *Magnetism: From Fundamentals to Nanoscale Dynamics*, volume 152 of *Springer Series in Solid-State Sciences*. Springer-Verlag Berlin Heidelberg, Berlin, Heidelberg, 2006.

[41] J. M. D. Coey. *Magnetism and Magnetic Materials*. Cambridge University Press, 2009.

[42] W. Heisenberg. Zur Theorie des Ferromagnetismus. *Zeitschrift fur Physik*, 49:619–636, 1928.

[43] E. C. Stoner. Collective electron specific heat and spin paramagnetism in metals. *Proceedings of the Royal Society of London. Series A-Mathematical and Physical Sciences*, 154(883):656–678, 1936.

[44] E. C. Stoner. Collective electron ferromagnetism. *Proceedings of the Royal Society of London. Series A. Mathematical and Physical Sciences*, 165(922):372–414, 1938.

[45] N. Mott. A discussion of the transition metals on the basis of quantum mechanics. *Proceedings of the Physical Society*, 47(4):571, 1935.

[46] J. C. Slater. The ferromagnetism of nickel. *Physical Review*, 49(7):537, 1936.

[47] J. C. Slater. The ferromagnetism of nickel. II. Temperature effects. *Physical Review*, 49(12):931, 1936.

[48] M. Plötzing. Ultrafast Demagnetization Dynamics in Ni_xPd_{1-x} alloys. Master's thesis, Forschungszentrum Jülich GmbH, 2011.

[49] O. Eriksson, M. S. Brooks, and B. Johansson. Orbital polarization in narrow-band systems: Application to volume collapses in light lanthanides. *Physical Review B*, 41(10):7311–7314, 1990.

[50] O. Eriksson, B. Johansson, R. C. Albers, Boring, and M. S. Brooks. Orbital magnetism in Fe, Co, and Ni. *Physical Review B*, 42(4):2707–2710, 1990.

[51] G. M. Müller, J. Walowski, M. Djordjevic, et al. Spin polarization in half-metals probed by femtosecond spin excitation. *Nature Materials*, 8(1):56–61, 2009.

[52] M. Fähnle and C. Illg. Electron theory of fast and ultrafast dissipative magnetization dynamics. *Journal of Physics: Condensed matter*, 23(49):493201, 2011.

[53] R. J. Elliott. Theory of the Effect of Spin-Orbit Coupling on Magnetic Resonance in Some Semiconductors. *Physical Review*, 96(2):266–279, 1954.

[54] Y. Yafet. g Factors and Spin-Lattice Relaxation of Conduction Electrons. *Solid State Physics*, 14:1–98, 1963.

[55] K. Carva, P. Baláž, and I. Radu. Laser-Induced Ultrafast Magnetic Phenomena. *Handbook of Magnetic Materials*, 26:291–463, 2017.

[56] B. Koopmans, H. Kicken, M. van Kampen, and W. de Jonge. Microscopic model for femtosecond magnetization dynamics. *Journal of Magnetism and Magnetic Materials*, 286:271–275, 2005.

[57] K. Carva, M. Battiato, and P. M. Oppeneer. Ab Initio investigation of the Elliott-Yafet electron-phonon mechanism in laser-induced ultrafast demagnetization. *Physical Review Letters*, 107(20):207201, 2011.

[58] K. Carva, M. Battiato, D. Legut, and P. M. Oppeneer. Ab initio theory of electron-phonon mediated ultrafast spin relaxation of laser-excited hot electrons in transition-metal ferromagnets. *Physical Review B*, 87(18), 2013.

[59] C. Illg, M. Haag, and M. Fähnle. Ultrafast demagnetization after laser irradiation in transition metals: Ab initio calculations of the spin-flip electron-phonon scattering with reduced exchange splitting. *Physical Review B*, 88(21), 2013.

[60] M. Krauß, T. Roth, S. Alebrand, et al. Ultrafast demagnetization of ferromagnetic transition metals: The role of the Coulomb interaction. *Physical Review B*, 80(18), 2009.

[61] B. Y. Mueller, T. Roth, M. Cinchetti, M. Aeschlimann, and B. Rethfeld. Driving force of ultrafast magnetization dynamics. *New Journal of Physics*, 13(12):123010, 2011.

[62] E. Carpene, E. Mancini, C. Dallera, et al. Dynamics of electron-magnon interaction and ultrafast demagnetization in thin iron films. *Physical Review B*, 78(17), 2008.

[63] A. B. Schmidt, M. Pickel, M. Donath, et al. Ultrafast magnon generation in an Fe film on Cu(100). *Physical Review Letters*, 105(19):197401, 2010.

[64] B. Andres, M. Christ, C. Gahl, et al. Separating Exchange Splitting from Spin Mixing in Gadolinium by Femtosecond Laser Excitation. *Physical Review Letters*, 115(20):207404, 2015.

[65] E. Carpene, H. Hedayat, F. Boschini, and C. Dallera. Ultrafast demagnetization of metals: Collapsed exchange versus collective excitations. *Physical Review B*, 91(17), 2015.

[66] H.-S. Rhie, H. A. Dürr, and W. Eberhardt. Femtosecond electron and spin dynamics in Ni/W(110) films. *Physical Review Letters*, 90(24):247201, 2003.

[67] R. Gort, K. Bühlmann, S. Däster, et al. Early Stages of Ultrafast Spin Dynamics in a 3d Ferromagnet. *Physical Review Letters*, 121(8):087206, 2018.

[68] D. Zusin, P. M. Tengdin, M. Gopalakrishnan, et al. Direct measurement of the static and transient magneto-optical permittivity of cobalt across the entire M-edge in reflection geometry by use of polarization scanning. *Physical Review B*, 97(2):024433, 2018.

[69] P. Tengdin, W. You, C. Chen, et al. Critical behavior within 20 fs drives the out-of-equilibrium laser-induced magnetic phase transition in nickel. *Science Advances*, 4(3):eaap9744, 2018.

[70] S. Eich, M. Plötzing, M. Rollinger, et al. Band structure evolution during the ultrafast ferromagnetic-paramagnetic phase transition in cobalt. *Science Advances*, 3(3):e1602094, 2017.

[71] E. Turgut, D. Zusin, D. Legut, et al. Stoner versus Heisenberg: Ultrafast exchange reduction and magnon generation during laser-induced demagnetization. *Physical Review B*, 94(22):220408, 2016.

[72] M. Battiato, K. Carva, and P. M. Oppeneer. Superdiffusive spin transport as a mechanism of ultrafast demagnetization. *Physical Review Letters*, 105(2):027203, 2010.

[73] G. Malinowski, F. Dalla Longa, J. H. H. Rietjens, et al. Control of speed and efficiency of ultrafast demagnetization by direct transfer of spin angular momentum. *Nature Physics*, 4(11):855–858, 2008.

[74] D. Rudolf, C. La-O-Vorakiat, M. Battiato, et al. Ultrafast magnetization enhancement in metallic multilayers driven by superdiffusive spin current. *Nature Communications*, 3(1):1037, 2012.

[75] A. Melnikov, I. Razdolski, T. O. Wehling, et al. Ultrafast transport of laser-excited spin-polarized carriers in Au/Fe/MgO(001). *Physical Review Letters*, 107(7):076601, 2011.

[76] A. Eschenlohr, M. Battiato, P. Maldonado, et al. Ultrafast spin transport as key to femtosecond demagnetization. *Nature Materials*, 12(4):332–336, 2013.

[77] M. Battiato and K. Held. Ultrafast and Gigantic Spin Injection in Semiconductors. *Physical Review Letters*, 116(19):196601, 2016.

[78] E. Turgut, C. La-O-Vorakiat, J. M. Shaw, et al. Controlling the competition between optically induced ultrafast spin-flip scattering and spin transport in magnetic multilayers. *Physical Review Letters*, 110(19):197201, 2013.

[79] M. Hofherr, P. Maldonado, O. Schmitt, et al. Speed and efficiency of femtosecond spin current injection into a nonmagnetic material. *Physical Review B*, 96(10), 2017.

[80] M. Aeschlimann, M. Bauer, S. Pawlik, et al. Ultrafast Spin-Dependent Electron Dynamics in fcc Co. *Physical Review Letters*, 79(25):5158–5161, 1997.

[81] R. Knorren, K. H. Bennemann, R. Burgermeister, and M. Aeschlimann. Dynamics of excited electrons in copper and ferromagnetic transition metals: Theory and experiment. *Physical Review B*, 61(14):9427–9440, 2000.

[82] V. P. Zhukov, E. V. Chulkov, and P. M. Echenique. Lifetimes and inelastic mean free path of low-energy excited electrons in Fe, Ni, Pt, and Au: Ab initio GW+T calculations. *Physical Review B*, 73(12), 2006.

[83] A. J. Schellekens, W. Verhoeven, T. N. Vader, and B. Koopmans. Investigating the contribution of superdiffusive transport to ultrafast demagnetization of ferromagnetic thin films. *Applied Physics Letters*, 102(25):252408, 2013.

[84] P. Elliott, T. Müller, J. K. Dewhurst, S. Sharma, and E. K. U. Gross. Ultrafast laser induced local magnetization dynamics in Heusler compounds. *Scientific Reports*, 6(1):38911, 2016.

[85] C. Möller. *Ultrafast spin dynamics in FeNi alloys.* Phd thesis, University of Göttingen, 2023.

[86] C. Stamm, T. Kachel, N. Pontius, et al. Femtosecond modification of electron localization and transfer of angular momentum in nickel. *Nature Materials*, 6(10):740–743, 2007.

[87] T. Kachel, N. Pontius, C. Stamm, et al. Transient electronic and magnetic structures of nickel heated by ultrafast laser pulses. *Physical Review B*, 80(9):092404, 2009.

[88] C. Boeglin, E. Beaurepaire, V. Halté, et al. Distinguishing the ultrafast dynamics of spin and orbital moments in solids. *Nature*, 465(7297):458–461, 2010.

[89] J. L. Erskine and E. A. Stern. Calculation of the $M_{2,3}$ magneto-optical absorption spectrum of ferromagnetic nickel. *Physical Review B*, 12(11):5016–5024, 1975.

[90] B. Rösner, B. Vodungbo, V. Chardonnet, et al. Simultaneous two-color snapshot view on ultrafast charge and spin dynamics in a Fe-Cu-Ni tri-layer. *Structural Dynamics*, 7(5):054302, 2020.

[91] P. M. Oppeneer. Chapter 3 Magneto-optical Kerr spectra. In K. H. J. Buschow, editor, *Handbook of magnetic materials*, volume 13 of *Handbook of Magnetic Materials*, pages 229–422. North-Holland, Amsterdam, 2001.

[92] S. Sugano and N. Kojima, editors. *Magneto-optics*, volume 128 of *Springer series in solid-state sciences*. Springer, Berlin, Heidelberg, Germany, 2000.

[93] H.-C. Mertins, S. Valencia, A. Gaupp, et al. Magneto-optical polarization spectroscopy with soft X-rays. *Applied Physics A*, 80(5):1011–1020, 2005.

[94] P. Bruno, Y. Suzuki, and C. Chappert. Magneto-optical Kerr effect in a paramagnetic overlayer on a ferromagnetic substrate: A spin-polarized quantum size effect. *Physical Review B*, 53(14):9214–9220, 1996.

[95] E. Beaurepaire. *Magnetism*, volume v.697 of *Lecture Notes in Physics Ser.* Springer Berlin / Heidelberg, Berlin, Heidelberg, 2006.

[96] R. P. Hunt. Magneto–Optic Scattering from Thin Solid Films. *Journal of Applied Physics*, 38(4):1652–1671, 1967.

[97] Boswarva, Ian Melvyn and Howard, RE and Lidiard, AB. Faraday effect in semiconductors. *Proceedings of the Royal Society of London. Series A. Mathematical and Physical Sciences*, 269(1336):125–141, 1962.

[98] C.-Y. You and S.-C. Shin. Derivation of simplified analytic formulae for magneto–optical Kerr effects. *Applied Physics Letters*, 69(9):1315–1317, 1996.

[99] A. Yaresko, A. Perlov, V. Antonov, and B. Harmon. Band-Structure Theory of Dichroism. In *Magnetism: A Synchrotron Radiation Approach*, pages 121–141. Springer, Berlin, Heidelberg, 2006.

[100] C. La-O-Vorakiat. *Element-Selective Ultrafast Magnetization Dynamics with a Tabletop Light Source.* Phd thesis, University of Colorado, 2011.

[101] S. Mathias, C. La-O-Vorakiat, P. Grychtol, et al. Probing the timescale of the exchange interaction in a ferromagnetic alloy. *Proceedings of the National Academy of Sciences of the United States of America*, 109(13):4792–4797, 2012.

[102] M. Hennecke, D. Schick, T. Sidiropoulos, et al. Ultrafast element- and depth-resolved magnetization dynamics probed by transverse magneto-optical Kerr effect spectroscopy in the soft x-ray range. *Physical Review Research*, 4(2), 2022.

[103] B. L. Henke, E. M. Gullikson, and J. C. Davis. X-Ray Interactions: Photoabsorption, Scattering, Transmission, and Reflection at $E = 50 - 30,000\,\mathrm{eV}$, $Z = 1 - 92$. *Atomic Data and Nuclear Data Tables*, 54(2):181–342, 1993.

[104] E. Tamura, G. D. Waddill, J. G. Tobin, and P. A. Sterne. Linear and Circular Dichroism in Angle Resolved Fe 3 p Photoemission. *MRS Proceedings*, 375, 1994.

[105] J. G. Tobin, K. W. Goodman, F. O. Schumann, et al. Direct extraction of exchange splittings from magnetic X-ray dichroism in photoelectron spectroscopy. *Surface Science*, 395(2-3):L227–L235, 1998.

[106] J. G. Tobin and F. O. Schumann. Element-specific magnetometry with photoelectron dichroism: FeCo and FeNi. *Surface Science*, 478(3):211–228, 2001.

[107] F. U. Hillebrecht, C. Roth, H. B. Rose, M. Finazzi, and L. Braicovich. Circular magnetic dichroism in spin-resolved Fe 3p photoemission. *Physical Review B*, 51(14):9333–9336, 1995.

[108] C. T. Chen, Y. U. Idzerda, H. Lin, et al. Experimental confirmation of the X-ray magnetic circular dichroism sum rules for iron and cobalt. *Physical Review Letters*, 75(1):152–155, 1995.

[109] C. Piamonteze, P. Miedema, and F. M. F. de Groot. The accuracy of the spin sum rule in XMCD. *Journal of Physics: Conference Series*, 190(1):012015, 2009.

[110] M. Hennecke, I. Radu, R. Abrudan, et al. Angular Momentum Flow During Ultrafast Demagnetization of a Ferrimagnet. *Physical Review Letters*, 122(15):157202, 2019.

[111] R. Nyholm, N. Martensson, A. Lebugle, and U. Axelsson. Auger and Coster-Kronig broadening effects in the 2p and 3p photoelectron spectra from the metals ^{22}Ti-^{30}Zn. *Journal of Physics F: Metal Physics*, 11(8):1727–1733, 1981.

[112] J. Stöhr and Y. Wu. X-Ray Magnetic Circular Dichroism: Basic Concepts and Theory for 3D Transition Metal Atoms. In *New Directions in Research with Third-Generation Soft X-Ray Synchrotron Radiation Sources*, pages 221–250. Springer, Dordrecht, 1994.

[113] F. Willems. *Ultrafast optical demagnetization dynamics in thin elemental films and alloys: Foundations of and results from helicity-dependent and time-resolved XUV spectroscopy.* Phd thesis, Technischen Universität Berlin, 2019.

[114] H. S. Bennett and E. A. Stern. Faraday Effect in Solids. *Physical Review*, 137(2A):A448–A461, 1965.

[115] C. Möller, H. Probst, J. Otto, et al. Ultrafast element-resolved magneto-optics using a fiber-laser-driven extreme ultraviolet light source. *The Review of Scientific Instruments*, 92(6):065107, 2021.

[116] O. Pronin, V. Pervak, E. Fill, et al. Ultrabroadband efficient intracavity XUV output coupler. *Optics Express*, 19(11):10232–10240, 2011.

[117] Laser Components. *Data Sheet - HR15-30HTp1030/80/AR RW80-50-10UV, rect. XUV and NIR mirror, IBS1.*

[118] F. Frassetto, C. Cacho, C. A. Froud, et al. Single-grating monochromator for extreme-ultraviolet ultrashort pulses. *Optics Express*, 19(20):19169–19181, 2011.

[119] W. Cash. Echelle spectrographs at grazing incidence. *Applied Optics*, 21(4):710–717, 1982.

[120] S. Jana, J. A. Terschlüsen, R. Stefanuik, et al. A setup for element specific magnetization dynamics using the transverse magneto-optic Kerr effect in the energy range of 30-72 eV. *The Review of Scientific Instruments*, 88(3):033113, 2017.

[121] S. Günther, C. Spezzani, R. Ciprian, et al. Testing spin-flip scattering as a possible mechanism of ultrafast demagnetization in ordered magnetic alloys. *Physical Review B*, 90(18), 2014.

[122] S. Jana, R. Knut, S. Muralidhar, et al. Experimental confirmation of the delayed Ni demagnetization in FeNi alloy. *Applied Physics Letters*, 120(10):102404, 2022.

[123] S. Jana, R. Knut, S. Muralidhar, et al. Experimental confirmation of the delayed Ni demagnetization in FeNi alloy. *Applied Physics Letters*, 120(10), 2022.

[124] P. C. Johnsen, S. A. Ryan, C. Gentry, et al. A beamline for ultrafast extreme ultraviolet magneto-optical spectroscopy in reflection near the shot noise limit. *Review of Scientific Instruments*, 94(3):033001, 2023.

[125] F. Willems, C. von Korff Schmising, C. Strüber, et al. Optical inter-site spin transfer probed by energy and spin-resolved transient absorption spectroscopy. *Nature Communications*, 11(1):871, 2020.

[126] W. You, P. Tengdin, C. Chen, et al. Revealing the Nature of the Ultrafast Magnetic Phase Transition in Ni by Correlating Extreme Ultraviolet Magneto-Optic and Photoemission Spectroscopies. *Physical Review Letters*, 121(7):077204, 2018.

[127] T. D. Frazer, J. L. Knobloch, J. N. Hernández-Charpak, et al. Full characterization of ultrathin 5-nm low- k dielectric bilayers: Influence of dopants and surfaces on the mechanical properties. *Physical Review Materials*, 4(7), 2020.

[128] K. M. Hoogeboom-Pot, E. Turgut, J. N. Hernandez-Charpak, et al. Nondestructive Measurement of the Evolution of Layer-Specific Mechanical Properties in Sub-10 nm Bilayer Films. *Nano Letters*, 16(8):4773–4778, 2016.

[129] M. Tanksalvala, C. L. Porter, Y. Esashi, et al. Nondestructive, high-resolution, chemically specific 3D nanostructure characterization using phase-sensitive EUV imaging reflectometry. *Science Advances*, 7(5), 2021.

[130] H. Probst, C. Möller, M. Schumacher, et al. Unraveling Femtosecond Spin and Charge Dynamics with EUV T-MOKE Spectroscopy. arXiv:2306.02783 [cond-mat.mtrl-sci], 2023.

[131] C. La-O-Vorakiat, M. Siemens, M. M. Murnane, et al. Ultrafast demagnetization dynamics at the M edges of magnetic elements observed using a tabletop high-harmonic soft x-ray source. *Physical Review Letters*, 103(25):257402, 2009.

[132] B. Pfau, S. Schaffert, L. Müller, et al. Ultrafast optical demagnetization manipulates nanoscale spin structure in domain walls. *Nature Communications*, 3(1):1100, 2012.

[133] B. Vodungbo, J. Gautier, G. Lambert, et al. Laser-induced ultrafast demagnetization in the presence of a nanoscale magnetic domain network. *Nature Communications*, 3:999, 2012.

[134] O. Kfir, S. Zayko, C. Nolte, et al. Nanoscale magnetic imaging using circularly polarized high-harmonic radiation. *Science Advances*, 3(12):eaao4641, 2017.

[135] S. Zayko, O. Kfir, M. Heigl, et al. Ultrafast high-harmonic nanoscopy of magnetization dynamics. *Nature Communications*, 12(1):6337, 2021.

[136] M. Hofherr, S. Moretti, J. Shim, et al. Induced versus intrinsic magnetic moments in ultrafast magnetization dynamics. *Physical Review B*, 98(17), 2018.

[137] K. Yao, F. Willems, C. von Korff Schmising, et al. A tabletop setup for ultrafast helicity-dependent and element-specific absorption spectroscopy and scattering in the extreme ultraviolet spectral range. *The Review of Scientific Instruments*, 91(9):093001, 2020.

[138] J. K. Dewhurst, P. Elliott, S. Shallcross, E. K. U. Gross, and S. Sharma. Laser-Induced Intersite Spin Transfer. *Nano letters*, 18(3):1842–1848, 2018.

[139] J. K. Dewhurst, F. Willems, P. Elliott, et al. Element Specificity of Transient Extreme Ultraviolet Magnetic Dichroism. *Physical Review Letters*, 124(7):077203, 2020.

[140] E. Runge and E. K. U. Gross. Density-Functional Theory for Time-Dependent Systems. *Physical Review Letters*, 52(12):997–1000, 1984.

[141] R. van Leeuwen. Key Concepts in Time-Dependent Density-Functional Theory. *International Journal of Modern Physics B*, 15(14):1969–2023, 2001.

[142] S. Sharma, J. K. Dewhurst, and E. K. U. Gross. Optical Response of Extended Systems Using Time-Dependent Density Functional Theory. In *First Principles Approaches to Spectroscopic Properties of Complex Materials*, pages 235–257. Springer, Berlin, Heidelberg, 2014.

[143] P. M. Oppeneer, T. Maurer, J. Sticht, and J. Kübler. Ab initio calculated magneto-optical Kerr effect of ferromagnetic metals: Fe and Ni. *Physical Review B*, 45(19):10924–10933, 1992.

[144] J. Kuneš, P. M. Oppeneer, H.-C. Mertins, et al. X-ray Faraday effect at the $L_{2,3}$ edges of Fe, Co, and Ni: Theory and experiment. *Physical Review B*, 64(17), 2001.

[145] S. Mathias, C. La-O-Vorakiat, J. M. Shaw, et al. Ultrafast element-specific magnetization dynamics of complex magnetic materials on a table-top. *Journal of Electron Spectroscopy and Related Phenomena*, 189:164–170, 2013.

[146] J. Zak, E. R. Moog, C. Liu, and S. D. Bader. Universal approach to magneto-optics. *Journal of Magnetism and Magnetic Materials*, 89(1-2):107–123, 1990.

[147] J. Zak, E. R. Moog, C. Liu, and S. D. Bader. Magneto-optics of multilayers with arbitrary magnetization directions. *Physical Review B*, 43(8):6423–6429, 1991.

[148] D. Schick, A. Bojahr, M. Herzog, et al. UDKM1DSIM - A simulation toolkit for 1D ultrafast dynamics in condensed matter. *Computer Physics Communications*, 185(2):651–660, 2014.

[149] A. Meurer, C. P. Smith, M. Paprocki, et al. *SymPy: Symbolic computing in Python*. PeerJ, 2016.

[150] H. Höchst, D. Rioux, D. Zhao, and D. L. Huber. Magnetic linear dichroism effects in reflection spectroscopy: A case study at the Fe $M_{2,3}$ edge. *Journal of Applied Physics*, 81(11):7584–7588, 1997.

[151] S. Valencia, A. Gaupp, W. Gudat, et al. Faraday rotation spectra at shallow core levels: 3p edges of Fe, Co, and Ni. *New Journal of Physics*, 8(10):254, 2006.

[152] See Supplemental Material for details on the experimental setup, the data analysis and the theoretical calculations.

[153] T. Uchikoshi, Y. Sakka, M. Yoshitake, and K. Yoshihara. A study of the passivating oxide layer on fine nickel particles. *Nanostructured Materials*, 4(2):199–206, 1994.

[154] B. L. Zink, M. Manno, L. O'Brien, et al. Efficient spin transport through native oxides of nickel and permalloy with platinum and gold overlayers. *Physical Review B*, 93(18), 2016.

[155] C.-M. Wang, D. R. Baer, S. M. Bruemmer, et al. *Microstructure of the native oxide layer on Ni and Cr-doped Ni nanoparticles*, volume 11. American Scientific Publishers, 2011.

[156] J. K. Dewhurst and Sharma, Sangeeta, and et. al. `elk.sourceforge.net`.

[157] S.-g. Gang, R. Adam, M. Plötzing, et al. Element-selective investigation of femtosecond spin dynamics in NiPd magnetic alloys using extreme ultraviolet radiation. *Physical Review B*, 97(6), 2018.

[158] B. Watts. Calculation of the Kramers-Kronig transform of X-ray spectra by a piecewise Laurent polynomial method. *Optics Express*, 22(19):23628–23639, 2014.

[159] B. Koopmans, M. van Kampen, and W. J. M. de Jonge. Experimental access to femtosecond spin dynamics. *Journal of Physics: Condensed Matter*, 15(5):S723–S736, 2003.

[160] J. Lloyd-Hughes, P. M. Oppeneer, T. Pereira Dos Santos, et al. The 2021 ultrafast spectroscopic probes of condensed matter roadmap. *Journal of Physics. Condensed matter*, 33(35):353001, 2021.

[161] J. Minár, S. Mankovsky, O. Šipr, D. Benea, and H. Ebert. Correlation effects in fcc-Fe$_x$Ni$_{1-x}$ alloys investigated by means of the KKR-CPA. *Journal of Physics. Condensed matter*, 26(27):274206, 2014.

[162] J. K. Dewhurst, K. Krieger, S. Sharma, and E. Gross. An efficient algorithm for time propagation as applied to linearized augmented plane wave method. *Computer Physics Communications*, 209:92–95, 2016.

[163] M. Düvel, M. Merboldt, J. P. Bange, et al. Far-from-Equilibrium Electron-Phonon Interactions in Optically Excited Graphene. *Nano Letters*, 22(12):4897–4904, 2022.

[164] N. Pontius, J. K. Dewhurst, C. Schuessler-Langeheine, et al. Mapping the energy-time landscape of spins with helical X-rays. arXiv:2205.03172 [cond-mat.mtrl-sci], 2022.

[165] R. Gort, K. Bühlmann, G. Saerens, et al. Ultrafast magnetism: The magneto-optical Kerr effect and conduction electrons. *Applied Physics Letters*, 116(11):112404, 2020.

[166] B. Koopmans, G. Malinowski, F. Dalla Longa, et al. Explaining the paradoxical diversity of ultrafast laser-induced demagnetization. *Nature Materials*, 9(3):259–265, 2010.

[167] M. Keunecke, C. Möller, D. Schmitt, et al. Time-resolved momentum microscopy with a 1 MHz high-harmonic extreme ultraviolet beamline. *Review of Scientific Instruments*, 91(6):063905, 2020.

[168] S. Eich. *Ultrafast Dynamics of Photoinduced Phase Transitions in Correlated Electron Materials.* Phd thesis, Technische Universität Kaiserslautern, 2016.

List of Figures

List of Tables

Acknowledgement

Zum Abschluss möchte ich mich bei sehr vielen Menschen bedanken, ohne die diese Arbeit nicht möglich gewesen wäre!

- Stefan Mathias danke ich zunächst einmal für die Möglichkeit in seiner Arbeitsgruppe und an diesem interessanten Projekt zu arbeiten. Danke für die begeisterten wissenschaftlichen Diskussionen, die motivierenden Gespräche und vor allem für das große Vertrauen in meine Arbeit. Ich bin dankbar für die vielen Möglichkeiten, die mir Stefan in der Zeit meiner Promotion gegeben hat, wie der Forschungsaufenthalt in Boulder und der Besuch verschiedener internationaler Konferenzen.

- Martin Wenderoth danke ich, dass er ohne zu zögern bereit dazu war, als Zweitprüfer für meine Arbeit zu fungieren (trotz zahlreicher weiterer Disputationen im gleichen Zeitraum). Mein Dank gilt hierbei auch allen weiteren Mitgliedern der Prüfungskommission: Cynthia Volkert, Vasily Moshnyaga, Peter Blöchl und Tobias Meyer.

- Christina, dir danke ich für die gesamte Zeit, die wir in der Promotion gemeinsam verbracht haben. Ohne deine Unterstützung, dein offenes Ohr, die unzähligen wissenschaftlichen Diskussionen (in Person und per Zoom), die vielen gemeinsamen Messzeiten und deine ruhige und motivierende Art, wäre diese Arbeit so nicht entstanden. Ich werde unsere Zusammenarbeit vermissen und bin dir einfach für **alles** dankbar. Mit dir habe ich während der Promotion nicht nur eine tolle Kollegin, sondern auch eine wunderbare Freundin gewonnen!

- Daniel Steil danke ich für die Beantwortung zahlreicher Fragen, die vielen gemeinsamen Diskussionen, dass er sich immer Zeit für meine Problemchen genommen und mich mit Korrekturen und vielen Ideen für diese Arbeit unterstützt hat.

- Matthijs Jansen gilt großer Dank für seine tatkräftige Unterstützung in den letzten Monaten. Danke für die Beantwortung hunderter Rocket.Chat-Nachrichten, dem intensiven Einsatz für unsere Paper und für die unentbehrliche Hilfe mit Python.